TECHNISCHE UNIVERSITÄT MÜNCHEN
Institut für Energietechnik

Lehrstuhl für Thermodynamik

Auto-Ignition and Combustion of Fuel Jets in Vitiated Co-Flow at Elevated Pressure

Georg Tautschnig

Vollständiger Abdruck der von der Fakultät für Maschinenwesen der Technischen Universität München zur Erlangung des akademischen Grades eines

Doktor-Ingenieurs

genehmigten Dissertation.

Vorsitzender:
Univ.-Prof. Dr.-Ing. W. A. Günthner
Prüfer der Dissertation:
1. Univ.-Prof. Dr.-Ing. Th. Sattelmayer
2. Univ.-Prof. E. Mastorakos, Ph.D., University of Cambridge / UK

Die Dissertation wurde am 08. 12. 2015 bei der Technischen Universität München eingereicht und durch die Fakultät für Maschinenwesen am 18. 04. 2016 angenommen.

Für Georg

Danksagung

Die vorliegende Arbeit entstand während meiner Tätigkeit als wissenschaftlicher Mitarbeiter am Lehrstuhl für Thermodynamik an der TU München. Sie wurde von der Firma Alstom Power GmbH und dem deutschen Forschungsverbund AG-Turbo gefördert.

Mein besonderer Dank gilt meinem Doktorvater, Herrn Professor Dr.-Ing. Thomas Sattelmayer, der es mir ermöglicht hat, diese Arbeit zu einem erfolgreichen Abschluss zu bringen. Vielen Dank für das entgegengebrachte Vertrauen und die fachlichen Impulse!

Ohne die vielen fachlichen Diskussionen mit Dr.-Ing. Christoph Hirsch wäre es wohl kaum möglich gewesen, die Ideen die dieser Arbeit zu Grunde liegen zu entwickeln. Vielen Dank für die stets positive Sichtweise, die aufmunternden Worte und stete Hilfsbereitschaft!

Bei meinen Kollegen vom Lehrstuhl, insbesondere meiner Bürokollegin Eva-Maria Haner die mit mir dieses Projekt bearbeitet hat möchte ich mich für die Zusammenarbeit bedanken. Ein besonderer Dank auch an Dr.-Ing. Janine Sangl, Michael Hertweck, Balbina Hampel, meinen Studentischen Hilfskräften und Semestranden die mit mir manch einen Kampf mit dem Hochdruckversuchsstand ausgefochten haben. Vielen Dank auch an die Lehrstuhlwerkstatt, das Sekretariat rund um Helga Basset und die TUM-Feuerwehr für ihre Unterstützung.

Ein großes Danke an Dr.-Ing. Thomas Fiala und Dr.rer.nat. Daniel Herde für die finale Unterstützung und hilfreichen Kommentare zu meiner Arbeit.

Meinen Eltern möchte ich für ihren Rückhalt danken, dass Sie mir die Basis für meine Ausbildung geschaffen haben und es mir dadurch ermöglichten, diese Arbeit zu schreiben. Von ganzem Herzen möchte ich meinem Bruder Michael für die immerwährende Unterstützung aus der Ferne danken! Danke auch an die Familie meiner Verlobten für die stete Versorgung durch nicht-wissenschaftliche Güter und die Unterstützung in schwierigen Zeiten.

Der letzte und wichtigste Dank geht an meine Andrea, die mich in dieser langen Zeit durch Dick und Dünn begleitet, ertragen und getragen hat und mir stets die guten und schönen Seiten des Lebens aufgezeigt hat. Danke!

Vilsbiburg, 2015 Georg Tautschnig

Significant parts of this Ph.D. thesis were published by the author beforehand in conference proceedings, journal papers and reports. All of these prior printed publications are registered according to the valid doctoral regulations. However, not all of them are quoted explicitly everywhere as they are part of this present work being official documents. Whether these personal prior printed publications were referenced, depended on maintaining comprehensibility and providing all necessary context.

Wesentliche Teile dieser Dissertation wurden vom Autor bereits vorab als Konferenz- und Zeitschriftenbeiträge sowie im Rahmen von Berichten veröffentlicht. Alle Vorveröffentlichungen sind entsprechend der gültigen Promotionsordnung ordnungsgemäß gemeldet. Sie sind deshalb nicht zwangsläufig im Detail einzeln referenziert. Vielmehr wurde bei der Referenzierung eigener Vorveröffentlichungen Wert auf Verständlichkeit und inhaltlichen Bezug gelegt.

Kurzfassung

Gestufte Verbrennung in Verbindung mit einer Expansionsturbine zwischen den Brennkammern ist ein guter Weg, um Gasturbinen auch im niedrigen Lastbereich emissionsarm betreiben zu können. Das dominierende Verbrennungsregime in der zweiten Verbrennungsstufe ist Selbstzündung. Im Rahmen dieser Arbeit wird ein generisches, unter Druck stehendes zweistufiges Verbrennungsexperiment vorgestellt, an welchem optische Messtechniken an der zweiten Verbrennungsstufe Anwendung finden. Größen wie die Abhebehöhe oder die Luftzahl der selbstzündenden Flamme werden gemessen. Um die Luftzahl durch spektrale Analyse der Chemilumineszenz zu bestimmen, werden die Einflüsse des hohen Inertgasanteils und der hohen Temperatur des Oxidators auf die Chemilumineszenz-Emissionen untersucht. Die beobachteten Tendenzen können in Simulationen erfolgreich nachvollzogen werden.

Abstract

Sequential staged combustion with an expansion turbine between both stages is an efficient way of extending the low emission regime of gas turbines towards very low loads. The dominating combustion regime in the second stage is auto-ignition. A generic pressurized staged combustion experiment is presented whereon optical measurement techniques are applied to the second combustion stage. Lift-off height and air excess ratio of the flame in the ignition region are determined. In order to measure air excess ratios in the second stage, influences of vitiated conditions on chemiluminescence are investigated. Tendencies observed in the experiments are simulated successfully.

Contents

List of Figures

List of Tables

Nomenclature

Latin Characters

a	Constant (linear regression analysis)	-
b	Coefficient (linear regression analysis)	-
c_χ	Constant	s
c_p	Specific heat capacity at constant pressure	J kg^{-1} K^{-1}
d	Nozzle-diameter	m
e	Step number	-
f	Focal length	m
$\check{h}$	Planck constant	J s
h	Specific enthalpy	J kg^{-1}
j_i	Diffusion flux of species i	-
k_R	Reaction rate coefficients	cm^3 mol^{-1} s^{-1}
k	Turbulent kinetic energy	m^2 s^{-2}
l_{min}	Stoichiometric air-fuel ratio	kg kg^{-1}
$l_{min,m}$	Molar stoichiometric air-fuel ratio	kmol kmol^{-1}
l_T	Turbulent length scale	m
$\dot{m}$	Mass flow	kg s^{-1}
m	Mass	kg
p	Pressure	Pa, bar
q	Specific heat per volume	J kg^{-1} m^{-3}
s	Slope	-
t	Time	s
u	Velocity	m s^{-1}
v_{min}	Minimum flue gas quantity	kmol kmol^{-1}
v', v''	Vibrational states	-
$\dot{w}_i$	Chemical source term of species i	kg m^{-3} s^{-1}
$\mathbf{x}$	Position vector	-
x_1, x_2, x_3	Cartesian coordinate directions	-
A	Area	m^2

$\breve{A}$	Coefficient	-
A_i	Einstein coefficient of species i	s^{-1}
A_A	Pre-exponential factor	mol cm^{-3} s^{-1}
AR	Aspect ratio	-
$\breve{B}$	Coefficient	-
$\breve{C}$	Coefficient	-
$C_{j,r}$	Molar concentration of each reactant and product species j in reaction r	-
C	Proportionality factor	-
D_h	Hydraulic diameter	m
D_Z	Diffusion coefficient	m^3 m^{-1} s^{-1}
E_A	Activation energy	J mol^{-1}
$E(\zeta)$	Expected value of ζ	-
$F(\lambda_v)$	Self-similarity function	-
$H_{l.o.}$	Lift-off height in nozzle-diameter	-
H	Enthalpy	J
I	Intensity	-
J	Momentum flux ratio	-
K_w	Expansion factor	m s^{-1} Pa^{-1}
L_t	Integration length	m
M	Molar mass	kg mol^{-1}
N_r	Number of chemical species in reaction r	-
$P(\zeta)$	Probability density function of ζ	-
PV	Normalized progress variable	-
$\dot{Q}$	Heat flow	W
R^2	Determination coefficient	-
R	Gas constant	J mol^{-1} K^{-1}
S	Measurement signal	-
T_{ad}	Adiabatic flame temperature	K
T	Temperature	K, °C
T_{Plenum}	Air temperature before vitiator	K
$\hat{T}$	Transmission	-
TI	Turbulence intensity	-
U	Internal energy	J
V	Volume	m^3
W	Width of mixture profile	-
X	Mole fraction	kmol $kmol^{-1}$
Y	Mass fraction	kg kg^{-1}

Z	Mixture fraction	kg kg^{-1}
$\widetilde{Z''^2}$	Variance of mixture fraction	-
$[i]$	Concentration of species i	mol cm^{-3}

Greek Characters

α	Heat transfer coefficient	W m^{-2} K^{-1}
α_β, β_β	Shape parameters beta distribution	-
γ	Variable	-
δ	Difference between center position of evaluation window and lift-off height	-
ε	Turbulent dissipation rate	m^2 s^{-3}
$\breve{\varepsilon}$	Emissivity	-
ϕ	Equivalence ratio	-
Φ	Variable	-
ζ	Variable	-
η	Dynamic viscosity	N s m^{-2}
ι	Volumetric photon emission rate	mol cm^{-3} s^{-1}
κ	Curvature	m^{-1}
λ	Air excess ratio	-
λ_T	Thermal conductivity	W m^{-1} K^{-1}
λ_v	Wavelength	m
ν	Frequency	s^{-1}
$\nu_{i,r,1}$	Stoichiometric coefficient for reactant i in reaction r	-
$\nu_{i,r,2}$	Stoichiometric coefficient for product i in reaction r	-
ξ	Variable	-
ρ	Density	N m^{-2}
σ	Stefan-Boltzmann constant	W m^{-2} K^{-4}
σ^2	Variance	-
τ	Ignition delay time, characteristic time	s
τ_x	Time	s
τ_T	Turbulent time scale	s
ψ	Variable	-

$\langle \chi_{st} \rangle$	Conditional mean of scalar dissipation rate	s^{-1}
χ	Scalar dissipation rate	s^{-1}
$\dot{\omega}_i$	Chemical source term of species i (molar)	mol m^{-3} s^{-1}
Γ, Ξ, Ψ, Ω	Variables representing chemical species	-

Subscripts

0	Jet
AI	Auto-ignition
BP	Bandpass
c	Progress variable, value on center line
d	Distorted
eff	Effective diameter
eq	Equilibrium value
e, i, j, k, l	Indices
Exp	Experimental setup
$fuel$	Fuel
g	Gas
GSB	Generic swirl burner
h	Horizontal index
in	Value at inlet
in_2	Value at inlet 2^{nd} combustion stage
bin	Binary
m, n	Stoichiometric indices
ref	Reference value
rms	Root mean square
r	Number of reaction
R	Radiation
SC	Sequential combustor
st	Stoichiometric, stoichiometry
t	Thermocouple
u	Undistorted
v	Vertical index
w	Wall
∞	Main flow

Superscripts

$()^B$	Temperature exponent
$()^*$	Chemiluminescence
$()'$	Fluctuating value
$\bar{(\ )}$	Time average
$\hat{(\ )}$	Volumetric average

Non-Dimensional Numbers

Da	Damköhler number
Le	Lewis number
Nu	Nusselt number
Pr	Prandtl number
Re	Reynolds number
Sc	Schmidt number

Abbreviations

CFD	Computational fluid dynamics (simulation)
DNS	Direct numerical simulation
EV	Alstom premix burner
FWHM	Full width at half maximum
PDF	Probability density function
PMT	Photo multiplier tube
PLIF	Planar laser induced fluorescence
RANS	Reynolds averaged Navier Stokes
SEV	Alstom sequential burner

1 Introduction

Renewable energy systems will become more important in future as resources of fossil fuels are limited. One disadvantage of renewable energy systems is that their output often depends on weather conditions and therefore fluctuates. To compensate for such fluctuations, highly efficient gas turbine power plants that can be started up quickly are necessary. Moreover, they need to be efficient at part load, too. Sequential staged combustion with an expansion turbine between the two stages is an option to extend the low emission regime of gas turbines towards very low loads. In ALSTOM's GT24/26 gas turbines, sequential combustion is realized. Due to the staged combustion process the inlet conditions of the second combustion stage are different to the one of the first combustor. High inlet temperatures offer the possibility to start the combustion process without any external energy source, via *auto-ignition*. Furthermore, increased contents of inert gas and the decreased oxygen content in the oxidator (*vitiated* conditions) can influence flame behavior (lift-off height, instabilities) and radiation (*chemiluminescence*) of the flame.

Distinctly higher amounts of inert gas in the second combustion stage can occur if flue gas recirculation is applied to gas turbines with staged combustion. Flue gas recirculation is a way to increase the relative CO_2 content in the exhaust gas in order to make the post-combustion CO_2 sequestration processes more efficient. This will be relevant if either sensible ways are found to utilize sequestrated CO_2 further or safe storage can be provided.

1.1 Background

The present study was initiated by the COORETEC-Turbo program of the research association AG-Turbo, which consisted of universities, research facilities and industrial partners. With support of the *Bundesministerium für Wirtschaft und Technologie* their aim was to promote the development of climate friendly, low emission and resource saving power plants on the basis of advanced turbo machines [AT11]. The project COORETEC-Turbo 2.1.5 "Investigation of a gas turbine com-

bustion process with flue gas recirculation for efficient CO_2 sequestration" was realized in cooperation with ALSTOM Power GmbH.

While ALSTOM Power GmbH conducted tests on engine hardware under engine conditions at the DLR institute in Cologne, TU Munich developed a generic experiment to investigate the process of auto-ignition with flue gas recirculation. A coaxial turbulent round jet in vitiated axisymmetrical co-flow was chosen since it comprises the full complexity of turbulence-chemistry interaction in a moderately complex turbulent flow. Two variants of the jet were investigated. The plain round fuel jet and the concentric fuel jet with an annular injection of shielding air. Whereas the first configuration allows to investigate fundamental effects of a vitiated co-flow on auto-ignition, the second configuration reflects technological systems where the shielding air is used to influence the mixing and ignition delay to optimize the combustion properties. The effect of shielding air on NO_x emissions was investigated by Haner, who also did cold mixture measurements of a jet in co-flow and a jet in cross-flow configuration [HTH+13]. In the present thesis the focus lies on the plain round fuel jet where the dominating combustion regime is auto-ignition.

1.2 Scope

From literature ([SC94, BPF06]) it is known that temperature is the main driver for auto-ignition. The aim of this work is to investigate other influences than temperature on auto-ignition experimentally and numerically. The impact of momentum flux ratio, pressure and oxygen content on the lift-off height of an auto-igniting natural gas jet in hot vitiated co-flow is studied. Air excess ratios are determined in the zones where combustion is initiated by self-ignition to find out whether ignition starts preferably at air excess ratios differing from the stoichiometric value, as postulated by Mastorakos [Mas09]. For the air excess ratio measurements the influence of the vitiated conditions and of pressure on the chemiluminescence signal emitted from the flame had to be clarified in order to use it for quantitative analysis. Also as auto-ignition is a highly fluctuating process a simultaneous measurement technique had to be developed to sample the chemiluminescence characteristics of the auto-ignition flame kernel.

1.3 Overview

In chapter 2 fundamentals of the processes studied in this work are given. The test rig, combustor setups and measurement setups are explained in chapter 3. Then the flamelet model, its implementation in Matlab and the chemiluminescence model are shown. Experimental as well as numerical results are presented in chapter 5. The last section 6 summarizes and concludes this study.

2 Fundamentals

This chapter introduces basic principles of combustion, chemiluminescence and a statistical method that is used to analyze measurement data in the results section.

2.1 Combustion

Combustion is the process of releasing chemically bound energy in form of sensible enthalpy by chemical change [Pet12]. The reactants are transformed to products (e.g.: $CH_4 + 2\ O_2 \rightarrow CO_2 + 2\ H_2O$). In order to burn fuel such as methane or natural gas, it needs to be mixed with an oxidator (e.g.: oxygen, air). Two extreme cases can be distinguished:

1. The mixing process is completed upstream of the combustion chamber.
2. The mixing process takes place in parallel to the combustion process inside the combustion chamber.

The first case is referred to as “premixed” and the second as “non-premixed” combustion. With premixed combustion processes low pollutant emissions can be achieved when lean mixtures are burned. Therefore premixed combustion is often applied in modern power generation gas turbines.

The word premixed implies that the fuel/oxidator mixture which enters the combustion chamber is homogenous. Such mixtures are necessary for investigations on spectrally resolved chemiluminescence measurements as shown in section 5.2. In real technology premixing is never complete but depends on the turbulence structure and the residence time between fuel injection and the flame. This is in particular true for sequential combustion. Therefore investigations are done on a fuel jet injected coaxially into a vitiated flow using the flame lift-off as premixing time. Since mixing and reaction i.e. auto-ignition, occur simultaneously, the process description follows the theory of non-premixed flames.

2.1.1 Non-Premixed Flames

In many technical combustion processes, including industrial ovens and Diesel engines, oxidator and fuel are transported separately to the combustion chamber. The mixing process happens within the combustion chamber by means of convection and diffusion. Since often diffusion is the rate limiting step, the resulting flames are often called "diffusion flames". For flames that are rate limited by mixing, combustion occurs where near stoichiometric mixture is achieved and the combustion rate can be reduced to the calculation of the mixing rate ("mixed $\equiv$ burned"). In case of auto-ignition, the rate limitation is governed by the chemical reaction rate, therefore detailed chemistry needs to be considered.

2.1.2 Mixture Fraction

In non-premixed systems with two distinct streams (oxidator, fuel), the mixture fraction is an important parameter to describe the state of mixing. In this case the oxidator contains no fuel and the fuel does not contain any oxygen. As the oxidator is air, the amount of nitrogen needs to be taken into account (mass fraction of oxygen: $Y_{O_2} = 0.23$). In case of vitiated combustion it is necessary to consider that the oxygen content is lower in the second combustor as it depends on the operating conditions of the first combustion stage. The fuel used in this study is natural gas, which contains N_2 and CO_2. Therefore the combustible mass fraction of the fuel is unequal unity (mass fraction of combustible fuel: $Y_{fuel} = 0.974$).

In the following, the index 0 corresponds to the fuel and ∞ to the oxidator. According to Peters [Pet12] the mixture fraction for masses is defined as:

$$Z = \frac{m_0}{m_0 + m_\infty}. \tag{2.1}$$

Z can vary between zero and one. In the fuel stream Z is unity and in the oxidator stream Z is zero. λ denotes the air excess ratio[1]. It is the ratio of the amount of available oxygen to the minimum amount of oxygen necessary for stoichiometric combustion. l_{min} is the minimum amount of air necessary for stoichiometric combustion per unit of fuel. With the relation

$$\lambda \cdot l_{min} = \frac{m_\infty}{Y_{fuel,0} \cdot m_0}, \tag{2.2}$$

1 The air excess ratio corresponds to the inverse value of the equivalence ratio $\lambda = \phi^{-1}$

the mixture fraction can be written as:

$$Z = \frac{1}{1 + \lambda l_{min} Y_{fuel,0}}. \tag{2.3}$$

2.1.3 Auto-Ignition

In this section the basics of ignition and the way parameters such as temperature or pressure influence auto-ignition are presented.

Mastorakos [Mas09] defines auto-ignition *[...] to be contrasted to forced ignition in that no external source is needed to reach fully-fledged combustion.*

A characteristic value for auto-ignition of hydrocarbon mixtures is the *ignition delay time* [BK08]. The reason for this delay are radical chain reactions that control the combustion process of hydrocarbons [Bra05]. Radicals are produced in a start reaction if enough energy is available. These radicals react with other molecules and therefore new radicals are formed. If the quantity of radicals increases in chain branching reactions, the number of radicals increases exponentially. Ignition will only occur if more radicals are produced than consumed in chain-breaking reactions [Süß12, Rod07]. To reach such conditions, temperature of the fuel/air mixture needs to be high enough as chemical reaction rates depend exponentially on it. During the induction phase, where the number of radicals increases, the freed reaction enthalpy is consumed by the formation of new radicals and temperature remains almost constant. Once the critical number of radicals is reached, temperature increases almost instantly.

There exist different methods to define ignition delay time. For the numerical parts in this work the point of ignition is defined as being the moment where a normalized progress variable exceeds a value of 0.5. The definition of the normalized progress variable will be given in Eqn. 4.9.

Experimentally, the ignition delay can be determined in shock-tube experiments where a diaphragm separates two masses of gas initially at rest. The gas in the *driver section* is at high pressure, whereas the mass at low pressure is the *driven section* and forms the ignitable mixture of interest. By changing initial pressures in the two sections, test conditions can be varied. Destroying the diaphragm results in a shock wave being sent into the low pressure section increasing static pressure and temperature of the mixture. The shock wave is reflected at the boundary wall of the tube and leads to a further increase of static pressure and temperature. The

ignition delay is defined as the time between the moment the shock wave passes the measurement section and the start of the rapid reaction, measured by pressure sensors or photomultiplier instrumentation.

Based on shock-tube experiments and data from other literature, Spadaccini and Colket [SC94] obtain the following relation for ignition delay times of methane given in s:

$$\tau = 2.21 \cdot 10^{-14} \exp(22659/T) \cdot [O_2]^{-1.05} \cdot [CH_4]^{0.33}, \tag{2.4}$$

and for natural gas, which considers other hydrocarbons than methane in the fuel, too:

$$\tau = 1.77 \cdot 10^{-14} \exp(18693/T) \cdot [O_2]^{-1.05} \cdot [CH_4]^{0.66} \cdot [HC]^{-0.39}. \tag{2.5}$$

Herein the square brackets represent concentrations of the species in mol cm^{-3} and $[HC]$ denotes the total molar concentration of all non-methane hydrocarbons. T denotes the temperature in K. Several studies such as [SC94, Bra05, HW69, LSBS71] show that it is important to consider higher hydrocarbons. Among these, Higgin and Williams [HW69] show that an addition of 1 % n-butane reduces ignition delay by a factor of three. For the ignition delay-relation in Eqn. 2.5 shock-tube experiments at temperatures from 1300 K to 2000 K, equivalence ratios between 0.45 and 1.25 and pressures from 3 atm to 15 atm were conducted [SC94]. Besides the fuel composition, Eqn. 2.5 considers temperature, the oxygen content in the oxidator and the pressure, as the concentrations are pressure dependent:

$$[\ ]_i = \frac{X_i p}{RT}. \tag{2.6}$$

Herein X_i is the mole fraction of species i, p the pressure in Pa, R the universal gas constant and T the absolute temperature of the mixture in K.

As the reaction rate depends exponentially on temperature, temperature is the main driver for auto-ignition. Figure 2.1 shows measurement data of Goy et al. [GMT01], gained from shock tube measurements. They compare their measurements with data calculated with the ignition delay relation (see Eqn. 2.5) of Spadaccini and Colket [SC94] (dashed line). As expected, ignition delay highly depends on temperature. Furthermore Fig. 2.1 shows that the agreement between

the relation for ignition delay and the measured data is acceptable in a temperature range from 1100 K to 1400 K, although the relation of Spadaccini and Colket is validated from 1300 K to 2000 K. Below 1100 K measurement data of Goy et al. [GMT01] gives distinctly lower values for the ignition delay than the ignition delay relation of Spadaccini and Colket [SC94]. According to Fig. 2.1, ignition delay depends less on temperature in the temperature range below 1100 K.

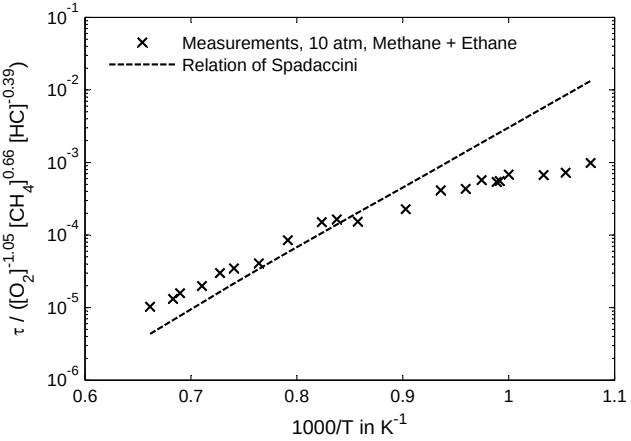

Figure 2.1: Ignition delay normalized for oxygen, methane and higher hydrocarbon molar concentrations as a function of mixture temperature, taken from Goy et al. [GMT01]. Pressure 10 atm, air excess ratio $\lambda = 2$, fuel mixture: methane and 15 % per volume ethane.

Figure 2.2 shows ignition delay times for three different pressure levels. Pressure as well as temperature decrease the ignition delay time, though the influence of pressure is smaller. For the measurements shown in Fig. 2.2, pure methane is used as fuel. Therefore Goy et al. [GMT01] used Spadaccini and Colket's relation for ignition delay of methane (Eqn. 2.4). It can be seen that the relation is suitable for temperatures higher than 1250 K.

Beside temperature, fuel and pressure, the oxygen concentration and other species can influence the ignition delay time. Spadaccini and Colket [SC94] measure in their study a stronger dependence on the oxygen concentration than Goy et al. [GMT01]. According to Spadaccini and Colket ignition delay decreases with

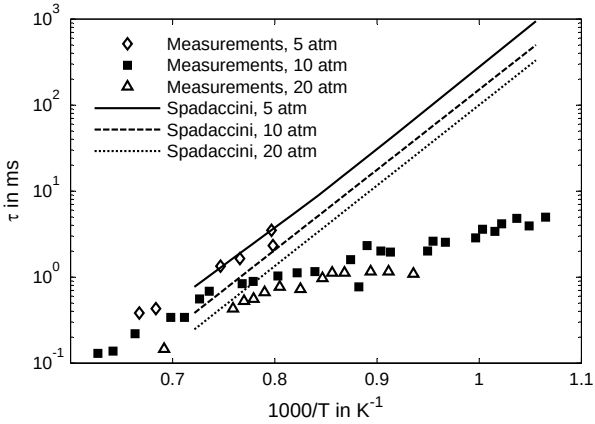

Figure 2.2: Ignition delay as a function of mixture temperature, taken from Goy et al. [GMT01]. Pressure is varied, air excess ratio $\lambda = 2$, fuel: methane.

increasing oxygen concentration (see also Eqn. 2.4 and 2.5). According to Goy et al. [GMT01], other species than water increase the ignition delay with increasing concentration.

In summary, temperature is the controlling factor of auto-ignition. Besides, many other parameters can influence ignition delay time. Therefore it is a challenging task to control or to simulate combustion processes that are dominated by auto-ignition.

Relevant Studies on Auto-Igniting Fuel Jets

While no claim of completeness is made for the following short review it serves to point out some findings of other authors and to formulate the open questions adressed in this study.

Markides and Mastorakos [MM05] study auto-ignition of a fuel jet (hydrogen) in a hot co-flow at atmospheric pressure. The oxidator was pure air. In a review paper Mastorakos [Mas09] concludes that ignition preferably occurs in areas of low mixture- and temperature gradients. Furthermore he states that there is a “most

reactive mixture fraction" where ignition preferentially occurs. As the fuel enters the combustion chamber at a lower temperature than the oxidator, the most reactive mixture fraction lies on the lean side of the mixture (for hydrogen and methane). According to Mastorakos [Mas09], experimental data from mixture fraction measurements in auto-igniting jet flames are sparse. Furthermore he states that the influence of pressure on the most reactive mixture fraction is not studied yet.

Oldenhof et al. [OTvVR11] present in their study a jet in vitiated hot co-flow at atmospheric conditions. The co-flow has a particular temperature profile, resulting from cooling of the fuel lance. They observe lower lift-off heights at higher jet Reynolds numbers and explain this with more entrainment of hotter air. Oldenhof et al. do not discuss the influence of a temperature profile on lift-off height at increased pressure.

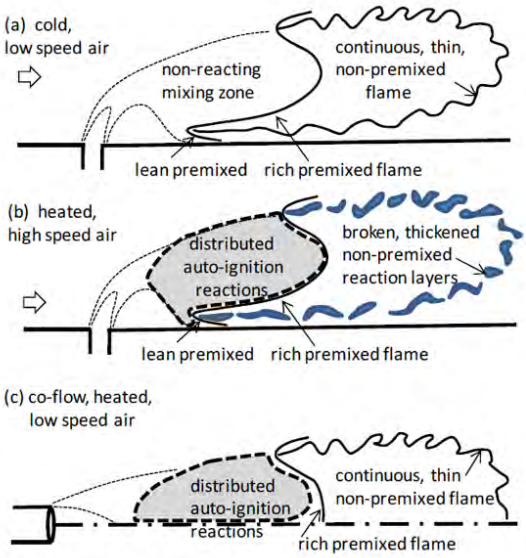

Figure 2.3: Schematic of highly-lifted flames, illustrating some effects of raising the air temperature above the auto-ignition temperature and increasing the air velocity [MD11].

Micka and Driscoll [MD11] investigate jet flames (fuel: 50 % ethylene, 50 % hydrogen) in a heated (1364 K) cross-flow (Reynolds number in main flow: 80000) using PLIF-measurements. They state that, depending on the flow velocity of the hot flow, different flame regimes can be observed (see Fig. 2.3): in case of hot co- or cross-flows, random auto-ignitions occur shortly after the fuel nozzle. In the far field, either a continuous non-premixed thin flame or thickened broken non-premixed reaction layers can be seen, depending on the flow velocity of the main flow. Flame regimes occuring in a highly turbulent auto-igniting jet in a hot co-flow flame are not discussed by Micka and Driscoll.

In the current work, auto-ignition of a methane jet in hot vitiated co-flow is investigated. An aim is to measure the mixture fraction in the ignition zone of the flame to find out whether ignition preferably takes place at lean mixture fractions. Furthermore the influence of parameters such as pressure on the most reactive mixture fraction shall be investigated.

In this study a temperature profile similar to that in the work of Oldenhof et al. [OTvVR11] occurs. The influence of such a profile on auto-ignition at elevated pressure is investigated. Furthermore the occurring flame regime is compared to the flame regimes shown in Fig. 2.3.

2.1.4 Sequential Combustion

The combustion process in ALSTOM's GT24/26 gas turbines is based on a reheat process which leads to higher specific power and efficiency than the simple gas turbine cycle of the same maximum process temperature and pressure.

As seen from Fig. 2.4, the reheat process is realized by sequential combustion. The total fuel rate is split between a primary combustor equipped with EV-Burners and a secondary reheat combustor based on SEV-Burners. Between primary and secondary combustor the power extracted by the high pressure turbine reduces the hot gas temperature, such that additional fuel can be burned to raise the fluid temperature for the low pressure turbine. In the second combustion stage cold air is injected coaxially to the fuel to increase the ignition delay time and to enhance the mixing between fuel and oxidator. This way almost perfect mixing can be achieved which leads to low NO_x emissions [BK08]. Furthermore, with sequential combustion processes, an improved part load behavior of the gas turbine can be achieved [CEGP10].

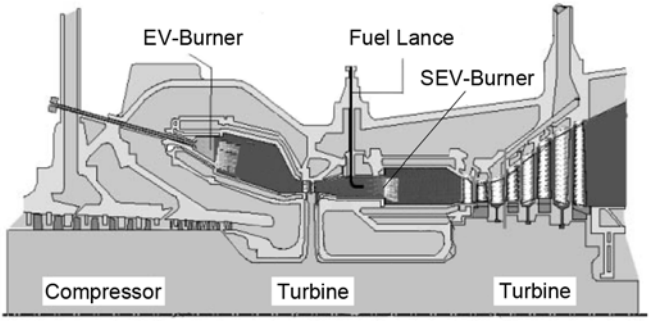

Figure 2.4: Cross section of the GT24/26 [Bra05].

2.2 Characteristics of Turbulent Flows

In turbulent flows, velocity as well as other properties of the flow are fluctuating stochastically around a mean value. The instantaneous velocity can be decomposed into an averaged velocity and the fluctuation component:

$$u_i(\mathbf{x},t) = \overline{u_i}(\mathbf{x}) + u_i'(\mathbf{x},t). \tag{2.7}$$

Applying the decomposition 2.7 to the equations for conservation of mass and conservation of momentum and averaging the terms, the Reynolds Averaged Navier Stokes (RANS) equations can be obtained [Bra05]:

$$\frac{\partial \overline{\rho}}{\partial t} + \frac{\partial}{\partial x_i}(\overline{\rho}\,\bar{u}_i) = 0, \tag{2.8}$$

$$\frac{\partial \overline{\rho}\bar{u}_i}{\partial t} + \frac{\partial}{\partial x_j}(\overline{\rho}\bar{u}_i\bar{u}_j) + \frac{\partial \overline{p}}{\partial x_i} = \frac{\partial}{\partial x_j}(-\overline{\rho u_i' u_j'}). \tag{2.9}$$

Wherein u corresponds to the velocity, p to the pressure, ρ to the density and x denotes the Cartesian coordinate.

The last term of Eqn. 2.9 is called the Reynolds stress tensor which needs to be modeled to close the problem. Even though computational power gets cheaper theses days, RANS simulations are still very attractive if many different simulations need to be conducted for parametric studies. In this study, the Realizable k-ε RANS model is applied wherein two more differential equations need to be solved – one for the turbulent kinetic energy k and another one for the dissipation rate ε. More details on simulation of turbulent flows can be found in literature [BPF06, Pop00, Inc02].

In turbulent flows, a large spectrum of length- and timescales can be observed, also named *energy cascade*. The largest eddies are in the range of the flow duct and show a preferred orientation. Those structures break up into smaller structures. The smaller the structures become, the less they are affected by the main flow and isotropic behavior is assumed. According to the theory of Kolmogorov, kinetic energy is transferred from larger to smaller structures along the energy cascade. At the end of it, the kinetic energy is dissipated into internal energy. The turbulent dissipation rate ε is the mean rate at which energy is converted. An estimation of ε is possible by looking at large eddies as the total kinetic energy is only passed through the different sizes of eddies until it is dissipated [Bra05, Pop00].

$$\varepsilon = \frac{k}{\tau_T}. \tag{2.10}$$

τ_T is the turbulent time scale that is equal to the time a large eddy needs for one rotation. Given the turbulent length scale and the fluctuating velocity it can be determined:

$$\tau_T = \frac{l_T}{u'}. \tag{2.11}$$

The turbulent length scale can be estimated as being proportional to the hydraulic diameter and the fluctuating velocity is proportional to the bulk velocity of the investigated problem.

By summarizing the *rms* (root mean square) values of the velocities, the turbulent kinetic energy can be calculated [Tur00]:

$$k = \frac{1}{2}(u'^2_{1,rms} + u'^2_{2,rms} + u'^2_{3,rms}). \tag{2.12}$$

rms values give the turbulence intensity of flow properties and are defined as follows (ξ being an arbitrary fluctuating signal):

$$\xi'_{rms} = \sqrt{\overline{\xi'^2}}. \tag{2.13}$$

The relative turbulence intensity TI is determined via normalization by the mean bulk velocity u_∞:

$$TI = \frac{1}{u_\infty} \sqrt{\frac{1}{3}(u'^2_{1,rms} + u'^2_{2,rms} + u'^2_{3,rms})}. \tag{2.14}$$

2.3 Simulation of Combustion

Turbulent combustion simulation is a demanding task because a large number of species need to be calculated to capture full chemistry and because of the turbulence-chemistry interaction. For both problems many approaches were developed over the years, though there is no general solution. A brief introduction with emphasize on the models employed in section 4.1.2 is given.

2.3.1 Chemistry

To simulate combustion, equations for all species and enthalpy need to be solved (see Eqns. 4.12 and 4.15). For complex reaction mechanisms a high number of species leads to long simulation times. One strategy to speed up simulations is to use reduced mechanisms. But especially for high temperature auto-ignition this can lead to erroneous results [Boi11]. Another strategy is tabulated chemistry in combination with a progress variable [BPF06, KP12, PI04]. The progress variable can be the mass fraction of one species representing the radical pool [BPF06] or the sum of mass fractions of several species [KP12, PI04]. The advantage of tabulated chemistry is that detailed mechanisms can be used. Look-up tables for the source term of the progress variable and enthalpy equation can be processed with simple and fast reactor simulations prior the computational fluid dynamics (CFD) simulation. Entries might be listed as a function of fuel mixture fraction and other thermodynamic properties e.g. pressure or temperature.

2.3.2 Flamelet Model

In the present work the diffusive and reactive mixing layer that is formed between fuel and oxidator (see also Fig. 2.5) shall be simulated. A combustion model with the following characteristics is required for this task:

- Chemistry and flow shall be calculated separately from each other, because it should be possible to use measurement data as input for the combustion simulation.
- Timescales of flow and chemistry are in the same range, therefore unsteady equations need to be applied that consider chemical kinetics.
- As non-premixed or partially premixed conditions are assumed, the model has to be able to compute combustion near to stoichiometry.
- A combustion model with a low number of equations is needed as computational times shall be minimized.

In the current work the "Lagrangian Flamelet Model" by Pitsch [Pit00], that applies the unsteady flamelet equations of Peters [Pet84] is applied. With this model wherein the flamelets are transported convectively through the flow the requirements above can be fulfilled. In this section an overview of the derivation of the flamelet model is given.

The balance equations for species and enthalpy may be written as [Pet84]

$$\rho \frac{\partial Y_i}{\partial \tau_x} + \rho u_j \frac{\partial Y_i}{\partial x_j} = \dot{w}_i - \frac{\partial j_{ij}}{\partial x_j}, \tag{2.15}$$

$$\rho \frac{\partial h}{\partial \tau_x} + \rho u_j \frac{\partial h}{\partial x_j} - \frac{\partial}{\partial x_j}\left(\frac{\lambda_T}{c_p}\frac{\partial h}{\partial x_j}\right) = -\frac{\partial}{\partial x_j}\sum_{i=1}^{n} h_i \left(\frac{\lambda_T}{c_p}\frac{\partial Y_i}{\partial x_j} + j_{ij}\right) + \frac{\partial p}{\partial \tau_x} + q_R. \tag{2.16}$$

ρ represents the density, Y the mass fraction, τ_x the time, the index i the species, n the number of species and the index j denotes the three directions in space. j_{ij} is the diffusion flux of species i, u the velocity, x the direction and $\dot{w}$ the chemical

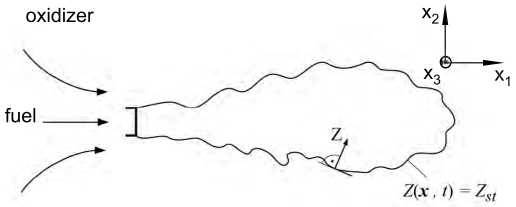

Figure 2.5: Schematic representation of the coordinate transformation.

source term. q_R corresponds to the heat loss due to radiation, h to the specific enthalpy, c_p to the specific heat capacity, λ_T to the thermal conductivity and p to the pressure.

The details of the derivation of the flamelet equations can be found in the paper of Peters [Pet84]. He assumes that the mixture fraction is given in the whole flow field as a function of time and space. Peters introduces an oblique coordinate system attached to the surface of stoichiometric mixture. The coordinate x_1 is replaced by the mixture fraction Z and the original coordinate system is defined such that x_1 does not lie within the surface of stoichiometric mixture (see Fig. 2.5). By definition, the new coordinate Z is locally normal to the surface of stoichiometric mixture. Using $Z_2 = x_2$, $Z_3 = x_3$ and $t = \tau_x$, Peters transforms Eqns. 2.15 and 2.16 to the set of unsteady flamelet equations. The equations are valid for a coordinate system that is moving with the flow. By neglecting terms of higher order, all terms with Z_2 and Z_3 disappear, therefore the equations become one-dimensional:

$$\rho \frac{\partial Y_i}{\partial t} = \rho D_Z (\nabla Z)^2 \frac{\partial^2 Y_i}{\partial Z^2} + \dot{w}_i, \tag{2.17}$$

$$\rho \frac{\partial T}{\partial t} = \rho D_Z (\nabla Z)^2 \frac{\partial^2 T}{\partial Z^2} - \sum_{i=1}^{n} \frac{h_i}{c_p} \dot{w}_i. \tag{2.18}$$

In Eqns. 2.17 and 2.18 the following simplifications were made:

- in gaseous flows the Lewis number ($Le = \frac{Sc}{Pr}$) is approximately one,
- terms of higher order are ignored,
- heat losses due to radiation are neglected ($q_R = 0$),

- an isobaric system is assumed ($\frac{\partial p}{\partial t} = 0$),
- the variable heat capacity is only considered in the calculation process of the source term $\sum_{i=1}^{n} \frac{h_i}{c_p} \dot{w}_i$, therefore the temperature calculated by the flamelet equation 2.18 has to be assumed as being an approximation only.

The influence of the flow field is introduced into the equations by the instantaneous scalar dissipation rate χ defined by

$$\rho \frac{\chi}{2} = \rho D_Z (\nabla Z)^2 . \tag{2.19}$$

With the dimension one per second it may be interpreted as the inverse of a characteristic diffusion time. Due to the transformation it incorporates implicitly the influence of diffusion normal to the surface of stoichiometric mixture. Figure 2.6 shows a schematic solution for the temperature profile. The inner reaction zone is embedded by two chemically inert outer zones. Disturbances, which act via χ on the flame structure, are transmitted from the inner to the outer zones which are described by the balance of unsteady and diffusive term in Eqns. 2.17 and 2.18 [Pet84].

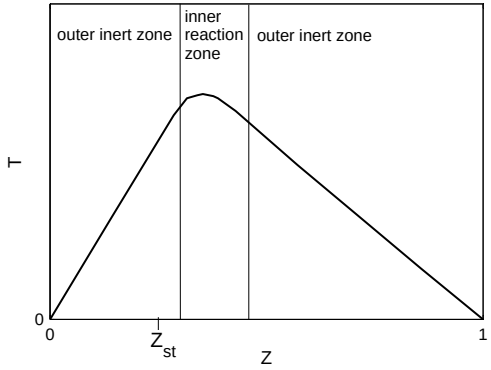

Figure 2.6: Schematic representation of the flamelet structure. Temperature is plotted as a function of mixture fraction. From Peters [Pet84].

Following Pitsch [Pit00], the scalar dissipation rate can be correlated with the mixture fraction by the equation

$$\chi = \chi_{st} f(Z), \tag{2.20}$$

with

$$f(Z) = \frac{Z^2}{Z_{st}^2} \cdot \frac{\ln Z}{\ln Z_{st}}. \tag{2.21}$$

Nilsen and Kosály [NK99] showed in their study on decaying turbulence in an initially non-premixed system employing *direct numerical simulation* (DNS) that a function similar to Eqn. 2.21 provides a good estimate for the relationship between mixture fraction and the scalar dissipation rate.

In terms of the k - ε turbulence model, the time averaged scalar dissipation rate can be expressed as

$$\bar{\chi} = c_\chi \frac{\bar{\varepsilon}}{\bar{k}} \widetilde{Z''^2}, \tag{2.22}$$

with the common estimate $c_\chi = 2.0$ [Pet84]. $\widetilde{Z''^2}$ denotes the mixture fraction variance that is gained in this work from water channel measurements. Equation 2.20 shows that the scalar dissipation rate only depends on its stoichiometric value and the mixture fraction. Statistical independence presumed, Pitsch [Pit00] states that the turbulent mean of the scalar dissipation rate can be written as

$$\bar{\chi} = \langle \chi_{st} \rangle \int_Z f(Z) P(Z) dZ, \tag{2.23}$$

wherein P denotes a PDF and $\langle \chi_{st} \rangle$ the mean scalar dissipation rate conditioned on Z_{st}. With Eqns. 2.21, 2.22 and 2.23, $\langle \widetilde{\chi_{st}} \rangle$ can be expressed as

$$\langle \widetilde{\chi_{st}} \rangle = \frac{c_\chi \frac{\bar{\varepsilon}}{\bar{k}} \widetilde{Z''^2}}{\int_0^1 \frac{Z^2}{Z_{st}^2} \frac{\ln Z}{\ln Z_{st}} P(Z) dZ}. \tag{2.24}$$

The flamelet equations Eqn. 2.17 and Eqn. 2.18 are solved using Eqn. 2.20 with Eqn. 2.21 and the definition $\chi_{st} \equiv \langle \widehat{\chi_{st}} \rangle$ from Pitsch [Pit00], wherein the hat identifies the mean of $\langle \chi_{st} \rangle$ over a certain volume.

The implementation of the flamelet equations in Matlab is explained in detail in chapter 4. Tabulated detailed chemistry in combination with a progress variable is applied.

2.3.3 Turbulence-Chemistry Interaction

In this study flames in turbulent flow are investigated. Therefore, turbulence has to be taken into account. In section 2.1.3 it was shown that auto-ignition strongly depends on temperature. The enthalpy of a fuel/oxidator mixture can be approximated using the following equation:

$$h = h_{fuel} Z + h_{\infty}(1 - Z). \tag{2.25}$$

In non-premixed or partially premixed systems Z also represents fluctuations due to turbulence, therefore enthalpy fluctuates. To consider such fluctuations in time averaged simulations, mean flow properties or reaction rates can be calculated with a probability density function (PDF) of the mixture fraction [Bra05]:

$$\overline{\xi} = \int_{-\infty}^{\infty} \xi(Z) P(Z) dZ. \tag{2.26}$$

Herein ξ can be an arbitrary value that depends on mixture fraction and P is the PDF of Z. The problem of this approach is that the mixture PDF is determined by diffusive and convective mixing processes. According to Brandt [BPF06] there are two methods in use to determine the shape of the PDF:

- *Presumed PDF method:* Prior to the CFD-simulation, the shape of the PDF is selected (β or Gaussian distribution), therefore look-up tables for reaction rates can be created. Distributions are selected so that they can be parametrized by functions of mean value and variance. In the CFD-simulation, transport equations for mean value and variance are solved. Reaction rates as a function of mean value and variance can then be extracted from the look-up tables.

- *Transported PDF method:* This approach might be necessary in highly turbulent flows where extinction and reignition events due to turbulence-chemistry interaction occur. The transport-PDF equation is a high-dimensional equation and therefore time-demanding to be solved [BPF06]. A transported PDF is usually represented by an ensemble of particles with mass, though the number of particles is limited by memory size and computational power. In this work a fast simulation method is needed, therefore the transported PDF method is not pursued any further.

In this study a particular type of the presumed PDF method is used: The PDF is obtained from water channel measurements. The advantage of this method is that uncertainties occurring due to presumed PDF simulation models can be avoided, however it must be assumed that the results are directly transferable. In order to use measurement data, CFD-simulation and combustion simulation are separated from each other. For the flow, RANS simulations are used.

2.4 Chemiluminescence

The term "chemiluminescence" refers to radiation emitted from chemically created excited radicals [Nor08]. The radiation is the output of a spontaneous transition of the excited molecule to the ground state. The excitation energy comes from a chemical reaction [Cam10]. Combustion processes involve unstable species that emit chemiluminescence. Therefore chemiluminescence emissions from various species are often used as a combustion diagnostic tool. This work deals with the emission from the excited molecules OH*, CH* and CO_2*. The asterisk indicates excited molecules.

Changes the state of the electrons of a molecule (e.g.: OH* $\rightarrow$ OH), light in the visible and ultra-violet regions is emitted. Due to the vibration and rotation of the molecule, the energetic level is divided in vibrational and rotational sub levels. Only discrete energy states are possible.

In the course of this study only vibrational states are observed as the resolution of the spectrally resolved chemiluminescence measurements is not high enough to investigate rotational states. Lauer [Lau11] states that the transition between identical vibrational states ($\Delta v = v' - v'' = 0$) is a good approximation for the total number of OH* molecules. Therefore it is assumed that the measurement of this transition which gives the strongest signal (see Fig. 2.7) is sufficient.

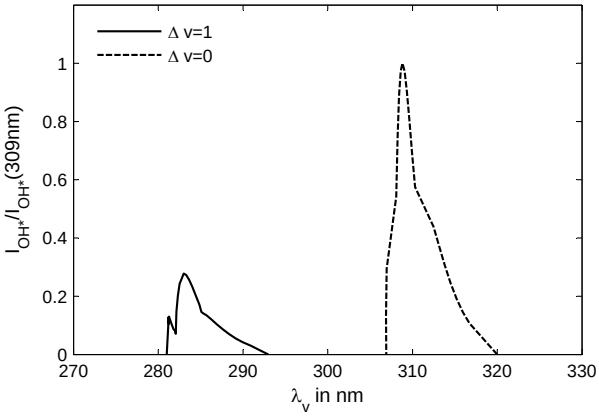

Figure 2.7: Normalized intensity as a function of wavelength. OH* emission spectrum at 2200 K and atmospheric pressure. Vibrational bands from $\Delta v = 1$ and $\Delta v = 0$. Calculated with HITRANS [RGB$^+$09].

Figure 2.8 shows a sketch of the steps on which the net photon emission due to chemiluminescence from an excited molecule (OH*, CH*, CO_2*) depends [Nor08]:

- excited state formation via chemical reaction (F):

$$\Xi + \Psi\Omega \rightarrow \Xi\Psi^* + \Psi, \tag{2.27}$$

- excited state formation via thermal excitation (T):

$$\Xi\Psi \rightarrow \Xi\Psi^*, \tag{2.28}$$

- collisional quenching reactions that remove the excited state, reducing to its ground electronic configuration non-radiatively (Q):

$$\Xi\Psi^* + \Gamma \rightarrow \Xi\Psi + \Gamma, \tag{2.29}$$

- reactive collision with another molecule (R):

$$\Xi\Psi^* + \Psi \rightarrow \Xi + \Psi_2, \tag{2.30}$$

- spontaneous radiative transitions to the ground state (S):

$$\Xi\Psi^* \rightarrow \Xi\Psi + \check{h}\nu, \tag{2.31}$$

wherein $\check{h}$ denotes the Planck constant and ν the frequency of chemiluminescent emission.

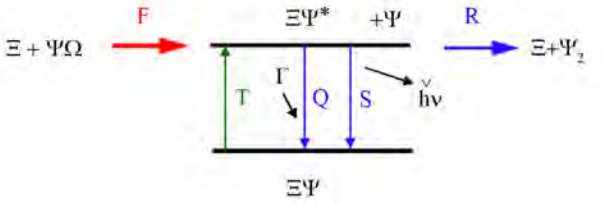

Figure 2.8: Sketch of possible chemiluminescence reactions, based on Nori [Nor08].

In a stationary flame the formation and deactivation of electronically excited radicals are in equilibrium [Lau11]. Therefore it can be assumed that the concentration of radicals is in quasi-steady state [SEB95]. For an excited state $\Xi\Psi^*$ according to Nori [Nor08] the following equation holds:

$$\frac{d[\Xi\Psi^*]}{dt} \approx 0 = F + T - Q - R - S. \tag{2.32}$$

In this study combustion with preheated air is considered. Even for stoichiometric mixture it can be shown that the flame temperature is below the limit postulated by [FS13, DLSKZ07] for thermal excitation (T). Therefore the latter is neglected in the chemiluminescence simulations. Furthermore, reactive collision with another molecule (R) is not considered as collisional quenching reactions (Q) dominate [Nor08].

The concentrations of OH* and CH* are simulated by taking excited state formation via chemical reactions (F), collisional quenching reactions (Q) and spontaneous radiative transitions (S) into account. Panoutsos et al. [PHT09] investigate in their work eight different reaction mechanisms for OH* and CH*. All mechanisms give comparable tendencies, though the absolute values vary. For this work a mechanism proposed by Panoutsos et al. is used. Therein OH* formation reactions are taken from Porter et al. [PCKB67], CH* formation reactions from Devriendt et al. [DVLCP96] and collisional quenching data from Tamura et al. [TBH+98].

This mechanism appears to approximate measurement data most accurately. It is presented in detail in section 4.2 (Tab. 4.2).

2.4.1 Calculation of Species Concentrations

Reaction rate coefficients k_R are calculated using the modified Arrhenius equation [PHT09]:

$$k_R = A_A T^B exp\left(-\frac{E_A}{RT}\right), \tag{2.33}$$

wherein A_A is the pre-exponential factor, T the temperature, B the temperature exponent, E_A the activation energy and R the universal gas constant. Only forward reaction rate coefficients are considered.

The following example shall explain the calculation of concentrations of the chemiluminescence species:

Quasi-steady state concentration is assumed:

$$\frac{d[\Xi\Psi^*]}{dt} \approx 0 = F - Q - S. \tag{2.34}$$

Using the concentrations of the left hand side species of Eqns. 2.27, 2.29, 2.31 and their forward rate coefficients, Eqn. 2.34 can be written as:

$$0 = k_{R,F}[\Xi][\Psi\Omega] - k_{R,Q}[\Xi\Psi^*][\Gamma] - A_{\Xi\Psi^*}[\Xi\Psi^*], \tag{2.35}$$

with the Einstein coefficient $A_{\Xi\Psi^*}$ as the rate coefficient for the spontaneous radiative transition to the ground state.

Rearranging Eqn. 2.35, the concentration of the chemiluminescent $[\Xi\Psi^*]$ can be calculated from the relation:

$$[\Xi\Psi^*] = \frac{k_{R,F}[\Xi][\Psi\Omega]}{k_{R,Q}[\Gamma] + A_{\Xi\Psi^*}}. \tag{2.36}$$

In section 4.2.2 Eqn. 2.36 is applied to determine the concentrations of OH* and CH* by using species concentrations obtained from reactor simulations (see section 4.2.1).

2.4.2 Chemiluminescence as Diagnostic Tool

Particular care needs to be taken in interpreting the results of chemiluminescence measurements. OH* or CH* emissions are often used to measure local heat release rates, though studies of Hurle et al. [HPST68], Najm et al. [NPMW98], Lee and Santavicca [LS03], Ayoola et al. [ABF$^+$06] and Lauer and Sattelmayer [LS10] show that those measurements lead to errors in turbulent flames. The reason for this is that the chemiluminescence signals of all emitting species are strongly affected by turbulence intensity, strain rate, curvature, degree of premixing and air excess ratio.

The air excess ratio, however, can be determined reliably at atmospheric pressure from the OH*/CH* chemiluminescence ratio of a methane or propane fueled flame, as shown by Haber [Hab00], Panoutsos et al. [PHT09], and Guyot et al. [GGS$^+$10]. Higgins et al. [HMLC01, HML$^+$01] evaluated in detail OH* and CH* chemiluminescence emissions of a laminar methane/air flame at varying operation conditions. They recorded bandpass filtered chemiluminescence emissions with a photo multiplier tube (PMT) at varying air excess ratios and pressures from 5 bar to 25 bar. According to those measurements, the air excess ratio is proportional to the following power law:

$$\lambda \propto \left(\frac{I_{OH^*}}{I_{CH^*}} \right)^{-0.4} \cdot p^{-0.09}. \tag{2.37}$$

Wherein I_{OH^*} and I_{CH^*} are the emission intensities of the species OH* and CH* and p denotes the pressure. Higgins et al. do not consider the broadband emission of CO_2* in their studies, though the chemiluminescence emission of this species plays an important role, as shown in section 3.3.3.

Ikeda et al. [IKH02], who investigated a laminar high pressure (up to 15 bar) methane/air flame also report a weak pressure dependency of the OH*/CH* ratio. Muruganandam et al. [MKM$^+$05] show in their study chemiluminescence measurements of a turbulent natural gas/air flame at pressures of up to 7.8 bar and report of nonmonotonic behavior of the OH*/CH* ratio at varying air excess ratios with increasing pressure. Furthermore they state that the preheat temperature has a low effect on the chemiluminescence ratio.

In a numeric study, Nori and Seitzman [NS08] analyzed the effects of pressure, preheat temperature and reactant product mixing on the OH*/CH* ratio. They found a weak influence of preheat temperature and reactant product mixing, but

a strong influence of pressure. According to their work, the dependence of the OH*/CH* ratio on the air excess ratio almost disappears at five bar and with increasing pressure the OH*/CH* ratio decreases with increasing air excess ratio.

Konishi et al. [KKA02] investigate a vitiated propane flame and report that chemiluminescence intensities decrease with increasing inlet temperature and decreasing oxygen content in the oxidator. They do not give any ratios of chemiluminescence emissions.

In summary there are many studies that show a reliable correlation between the OH*/CH* ratio and the air excess ratio at atmospheric pressure. In case of laminar flames a weak dependency of the chemiluminescence signal on pressure is reported. For turbulent pressurized flames Nori and Muruganandam found a non-monotonic behavior between air excess ratio and OH*/CH* ratio at pressures from three to eight (Muruganandam et al.) and beyond five bar (Nori and Seitzman). The effect of preheat temperature is said to be weak, but has only been investigated up to a preheat temperature of 698 K by Nori and Seitzman [NS08]. In the current work the oxidator is preheated up to 1205 K.

2.5 Linear Regression Analysis

A statistical tool for estimating the relationships among variables is called regression analysis. Linear regression analysis tries to find a linear function that assigns to every ξ-value a ζ-value [BZ09]. ξ is called the independent variable (parameter set in the experiment e.g.: temperature) and ζ the dependent variable (measured value e.g.: lift-off height). A multiple linear regression analysis tries to find a linear function with more than one independent variable that describes one dependent variable. The function has the following form:

$$\zeta = a + b_1 \cdot \xi_1 + b_2 \cdot \xi_2 + \cdots + b_N \cdot \xi_N, \tag{2.38}$$

where a is a constant, $b_{1\ldots N}$ are the coefficients, $\xi_{1\ldots N}$ are the independent variables and ζ is the dependent variable.

A requirement for a linear regression analysis is that there is a linear relation between the variables. Figure 2.1 shows that ignition delay does not depend linearly on temperature. Therefore it can be assumed that a measured value as e.g.: lift-off height is a non-linear function of temperature, too.

Hence, a function of the form

$$\zeta = a \cdot \xi_1^{b_1} \cdot \xi_2^{b_2} \cdot \ldots \cdot \xi_N^{b_N}, \tag{2.39}$$

is assumed.

To use linear regression, Eqn. 2.39 is transformed to a linear equation:

$$log(\zeta) = log(a) + b_1 log(\xi_1) + b_2 log(\xi_2) + \cdots + b_N log(\xi_N). \tag{2.40}$$

By taking the logarithm of the measurement data it is possible to find the exponents $b_{1\ldots N}$ with linear regression analysis for Eqn. 2.39.

In the present study SPSS [Cor12] is used to perform multiple linear regression analysis of experimental data. In the following, terms are explained that need to be understood to interpret the results.

2.5.1 Correlation

The basis of linear regression analysis are correlations. A correlation (r) reflects the relation between two variables, stating whether the manifestation of one variable (ξ) corresponds with the manifestation of another variable (ζ) [BZ09]. Values for correlations can vary between -1 and 1. The nearer the correlation comes to the values minus one or plus one, the higher the relation between the two variables. A correlation near to zero means almost no relation between the two variables.

The correlation of multiple regression analysis is also referred to as R. The square of the correlation value (R^2) is the determination coefficient. Its value can be interpreted as the percentage of differences of the dependent variable that can be predicted by differences of the independent variables. Bühner and Ziegler [BZ09] give the following ranges for the determination coefficient:

- $R^2 = 0.02 \rightarrow$ low predictive power,
- $R^2 = 0.13 \rightarrow$ mean predictive power,
- $R^2 = 0.26 \rightarrow$ high predictive power.

2.5.2 Null-Hypothesis

In statistical studies the null-hypothesis refers to the case where there is no relation between independent and dependent variable. Therefore the aim is to reject the null-hypothesis. To decide whether the null-hypothesis can be rejected, hypothesis tests are conducted. The outcome of such tests can be a *p-value* which is a probability value and an indicator for statistical significance.

2.5.3 Statistical Significance

The probability that a seen effect is not the result of a sampling error or just happened by accident is named *statistical significance*. For multiple linear regression all independent variables are tested whether they are statistically significant to find out whether the seen effects due to a change of one parameter are not due to chance alone. For *p-values* below 0.05 independent variables are assumed to be statistically significant. Whether independent variables that are not statistically significant are considered any further needs to be decided individually. Reasons for independent variables not becoming statistically significant could be too little data or the way experiments are conducted.

3 Experimental Investigations

In this chapter the experimental setups for the combustion experiments and the cold measurements done by Haner [HTH+13] in the water channel are presented. The high pressure test rig (see Fig. 3.1) used for the hot experiments is described. Furthermore, the setups employed for optical- and temperature measurements are shown.

3.1 Combustion Experiments

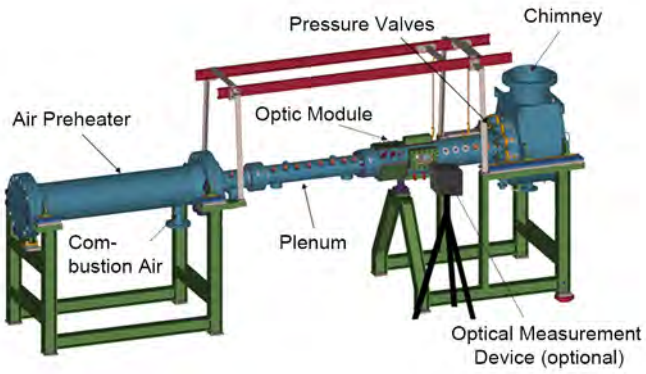

Figure 3.1: Scheme of the test rig [THHS13, THHS14].

3.1.1 Test Rig

Freitag [FKL+06] built the test rig in close cooperation with Tresch+Kieliger Engineering and Apparatebau Dössegger of Egliswil, Switzerland in 2003. The main

parts of the rig are the air preheater, the plenum, a hot, water-cooled, optically accessible module and a valve disk with hot gas valves. The air is preheated up to 770 K by four electric heaters. In the wall of the plenum there are one-inch apertures that can be used to perform measurements or for supply pipes. The plenum is followed by the optics module into which different burner geometries can be mounted. Here, two face-to-face arranged windows allow optical access to the flame. The inner diameter of the test rig is 150 mm, the length of the rectangular windows is 150 mm and their height is 90 mm. Therefore $3/5$th of the combustion chamber's diameter can be observed. On both sides of the optics module, flanges are integrated to ease the changing of setups. After the optics module two water cooled modules follow – the base module and the extension module. Each of those has four one-inch apertures that can be used to apply measurement techniques. In this area exhaust gas measurements after the flame can be performed. The last element of the pressurized parts of the test rig is the valve support disk with nine water cooled, adjustable hot gas valves. Finally the flue gas exits the lab through the chimney.

The maximum pressure is limited by the air supply and amounts to 10 bar at a mass flow of $300\,\mathrm{g\,s^{-1}}$. There are two air supplies: one is used for the combustion air, the other for cooling air and bypass air. Bronkhorst mass flow controllers are used to adjust the fuel mass flows.

In the course of this study, three types of flames need to be investigated: a perfectly premixed swirl flame, a premixed auto-igniting flame and a non-permixed auto-igniting flame. Therefore, the following three burner configurations are necessary:

3.1.2 Generic Swirl Burner

A swirl stabilized flame is observed in the measurements where the combustion air is preheated electrically. In this case the vitiator (see next section) is used to premix fuel and air. The mixture then enters the burner, which is described in detail in [SMS11, MSS+12]. The burner consists of a conical four-slot swirler, a convergent mixing tube and a diffuser (see Fig. 3.2). The convergent mixing tube and the diffuser are water cooled. The configuration is mounted in the upstream part of the window module. The flame stabilizes in the downstream part where it can be observed through the fused silica windows. The burner is operated at air mass flows from $20\,\mathrm{g\,s^{-1}}$ at 1 bar up to $60\,\mathrm{g\,s^{-1}}$ at 3 bar. These mass flows lead to Reynolds numbers ranging from 30 000 to 90 000. Therefore the flow is fully turbulent.

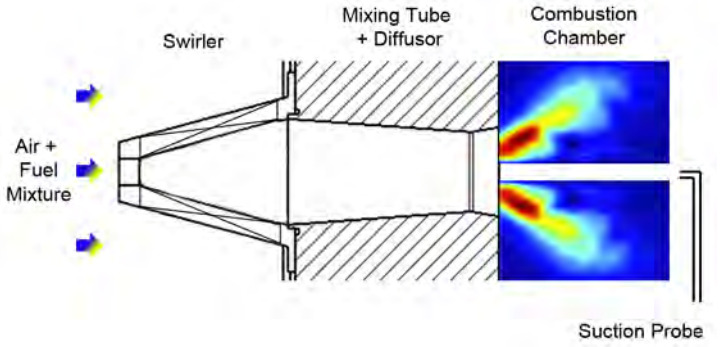

Figure 3.2: Sketch of the generic swirl burner.

3.1.3 Vitiator

For auto-ignition, hot gas needs to be provided. In this study this is done by the vitiator that is integrated in the plenum section of the test rig. Figure 3.3 shows a sketch of the vitiator. It has a premixed swirl burner with fuel injection downstream of the swirler and a lance cooled by the fuel. As the vitiator is designed to provide hot gases at air excess ratios around 2 to 4, the flow is split into a combustion and a dilution flow. Approximately 60 % of the main air flow are used for combustion. This way local air excess ratios from 1.5 to 2.7 are obtained in the combustor. On flange (2) (see Fig. 3.3) there is a rib, which allows the adjustment of the air split by moving the front panel. The liner is cooled by the combustion air which also reduces heat losses. Employing electrical air preheat provides an additional degree of freedom which allows decoupling of the outlet temperature from the oxygen content to a certain degree. The rest of the air is mixed with the flue gas through six apertures that are distributed on the circumference of the vitiator's liner, located three diameters downstream of the position where the flame stabilizes. Flue gas exits the vitiator at temperatures up to 1500 K.

Thermal Model of the Vitiator

The inlet temperature to the second combustion stage depends on the operating conditions of the vitiator. Temperature measurements of the main flow at the inlet

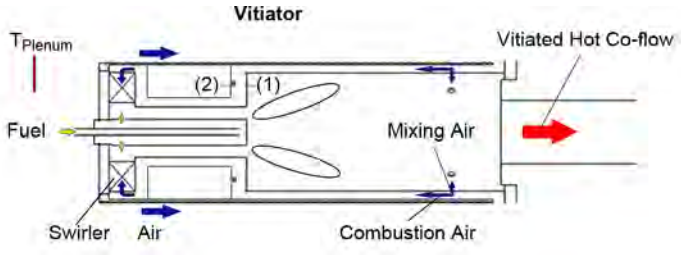

Figure 3.3: Sketch of the vitiator.

of the second combustion chamber show that the calculated adiabatic flame temperature is distinctly too high. Therefore heat losses to the cooling water have to be considered. From cooling water temperatures, measured at different points along the test rig and the cooling water mass flow, the increase in enthalpy, which is assumed to be similar to the heat losses of the co-flow, is calculated. The resulting curve is plotted as a function of the oxidator's pressure in Fig. 3.4. By considering the heat losses to the cooling water in the enthalpy balance, the inlet temperature to the second combustion stage $T_{in,2}$ is determined.

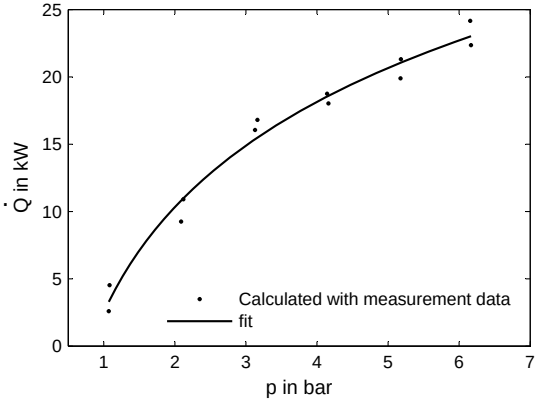

Figure 3.4: Heat losses to the cooling water as a function of pressure.

3.1.4 Sequential Combustor – Design Principles

To determine the operating parameters and the design of the sequential combustor, ALSTOM's SEV burner is used as reference. As mass flow and pressure of the SEV lie beyond the capabilities of the test rig, scaling rules need to be considered. For scaling, dimensionless parameters might be used such as Reynolds or Damköhler number. However for sufficiently large Reynolds numbers it can be assumed that the dependence on the Reynolds number vanishes. Therefore only a Damköhler number is considered to obtain the scaling for the experimental setup. As auto-ignition is the key process, the following Damköhler number is used:

$$Da_{AI} = \frac{\text{characteristic turbulent time}}{\text{auto-ignition time}} = \frac{\tau_T}{\tau_{AI}}, \tag{3.1}$$

with

$$\tau_T = \frac{l_T}{u'_{rms}}. \tag{3.2}$$

Here l_T is the turbulent length scale that is proportional to the hydraulic diameter D_h and u'_{rms} represents the root mean square velocity of fluctuation that is proportional to the bulk velocity u_∞. Therefore it can be written:

$$\tau_T \propto \frac{D_h}{u_\infty}. \tag{3.3}$$

The bulk velocity is a function of mass flow, area and density.

$$u_\infty = \frac{4\dot{m}}{D_h^2 \pi \rho}. \tag{3.4}$$

To get well understood flow structures in the experiment, a circular geometry is chosen. Therefore the hydraulic diameter is equal to the pipe diameter. The characteristic flow time is proportional to:

$$\tau_T \propto \frac{\pi D_h^3 \rho}{4\dot{m}}. \tag{3.5}$$

With the correlation of Spadaccini and Colket [SC94] (see Eqn. 2.5), auto-ignition times for SEV-burner and experiment are calculated. With the assumption

$$Da_{SEV} = Da_{Exp}, \tag{3.6}$$

the Eqns. 3.5 and 3.1, the following relation for the mass flow in the experimental setup can be found:

$$\dot{m}_{Exp} = \frac{D_{Exp}^3 \cdot \rho_{Exp} \cdot \tau_{AI,SEV} \cdot \dot{m}_{SEV}}{D_{h,SEV}^3 \cdot \rho_{SEV} \cdot \tau_{AI,Exp}}. \tag{3.7}$$

A pipe with an inner diameter of 64 mm is chosen for space constraints of the pressure vessel. At 6 bar a mass flow of $\approx 130\,\mathrm{g\,s^{-1}}$ is deduced from Eqn. 3.7. For lower pressures the mass flow is set in such a way that the flow velocity remains constant. Discrepancies between the calculated mass flows and the true mass flows are the result of leakages and measurement inaccuracies of the mass flow controllers of the air supply. The actual mass flow is calculated from the oxygen content in the flue gas and the fuel mass flow.

3.1.5 Sequential Combustor – Premixed Operation

For chemiluminescence investigations a premixed flame needs to be provided in the sequential combustion section. The two main parts of the combustor are the vortex generator and the fuel injector. In a high temperature steel pipe with an inner diameter of 64 mm the vortex generator is mounted. Shortly after the tip of the vortex generator the fuel is injected through a 14 mm wide orifice. Through a slot that is concentric to the fuel injection, additional cold air can be injected to avoid flashback and improve mixture uniformity. Three diameters after the fuel injector follows an area expansion with an area ratio of 1:2.95, which reflects the SEV geometry.

The flame stabilizes few centimeters after the area expansion. NO_x measurements are done to determine the quality of the mixture. The measured values are close to these of perfect premixed flames which indicates that the flame in the second stage is also well premixed (reference data from [Sat03]). 70 mm of the pipes upstream and downstream of the area expansion are made of fused silica with an inner diameter of 64 mm and 110 mm, respectively. They are mounted at the same

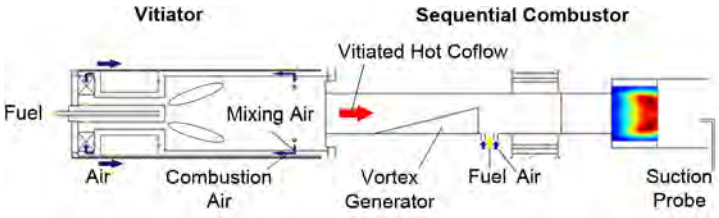

Figure 3.5: Sketch of the vitiator and the sequential combustor – premixed configuration.

axial position as the plane fused silica windows of the window module. Therefore the flame of the sequential combustor can be observed from outside. Between the outer and the inner windows additional air is injected for cooling purposes. The burner is operated at air mass flows from 20 g s^{-1} at 1 bar up to 60 g s^{-1} at 3 bar. This results in Reynolds numbers ranging from 8000 to 24 000.

3.1.6 Sequential Combustor – Non-Premixed Operation

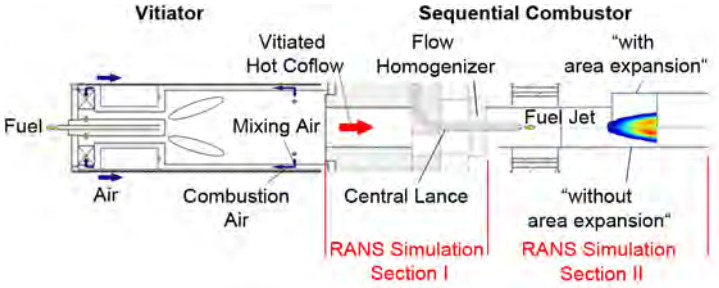

Figure 3.6: Sketch of the vitiator and the sequential combustor – non-premixed configuration.

To investigate parameters affecting auto-ignition, a non-premixed configuration is implemented in the sequential combustion section. The setup covering both combustion stages is shown in Fig. 3.6. The section between vitiator and sequential combustor is equipped with high temperature insulation on the inside to reduce heat losses to the test rig walls. The sequential combustor is located in the window

(a) High temperature insulation attached to the perpendicular part of the central lance. High temperature insulation upstream of the shown part is dismantled.

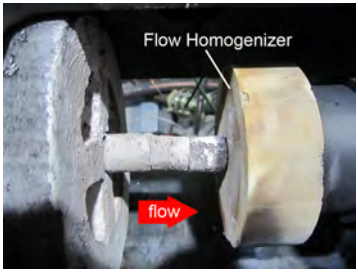

(b) Image of the flow homogenizer. Parts of high temperature insulation are dismantled.

Figure 3.7: Images of the experimental setup.

module. A water cooled lance with a diameter of 10 mm is mounted in an orifice of the test rig wall, therefore it is bent 90° to be parallel to the flow. The diameter of the fuel nozzle at the downstream end of the lance is 2 mm. High temperature insulation (see Fig. 3.7a) is attached to the part of the lance that is perpendicular to the main flow. The insulation is cross-shaped to avoid an asymmetric flow field, though section 5.1.2 shows that this approach is only partially successful. Approximately 50 mm downstream of this insulation, a flow homogenizer (see Fig. 3.7b) made of ceramics is installed. After the flow homogenizer the lance is concentric with the 64 mm duct. Downstream of the flow homogenizer the first 120 mm of the 64 mm duct are made of metal. Two configurations can be applied after it:

- a straight fused silica duct with an inner diameter of 64 mm and a length of 300 mm, later referred to as “without area expansion”,
- the configuration “with area expansion” already explained in section 3.1.5.

The distance between nozzle and area expansion corresponds to 70 nozzle-diameters. Cold air is injected between the inner test rig walls and the fused silica pipes for cooling purposes. Measurements are conducted between 1 and 6 bar at almost constant flow velocities. Mass flow rates of the main flow between 20 $\mathrm{g\,s^{-1}}$

at 1 bar up to $120\,\mathrm{g\,s^{-1}}$ at 6 bar result in Reynolds numbers of ≈ 8000 at 1 bar up to $\approx 45\,000$ at 6 bar.

All combustors are fueled with natural gas with an average composition of 96.18 % CH_4, 1.8 % C_2H_6, 0.48 % C_3H_8, 1 % N_2, 0.35 % CO_2 and 0.19 % higher hydrocarbons [SWM11]. For the simulations the amount of higher hydrocarbons is added to C_3H_8 as this is the highest hydrocarbon available in the GRI3.0 mechanism.

The test runs are conducted as follows: First the vitiator is adjusted to the nominal operating point and the oxygen content in main flow is measured for cross-checking. Then the fuel mass flow in the sequential combustor is gradually increased to its target value and the pressure is adjusted by regulating the amount of bypass air that is blown into the combustor upstream of the backpressure valves. When the parameters are stable, the optical measurements are conducted.

3.2 Water Channel

Due to a better optical access, cold flow mixture measurements were done by Haner [HPHS12] in the water channel which is explained in detail in [SMS11]. The model employed in the water experiment is twice the size of the combustion experiment in order to achieve high spatial resolution. Only the regions near the central lance are of interest in the isothermal measurements. Mass flows are selected to reach similar momentum flux ratios as in the combustion experiment. According to Brückner-Kalb et al. [BKKHS10] the momentum flux ratio is defined as

$$J = \frac{\rho_0 u_0^2}{\rho_\infty u_\infty^2}, \tag{3.8}$$

wherein the index 0 denotes the jet and ∞ the main flow. u represents the velocity and ρ the density of the jet and main flow, respectively. Planar Laser Induced Fluorescence (PLIF) measurements with Uranin fluorescent dye [BAS00] are performed in order to acquire mixture PDFs and the mixture variances of the fuel jet. Up to 8000 images with a resolution of 2.5 pixels per mm are recorded. The measurement section is divided into 45x65 rectangular sections representing 21 diameters in radial and 65 diameters in axial direction. For each PDF an area of ± 3 pixels around the evaluated point is analyzed. Each PDF consists of 256 bins.

3.3 Measurement Setups

Below the optical measurement techniques used to determine the lift-off height and the shape of the auto-ignition flame are introduced first. Furthermore, techniques are presented to determine the air excess ratio in the flame. At the end of section 3.3, temperature measurements with a two-thermocouple temperature probe are explained.

3.3.1 Lift-off Height

To detect the lift-off height and the shape of the flame, high speed chemiluminescence images of the ignition events are taken. For these measurements, a BrightLine bandpass filter from Semrock (320 ± 20 nm) is used. 1000 images with a resolution of 1024 x 512 pixels at 1000 frames per second and an exposure time of 50 μs to 70 μs are recorded with a Fastcam APX II image intensified high speed camera from Photron. In all images shown subsequently flow direction is from left to right.

In a post-processing step the images are analyzed in Matlab to detect the lift-off height: Each single image is scanned from left to right until pixels with more than a predefined threshold value are found. From a reference image, the correlation between pixel and distance from injector-nozzle (given in nozzle-diameters) is known. Hence it is possible to evaluate the lift-off height in nozzle-diameters in every single image. In order to count auto-ignition events only, the lift-off height determined in the current image is compared with the one in the previous image. If the difference equals the flow velocity times the time difference between the images, it is assumed that a traveling flame kernel has been detected and the current lift-off height is discarded. The arithmetic mean axial location of all observed ignition kernels presented in the results section is calculated on the basis of 1000 images per operating point.

The way of determining the air excess ratio and the different optical measurement setups are presented in the following sections.

3.3.2 Air Excess Ratio

The oxygen content downstream of the flame is used to calculate the global air excess ratio. To measure the flue gas composition, a water cooled suction probe is mounted in the base module.

The global air excess ratio is an indirect measurement value, calculated from the O_2 or CO_2 content in the flue gas [BK08]. In order to compute the air excess ratio for hydrocarbons with the general chemical formula C_nH_m, two theoretical quantities have to be determined:

$$l_{min,m,dry} = \frac{n + \frac{m}{4}}{X_{O_2}}. \tag{3.9}$$

$l_{min,m,dry}$ (in $kmol_{air}/kmol_{fuel}$) is the minimum value of air necessary for a stoichiometric combustion process.

$$v_{min,dry} = n + \left(n + \frac{m}{4}\right) \cdot \left(\frac{1}{X_{O_2}} - 1\right) + X_{N_2,fuel} + X_{CO_2,fuel}. \tag{3.10}$$

$v_{min,dry}$ (in $kmol_{fluegas}/kmol_{fuel}$) represents the minimum amount of dry flue gas that originates from such a reaction. $X_{N_2,fuel}$ and $X_{CO_2,fuel}$ denote the nitrogen and carbon dioxide content in the fuel.

$$\lambda = 1 + \frac{X_{O_2,mea,dry}}{X_{O_2} - X_{O_2,mea,dry}} \cdot \frac{v_{min,dry}}{l_{min,m,dry}}. \tag{3.11}$$

X_{O_2} represents the oxygen content of the dry oxidator. In the present work, X_{O_2} equals to the oxygen content of pure air. $X_{O_2,mea,dry}$ denotes the measured dry oxygen content downstream of the swirl flame or the flame in the second stage, respectively. The air excess ratio λ can be computed as shown in Eqn. 3.11. In the experiments, the air excess ratio is adjusted by varying the fuel mass flow while keeping the air mass flow constant. For the premixed sequential combustor this means that only the fuel mass flow in the second combustion stage is changed while the air flow and the fuel flow through the vitiator are kept constant.

3.3.3 Spectrally Resolved Chemiluminescence Measurements

For the spectrally resolved, line of sight integrated chemiluminescence measurements, a SpektraPro 275 spectrometer from Acton Research Cooperation is used. The focal length is 275 mm with an aperture ratio of 1:3.8. The grating used in this study has 150 grooves per millimeter, allowing the observation of approximately

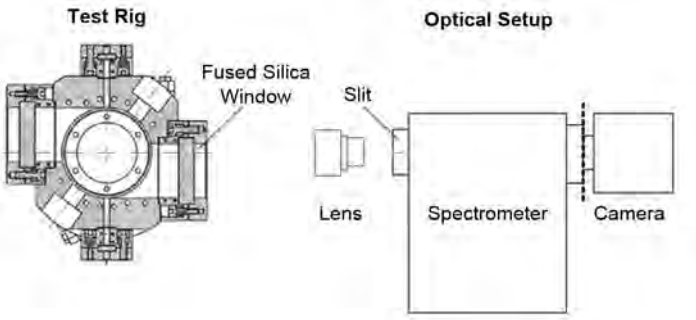

Figure 3.8: Optical setup for the spectrally resolved measurement technique.

300 nm of the flame spectrum with the attached camera. The slit width is adjusted to 10 μm. With a silica lens the image is focused on the slit of the spectrograph. A StreakStar S image intensified camera system from LaVision is used to record the spectrally resolved chemiluminescence images at the optical exit of the spectrometer. The setup is shown in Fig. 3.8. For each measurement 10 to 20 images are recorded at a frame rate of 1Hz and an exposure time of 500 μs. The images are averaged and analyzed with Matlab.

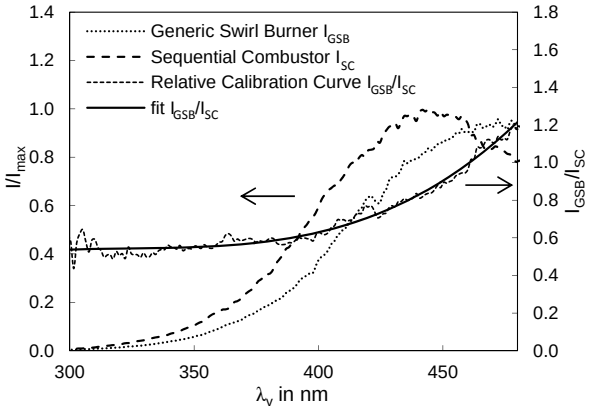

Figure 3.9: Relative intensities of the tungsten lamp as a function of wavelength measured in two different experimental setups. Values are normalized by their maximum values. The relative calibration curve is the ratio between the relative intensities.

An absolute calibration of the optical path with a calibrated tungsten lamp is not possible as the light intensity of the tungsten lamp is too low in the wavelength range around 300 nm. Lauer and Sattelmayer [LS10] were able to do an absolute calibration, but in their study there were thin or no windows in the optical path.

In this study, only a relative calibration is done when the experimental setup is changed so that measurement data from different setups can be compared. A relative calibration is sufficient, because in this work ratios of OH* and CH* are investigated only. In Fig. 3.9, the spectra observed using the tungsten lamp in the generic burner setup (dotted line) and the sequential combustor setup (dashed line) are shown. While the shape of the curves is the same, the relative intensities of the sequential combustor setup are higher. The main reason for that lies in the use of a lens with a lower aperture in case of the sequential combustor setup. The third curve gives the ratio between the spectra of the two measurement setups.

For further analysis of the OH* and CH* chemiluminescence intensities, the measured spectra of the sequential combustion experiment are multiplied by the fitted curve plotted in Fig. 3.9.

Furthermore, the spectral image of a mercury lamp is recorded to obtain the linear relation between pixel and wavelength ([LS10]).

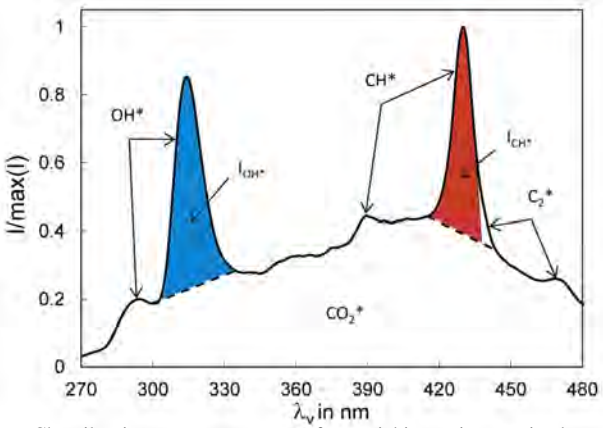

Figure 3.10: Chemiluminescence spectrum of a stoichiometric premixed natural gas/air flame. The narrowband radical emissions from OH*, CH* and C_2* are superimposed by the broadband emission from CO_2*. The intensity is normalized by the maximum value.

The typical spectrum obtained from a premixed natural gas/air flame is shown in Fig. 3.10. The first large peak around 310 nm represents the $X^2\Pi_i \leftarrow A^2\Sigma\ (\Delta v = 0)$ OH* transition. The $X^2\Pi \leftarrow A^2\Delta\ (\Delta v = 0)$ CH* transition emits light around 431 nm [LS10]. Both peaks are superimposed by the broadband CO_2* emissions. The OH* and CH* intensities are calculated by evaluating the areas under the peaks. The section of the amount of CO_2* under each peak has to be subtracted. For that purpose the CO_2* values are interpolated linearly in the region of the peaks.

3.3.4 Three-Lens Technique

A drawback of spectrally resolved images is that one dimension of the image is lost. Lauer and Sattelmayer show in [LS10] how to measure OH* or CH* intensities with bandpass filters. The problem of OH* or CH* bandpass filtered images is that the recorded signal is always the superimposed signal of the species OH* and CO_2* or CH* and CO_2*, respectively. In order to be able to calculate the intensities of OH* or CH*, an additional image has to be taken with a bandpass filter that has a transmittance in a wavelength range where only CO_2* chemiluminescence is emitted from the flame. Therefore it is necessary to take simultaneous images with bandpass filters in the wavelength range of OH* and CO_2* or CH* and CO_2*, respectively. The intensities can be calculated as follows [LS10]:

$$\begin{aligned} S_{BP,310nm|431nm} &= \int_0^\infty ((C_{OH^*|CH^*} \cdot F_{OH^*|CH^*}(\lambda_v) + \\ &\quad + C_{CO_2^*} \cdot F_{CO_2^*}(\lambda_v)) \cdot \hat{T}_{OH^*|CH^*}(\lambda_v)) d\lambda_v, \qquad (3.12) \\ S_{BP,456nm} &= \int_0^\infty \left(C_{CO_2^*} \cdot F_{CO_2^*}(\lambda_v) \cdot \hat{T}_{CO_2^*}(\lambda_v)\right) d\lambda_v, \qquad (3.13) \\ I_{OH^*|CH^*} &= \int_0^\infty \left(C_{OH^*|CH^*} \cdot F_{OH^*|CH^*}(\lambda_v)\right) d\lambda_v. \qquad (3.14) \end{aligned}$$

Herein S_{BP} represents the bandpass filtered signal and $\hat{T}$ the transmittance of the bandpass filters that are provided by the manufacturer. The subscripted vertical line "|" stands for "or". $F(\lambda_v)$ denotes the approximation of the different species with self-similar functions that are obtained from the spectrometer measurements. The proportionality factors C have to be calculated. With Eqn. 3.12 and 3.13, C_{OH^*} or C_{CH^*} can be determined. The corrected intensity can be calculated from Eqn. 3.14.

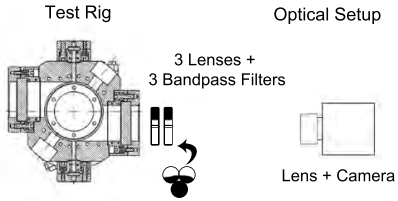

(a) Sketch of the optical setup.

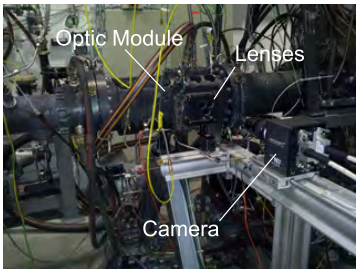

(b) Image of the optical setup.

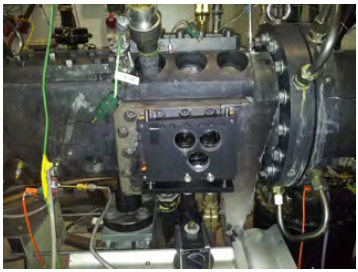

(c) Lens setup without filters.

Figure 3.11: Measurement setup for the three-lens method.

In this thesis the focus lied on the OH*/CH* ratio, hence images of the wavelength ranges of OH*, CH* and CO_2* need to be taken simultaneously. As the optical access to the test rig is limited, it is impossible to use three cameras simultaneously. Therefore three concave lenses with a focal length of f=−50 mm and a diameter of 40 mm are used to triple the original image (see Fig. 3.11). On each lens, a bandpass filter is applied. The following filters are used:

- For the chemiluminescence measurement in the wavelength range of OH* an interference filter with a maximum transmission of 15.01 % at 309.764 nm and a full width at half maximum (FWHM) of 9.064 nm is used.
- For the chemiluminescence measurement in the wavelength range of CO_2*, an interference filter with a maximum transmission of 68.29 % at 456.27 nm and an FWHM of 2.4 nm is used. In this wavelength range, only CO_2* is emitting chemiluminescence.

- For the chemiluminescence measurement in the wavelength range of CH*, an interference filter with a maximum transmission of 48.63 % at 431.39 nm and an FWHM of 10.6 nm is used.

  As the strength of the CH* signal is almost twice the intensity of the other two, a neutral density filter is applied too in order to get a comparable signal strength for all three images.

The images are recorded with a Fastcam APX II high speed camera from Photron. The frame rate is set to 125 frames per second for the premixed flame to record a mean image. The non-premixed flame is recorded at a frame rate of 1000 frames per second to detect single ignition events. A silica lens with a focal length of 45 mm and an aperture of 1:1.8 is used. For each measurement, 500 images are captured and analyzed.

The three resulting images are distorted (see Fig. 3.12 A). An algorithm of Bailey [Bai02] is applied to the images to correct the radial distortion. For the correction of the perspective distortion the Matlab image toolbox is used.

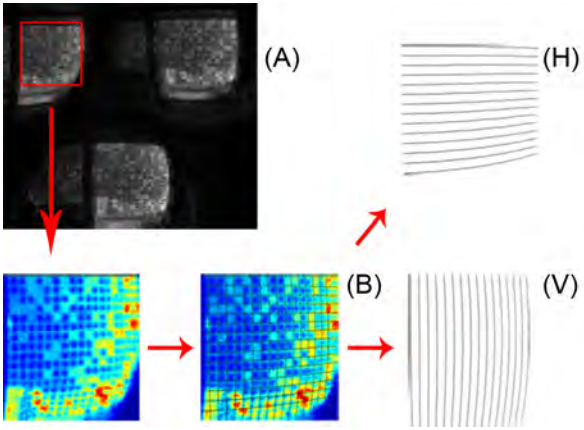

Figure 3.12: (A) shows a tripled image of a pattern on the central image plane. For the distortion correction a grid is drawn onto the pattern (B). Horizontal (H) and vertical (V) lines of the grid are treated separately.

The main features of the distortion correction are explained on the basis of the upper left image. A reference image of a pattern (see Fig. 3.13) put in the central

plane of the fused silica pipe is captured. Then a grid is drawn onto the pattern. The grid is split into two images: the vertical lines (Fig. 3.12 V) and the horizontal lines (Fig. 3.12 H).

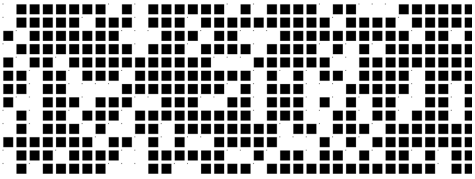

Figure 3.13: Pattern used for the reference image necessary for the correction of distortion.

Using Matlab, a parabola is fitted to every line of Figures 3.12 V and 3.12 H that is detected. The grid lines are hence represented by a polynomial of degree two. For the horizontal lines as follows:

$$\psi = \breve{A}_h \gamma^2 + \breve{B}_h \gamma + \breve{C}_h, \tag{3.15}$$

and for the vertical lines

$$\gamma = \breve{A}_v \psi^2 + \breve{B}_v \psi + \breve{C}_v. \tag{3.16}$$

"h" and "v" are the grid-line indices. According to Bailey, vertical and horizontal grid-lines that have the same distance from the origin of the radial distortion have the same curvature. Any difference in curvature can be attributed to the aspect ratio of the pixels [Bai02]. Even with nominally square pixels aspect ratio distortion can be present [Bai95], which needs to be removed before correcting for radial distortion. An approximation for the aspect ratio is:

$$AR = \sqrt{s_v / s_h}. \tag{3.17}$$

Herein s_h is the slope of $\breve{A}_h$ vs $\breve{C}_h$ for the horizontal lines and s_v the slope of $\breve{A}_v$ vs. $\breve{C}_v$ for the vertical lines. Then the coefficients are scaled according to Tab. 3.1.

Scaling of horizontal lines	Scaling of vertical lines
$\check{A}_h = \check{A}_h \cdot AR^2$	$\check{A}_v = \check{A}_v / AR$
$\check{B}_h = \check{B}_h \cdot AR$	$\check{B}_v = \check{B}_v / AR$
$\check{C}_h = \check{C}_h$	$\check{C}_v = \check{C}_v / AR$

Table 3.1: Scaling of the coefficients for correction of the aspect ratio distortion.

When the lines are corrected for aspect ratio distortion, the radial distortion can be eliminated. Bailey shows that the curvature of each line can be determined by the following expression:

$$\kappa_{h,v} = \frac{-\check{A}_{h,v}}{\check{C}_{h,v}(3\check{A}_{h,v}\check{C}_{h,v} + 3\check{B}_{h,v}^2 + 1)}. \tag{3.18}$$

A single value of κ is obtained by calculating a mean value of all κ weighted by the $\check{C}$ values. A correlation between undistorted image and distorted image is given according to Bailey by the distortion model:

$$\psi_u = \psi_d(1 + \kappa(\gamma_d^2 + \psi_d^2)), \tag{3.19}$$

$$\gamma_u = \gamma_d(1 + \kappa(\psi_d^2 + \gamma_d^2)). \tag{3.20}$$

The index "u" denotes undistorted and "d" distorted values. With Eqns. 3.19 and 3.20 for every pixel in the distorted image the new position in the undistorted image can be calculated. Pixel values are interpolated in the undistorted image from the neighboring pixels in the distorted image. Finally, perspective distortion is corrected with the imtransform-tool of the image toolbox of Matlab. The resulting image (see Fig. 3.14) can be processed further.

Another correction that needs to be done is the correction of relative displacement of the resulting image.

Figure 3.15 shows the graphical reconstruction for the two upper lenses of the three-lens configuration. The axis of the right lens is in line with the center of the object. Therefore a shift of the object in line of sight direction does not change the center position of the virtual image. In case of the left lens the shift in line of

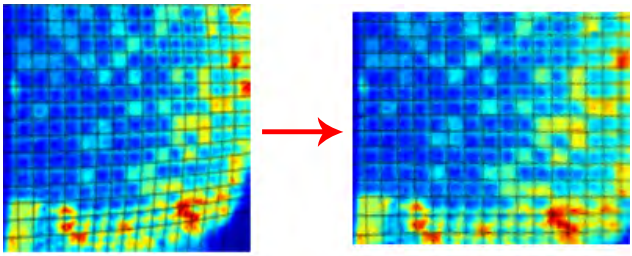

Figure 3.14: Left image: distorted, right image: corrected for aspect ratio, distortion and perspective.

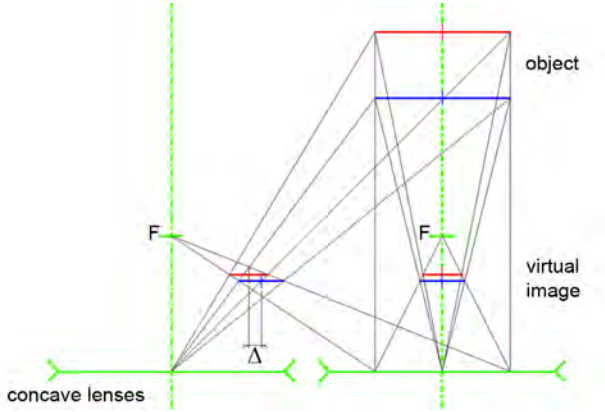

Figure 3.15: Graphical reconstruction for two concave lenses. A shift in line of sight direction of the object leads to a horizontal shift of the left virtual image.

sight direction of the object leads to a shift of the center of the virtual image in horizontal direction (Δ).

Depending on the position in line of sight direction of the object that is recorded, the image sections need to be shifted relative to each other. To get the parameters for the relative displacement, reference images are taken of a pattern positioned 32 mm behind and 32 mm in front of the center plane. Displacement parameters for planes that have an offset of ± 16 mm to the center plane are found by linear interpolation.

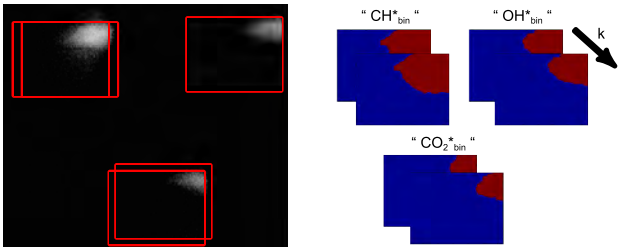

Figure 3.16: Left: original image with borders that imply the image sections. Right: two sets of images of binary type of the flame.

For every triple image of a flame it is necessary to decide, what displacement parameters fit best. Therefore, the three image sections are converted to images of binary type. Meaning that pixels that display intensity values beyond a threshold value are set to one (see Fig. 3.16, right), all others to zero. Then the sum of all absolute differences is determined according to Eqn. 3.21 for all sets (index “k”) of displacement parameters. The more the images differ from each other, the larger the values Eqn. 3.21 returns will be. Therefore, the k^{th} set with the lowest sum of absolute differences is the set where the three images show the most similar flame shape. This set of displacement parameters is used further.

$$\min\left(\sum_{x=1}^{imgsize(x)}\sum_{y=1}^{imgsize(y)} \begin{aligned} &|CH^*_{bin,k}(x,y) - OH^*_{bin,k}(x,y)| + \\ &|CH^*_{bin,k}(x,y) - CO^*_{2\ bin,k}(x,y)| + \\ &|OH^*_{bin,k}(x,y) - CO^*_{2\ bin,k}(x,y)| \end{aligned}\right). \tag{3.21}$$

After the correction of distortion and the selection of the best fitting image sections, the proportionality factors $C_{CO_2^*}$, C_{CH^*} and C_{OH^*} are determined for each pixel. Then the intensity images of OH* and CH* can be calculated. By dividing the OH* by the CH* intensity image pixel by pixel, an image of the OH*/CH* distribution can be found. In case of the reference experiment (the premixed auto-igniting flame) the mean of the OH*/CH* image is used for further analysis. In case of the

non-premixed flame, frequency distributions of the OH*/CH* signal are generated for three areas in the flow field. Each area has a size of 17×17 pixels. The area is chosen that large to obtain enough samples for the measurement of individual distributions. The OH*/CH* distributions have 101 bins and values from 0.1 to 10 are counted.

3.3.5 Temperature Measurements

To be able to compare the simulated temperature of the main flow with reality, temperature profiles are measured with a two-thermocouple temperature probe based on the probe used in the work of Eckstein [EFHS06]. The two thermocouples of type S (PtRh – Pt) have different diameters and allow for correction of measurement errors due to radiative heat losses.

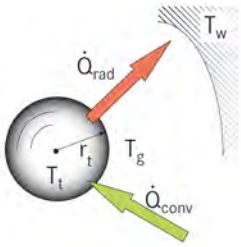

Figure 3.17: Convective and radiative heat flows at the thermocouple tip [Eck05].

For both thermocouples, the stationary energy balances considering convection and radiation can be expressed as follows (see also Fig. 3.17):

$$0 = \alpha_{t,1}(T_g - T_{t,1}) - \check{\varepsilon}_1 \sigma (T_{t,1}^4 - T_w^4), \tag{3.22}$$

$$0 = \alpha_{t,2}(T_g - T_{t,2}) - \check{\varepsilon}_2 \sigma (T_{t,2}^4 - T_w^4). \tag{3.23}$$

Radiative heat losses are approximated by Kirchhoff's law of radiation, assuming that the surface area of the colder combustor walls (index "w") is by far larger than the area of the thermocouples (index "t"). The emissivity $\check{\varepsilon}$ only depends on the material temperature, hence the temperature of the thermocouple. Eckstein

proposes a correlation of Kohler [Koh88] for calculating the emissivity of platinum in hot environment:

$$\check{\varepsilon} = 11 \cdot 10^{-5} T_t + 17 \cdot 10^{-3}, \quad 1000\,\mathrm{K} < T_t < 2000\,\mathrm{K}. \tag{3.24}$$

The different diameters of the thermocouples change the ratio of convection and radiation and therefore different temperatures are measured. The two variables in Eqns. 3.22 and 3.23 are the gas temperature (index "g") and the wall temperature. In contrast to Eckstein's work, here the wall temperature seen by the thermocouples cannot be measured, because parts of the test rig walls are water cooled and parts are uncooled. Therefore Eqns. 3.22 and 3.23 are solved for T_g:

$$T_g = \frac{\sigma \check{\varepsilon}_2 \left(T_{t,2}^4 - T_{t,1}^4 \right) + \alpha_2 T_{t,2} - \frac{\alpha_1 \check{\varepsilon}_2}{\check{\varepsilon}_1} T_{t,1}}{\alpha_2 - \frac{\alpha_1 \check{\varepsilon}_2}{\check{\varepsilon}_1}}. \tag{3.25}$$

A Nusselt-correlation of Whitaker [ID96] is used to calculate the heat transfer coefficient:

$$Nu = 2 + (0.4 Re^{\frac{1}{2}} + 0.06 Re^{\frac{2}{3}}) Pr^{0.4} \left(\frac{\eta}{\eta_w} \right)^{\frac{1}{4}}. \tag{3.26}$$

The gas temperature is found in an iterative calculation process: Reynolds number, Prandtl number and viscosity are calculated on the basis of an estimated gas temperature. η_w is the viscosity of the fluid at wall temperature conditions. The theoretic wall temperature can be determined with Eqn. 3.27.

$$T_w = \sqrt[4]{T_{t,1}^4 - \frac{\alpha_1}{\sigma \check{\varepsilon}_1} (T_g - T_{t,1})}. \tag{3.27}$$

Then Eqn. 3.25 is solved. For the next iteration step the estimated temperature is set to the calculated gas temperature if the difference between both exceeds five Kelvin, otherwise the iteration is stopped.

Data acquisition is done with an Agilent 34970A switch unit that can do up to 440 single channel readings per second [AT12]. In this study, for every measurement point, 200 values with a frequency of 3 Hz are recorded for each thermocouple. With every pair of values the gas temperature is calculated, then the arithmetic mean is determined.

4 Numerical Investigations

In order to get a better understanding of the effects observed through measurements such as the influence of momentum flux ratio on lift-off height (see section 5.1.3.2), the experiments are numerically simulated. An unsteady flamelet model by Pitsch [Pit00] is used to simulate combustion in a post-processing step. In the next section the implementation of the flamelet equations and the simulation procedure are shown. At the end of the chapter, a reactor model is presented that is used in section 5.2 to obtain more insight into the effects of a vitiated co-flow and pressure on chemiluminescence emissions.

4.1 Combustion Simulation

In Fig. 4.1, a chart of the combustion simulation procedure is shown. In this work the main focus lies on the position of ignition events – the lift off height. As the influence of the chemical pre-ignition reactions on the flow field is considered negligible, flow field and ignition are simulated in separated steps.

In the following, the steps involved in the combustion simulation procedure are explained in more detail: Time mean temperature and flow fields are determined with 3D RANS simulations employing the Realizable k-ε turbulence model. In section 4.1.1 details of the flow simulation are presented.

The following data is necessary as input data for the flamelet model: Temperature of the main flow, velocity, mixture fraction, turbulent kinetic energy and turbulent dissipation rate are read from RANS simulation data. The scalar dissipation rate is calculated according to Eqn. 2.22 from the turbulent kinetic energy, the turbulent dissipation rate and the variance. The latter originates from measured water channel data. Furthermore, mixture PDFs are determined from variance and mixture fraction (see section A.2).

Using the flamelet model allows to simulate combustion of non- or partially premixed fuel/air mixtures. Furthermore it is a model with two partial differential equations that can easily be transformed to a system of initial value problems. To solve such systems, only low computational power is necessary. Therefore it

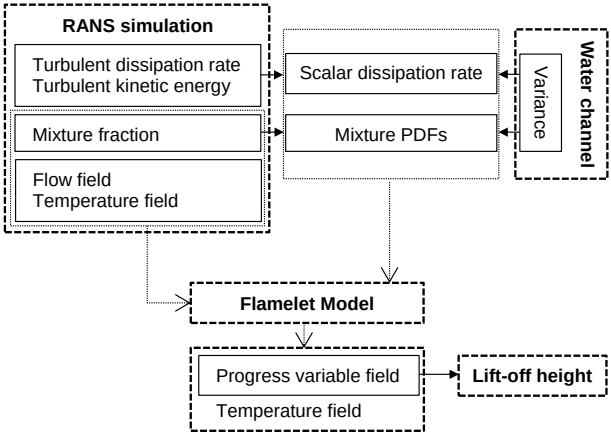

Figure 4.1: Chart of the combustion simulation procedure.

is used in this study, as a low cost model suitable for non- or partially premixed combustion systems is needed.

The flamelet model's implementation is presented in detail in section 4.1.2.2. With the output data of the flamelet model the lift-off height can be determined.

4.1.1 Simulation of the Temperature and Flow Field

Only the combustor with the central lance and the case "without area expansion" is evaluated numerically as recirculation zones that occur at area expansions are not reproduced well by RANS simulations [CLYS03, Ter04]. In order to reduce the simulation cost, only the section downstream of the vitiator is simulated. One of the key parameters in the simulations is the fuel mass flow through the central lance. The co-flow upstream of the end of the lance is not influenced by the fuel mass flow, therefore the simulated domain is split into two parts (see also Fig. 3.5). The first section (see Fig. 4.2) stretches from the beginning of the high temperature insulated part to the end of the flow homogenizer, which is treated in the simulation as a 30 mm long porous zone.

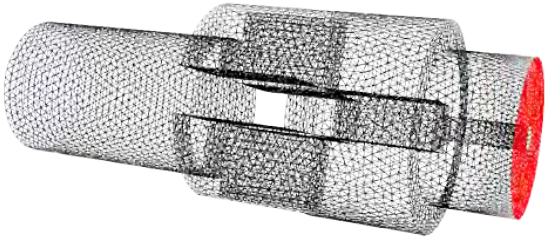

Figure 4.2: First simulation section. Meshed with tetrahedron cells. Flow from left to right.

The second section (see Fig. 4.3) begins at the outlet of the flow homogenizer and ends 320 mm after the injector outlet. For the simulation of the flow in the second section the outlet data of the first section (only axial velocity and temperature) is patched onto the inlet plane. Fluent is used for simulating the temperature and flow field and Gambit for meshing. In the first simulation section a tetrahedron mesh with 96 000 cells is applied. The flow homogenizer is meshed with a finer mesh to produce high resolution inlet data for the second simulation section. Here a structured mesh with 124 000 hexahedral cells leads to the best agreement between experimentally and numerically obtained results regarding the mixture fraction of the fuel jet.

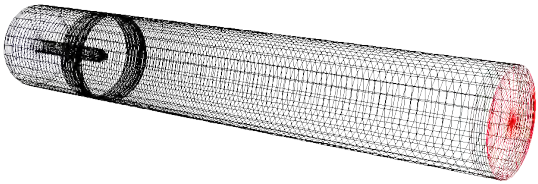

Figure 4.3: Second simulation section. Meshed with hexahedral cells [KB10]. Flow from left to right.

For the convective boundary conditions, heat transfer coefficients are calculated with analytical Nusselt correlations prior to all simulations. The inlet temperature is determined via an analytical thermal model of the vitiator (see section 3.1.3). Boundary conditions for simulations at 1 and 6 bar are presented in Tab. 4.1.

T_{ref} is the temperature of the surface corresponding with the heat transfer coefficients. The thickness of the lance insulation varies, therefore a range is given for

Boundary	Type of boundary	1^{st} section Values at 1 bar	Values at 6 bar
Inlet	Mass flow ($\dot{m}$, T, TI)	0.02 kg/s, 1498 K, 10 %	0.117 kg/s, 1305 K, 10 %
Outer walls	Convection (α, T_{ref})	7 W/(m^{2}K), 350 K	7.5 W/(m^{2}K), 350 K
Insulated parts of lance	Convection (α, T_{ref})	12…36 W/(m^{2}K), 290 K	10…40 W/(m^{2}K), 290 K
Parts of lance at flow homogenizer without insulation (laminar flow)	Convection (α, T_{ref})	730 W/(m^{2}K), 290 K	690 W/(m^{2}K), 290 K
Boundary	Type of boundary	2^{nd} section Values at 1 bar	Values at 6 bar
Inlet	Velocity inlet (u_∞, T, TI)	from outlet 1^{st} sec., 5 %	from outlet 1^{st} sec., 5%
Fuel inlet lance	Velocity inlet (u_0, T, TI)	74…167 m/s, 300 K, 5 %	67…151 m/s, 300 K, 5 %
Wall of the lance	Convection (α, T_{ref})	103 W/(m^{2}K), 290 K	302 W/(m^{2}K), 290 K
Outer wall	Convection (α, T_{ref})	55 W/(m^{2}K), 350 K	65 W/(m^{2}K), 350 K

Table 4.1: Boundary conditions of 1^{st} and 2^{nd} section at 1 bar and 6 bar.

those heat transfer coefficients. As the second simulation section is downstream of the flow homogenizer, the turbulence intensity is lower than in the first simulation section.

The measured and simulated mixture fractions on the centerline are compared with each other in Fig. 4.4a. As jet and main flow have the same density in the isothermal measurement, the experimental data needs to be corrected by the effective diameter[1] $d_{eff} = d\sqrt{\rho_0/\rho_\infty}$ according to Thring and Newby [TN53]. Compared to the data from the water channel measurements, the experimental data shows slightly lower fuel mass fractions in the far field ($x_1/d > 30$). In the near field simulation and experiment agree very well.

Looking at comparisons in radial direction, Fig. 4.4b shows that the simulated mixture fraction lies a bit above the measured one, but both agree well in width and shape.

Measured temperature profiles are compared to simulated data in Fig. 4.5. Due to the limited access to the test rig, only three temperature profiles can be measured.

1 Here the water channel data is stretched.

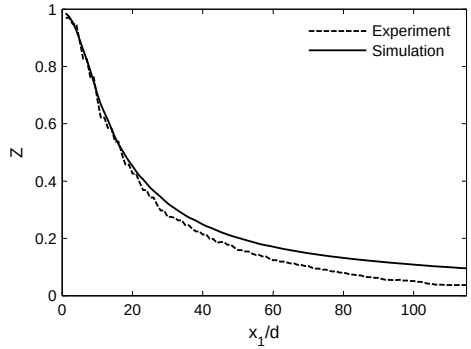

(a) Mixture fraction on the center line.

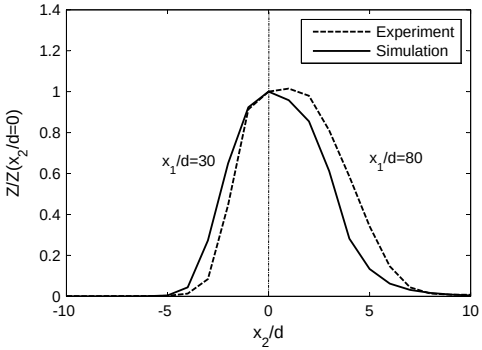

(b) Normalized mixture fraction in radial direction.

Figure 4.4: Comparison of water channel measurement and RANS simulation – mixture fractions on the center line (a) and normalized mixture fraction in radial direction at $x_1/d = 30$ and $x_1/d = 80$ (b) for a momentum flux ratio of $J = 100$ and a Reynolds number of $\approx 47\,000$ in the main flow.

Furthermore the inner fused silica tube has to be removed to measure along the traverses shown in Fig. 4.5a.

Temperature measurements are checked against simulated values in Fig. 4.5b – d. Discrepancies are in the range of 7 % which is acceptable as the uncertainty of

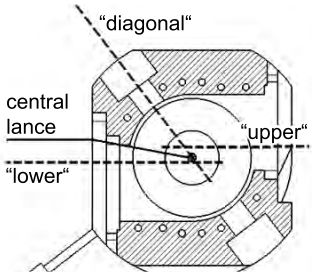

(a) Section drawing of test rig. The dashed lines indicate the measure traverses that are 80 mm ("diagonal") and 115 mm ("upper" and "lower") downstream the injector nozzle.

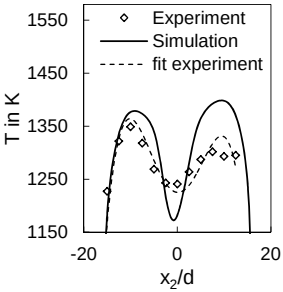

(b) Diagonal traverse.

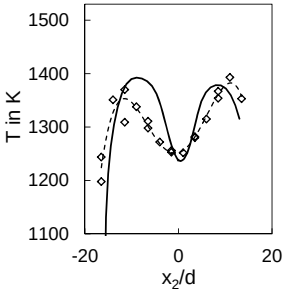

(c) Lower traverse.

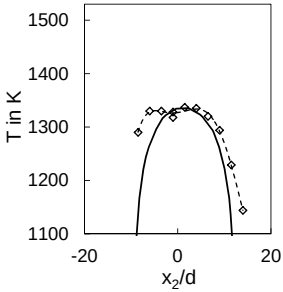

(d) Upper traverse.

Figure 4.5: Position of measurement traverses (a). Comparison of experiment and RANS simulation – three temperature profiles of the main flow at 1 bar (b – d).

the measurement method is already in the range of 4 %. Furthermore, the shape of the curves can be reproduced in the simulation. The diagonal traverse shows that temperature decreases in the center of the pipe due to the water cooled fuel lance. The effect is slightly overestimated in the simulation. Comparing Fig. 4.5c and 4.5d, it can be seen that only the lower traverse shows a local minimum at the temperature profile's center. This is caused by the lower traverse being located closer to the water cooled lance (see also Fig. 4.5a).

As simulated mixture and temperature are comparable to the experimental results, it is assumed that the simulated data is suitable as basis for post-processed auto-ignition simulations.

4.1.2 Implementation of the Flamelet Model

The domain for the combustion simulation stretches from the nozzle outlet to 115 nozzle-diameters downstream and over the whole pipe diameter. It is divided into cells in axial (115), vertical (33) and horizontal (33) direction (x_1, x_2, x_3; x_1 is the axial and therefore the flow direction). Each cell is a cube with the side length of one nozzle diameter. Figure 4.6 shows the simulation domain.

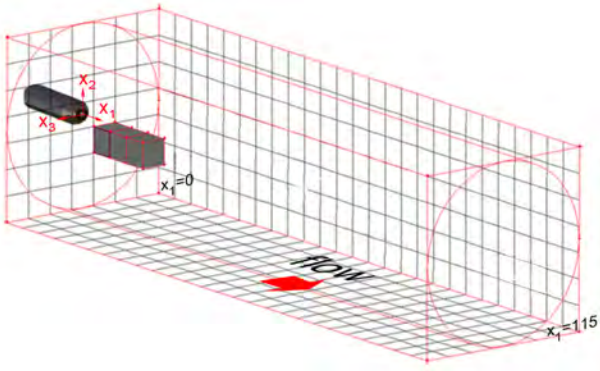

Figure 4.6: Sketch of the simulation domain: the grey boxes represent the cells the domain is divided in ($33 \times 33 \times 115$).

In each cell the process shown in Fig. 4.7 is executed. Flamelet information of the previous cells and data from the RANS simulation (scalar dissipation rate, temperature and velocity) are loaded into the solver of the flamelet equations.

Therein the flamelet equations presented in section 2.3.2 (Eqns. 2.17 and 2.18) are solved if the mean mixture fraction is above 0.002 [2]. To reduce computational costs, tabulated chemistry in combination with a composite progress variable is applied. The output are the progress variable Y_c and the temperature T as a function

2 No reliable data for the variances is available below this value

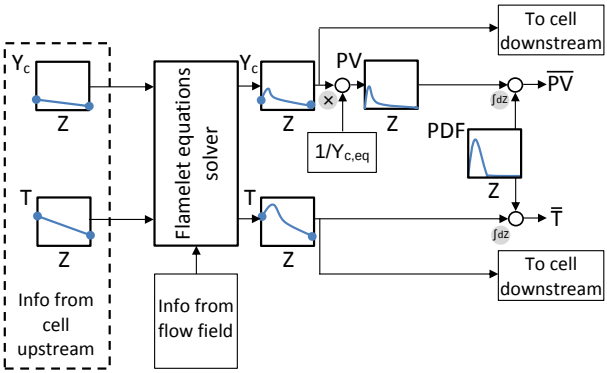

Figure 4.7: Sketch of the steps processed in each cell.

of mixture fraction Z. The progress variable is divided by the equilibrium value, therefore a normalized progress variable PV is obtained. With the mixture fraction PDF, mean values of the normalized progress variable and the temperature are calculated. The mean normalized progress variable $\overline{PV}$ is used as indicator for ignition.

In the following, the steps shown in Fig. 4.7 are explained in detail.

4.1.2.1 Convection of Flamelets

At $x_1 = 0$ in all 33×33 cells the flamelets are initialized with data from the RANS simulation. The boundary conditions $Y_c(Z = 1) = 0$, $Y_c(Z = 0) = Y_{c,in_2}$, $T(Z = 1) = T_{fuel}$ and $T(Z = 0) = T_\infty(0, x_2, x_3)$ are set.

Compared to the axial velocity in x_1-direction, the velocities in x_2 and x_3 direction are negligibly small. Therefore the convection of the flamelets with the flow is considered in axial direction only. The residence time of the flamelets in the cells is computed from the flow velocity in x_1-direction and the length of one cell (= 1 nozzle-diameter): $\Delta t = d/u$.

From $x_1 = 1$ up to $x_1 = 115$ the output of each cell upstream is the input for the next cell downstream. Additionally, the temperature at the boundary $Z = 0$ is set to the temperature of the main flow $T(Z = 0) = T_\infty(x_1, x_2, x_3)$.

4.1.2.2 Flamelet Equations Solver

In the following, the implementation of the flamelet equations in Matlab is explained. Matlab is used for the combustion simulation for several reasons: it can use Cantera methods, has powerful tools to solve differential equations and measurement data can be easily linked to it.

The flamelet equations are linear second-order partial differential equations of parabolic type [BSMM01]. They are solved using a finite difference approximation in mixture fraction space and the ode23 function of Matlab in time. The latter is a function for solving differential equations with the Bogacki-Shampine-method [BS89].

$$\begin{aligned}\left.\frac{\partial^2\Phi}{\partial Z^2}\right|_{Z_e} &\approx \frac{\frac{\Phi_{e+1}-\Phi_e}{Z_{e+1}-Z_e}-\frac{\Phi_e-\Phi_{e-1}}{Z_e-Z_{e-1}}}{\frac{1}{2}[(Z_{e+1}-Z_e)+(Z_e-Z_{e-1})]} \\ &= \frac{2}{\Delta Z_{e-1}+\Delta Z_e}\left(\frac{\Phi_{e+1}-\Phi_e}{\Delta Z_e}-\frac{\Phi_e-\Phi_{e-1}}{\Delta Z_{e-1}}\right). \qquad (4.1)\end{aligned}$$

By applying the finite difference scheme to the differential equations Eqn. 2.17, Eqn. 2.18 and using Eqn. 2.19, the flamelet equations become a system of initial value problems:

$$\frac{\partial Y_i}{\partial t}(Z_e,t) = \frac{\chi}{\Delta Z_{e-1}+\Delta Z_e}\left(\frac{Y_{i,e+1}-Y_{i,e}}{\Delta Z_e}-\frac{Y_{i,e}-Y_{i,e-1}}{\Delta Z_{e-1}}\right)+\frac{\dot{w}_i}{\rho}, \qquad (4.2)$$

$$\begin{aligned}\frac{\partial T}{\partial t}(Z_e,t) &= \frac{\chi}{\Delta Z_{e-1}+\Delta Z_e}\left(\frac{T_{e+1}-T_e}{\Delta Z_e}-\frac{T_e-T_{e-1}}{\Delta Z_{e-1}}\right) \qquad (4.3)\\ &\quad -\sum_{i=1}^{n}\frac{h_i}{\rho c_p}\dot{w}_i.\end{aligned}$$

Y_i denotes the mass fraction of species i, where $0 \le e \le N_e$ is the index of the discrete values in the mixture fraction space, Z the mixture fraction, χ the scalar dissipation rate, ρ the density, c_p the specific heat capacity and T the temperature. $\dot{w}_i$ and $\sum_{i=1}^{n} h_i \dot{w}_i$ are the source terms for the flamelet equations. Unequal intervals are chosen to discretize the Z-domain. As ignition starts at low mixture fractions, a logarithmic step-size progression with 15 intervals is applied, shown in Fig. 4.8.

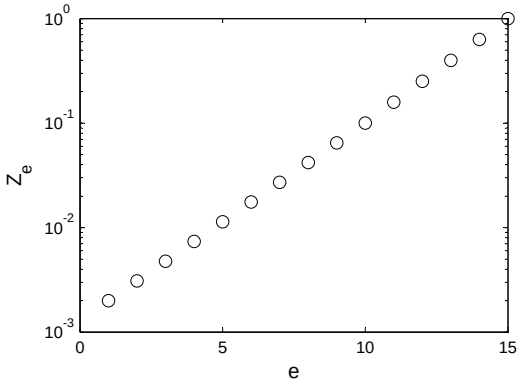

Figure 4.8: Logarithmic step-size progression. Discretized mixture fraction Z_e as a function of step number e.

For a chemical mechanism with 53 species this leads to a system of $16 \times 53 + 16 = 864$ differential equations. To simulate combustion, the flamelet equations have to be solved in every cell of the simulation domain shown in Fig. 4.6. This many differential equations would need too much computational power to be solved within reasonable time. For this reason, a progress variable in combination with tabulated chemistry is used.

Progress Variable and Tabulated Chemistry

Using a progress variable, Eqns. 4.2 and 4.3 can be written as:

$$\frac{\partial Y_c}{\partial t}(Z_e,t) = \frac{\chi}{\Delta Z_{e-1}+\Delta Z_e}\left(\frac{Y_{c,e+1}-Y_{c,e}}{\Delta Z_e}-\frac{Y_{c,e}-Y_{c,e-1}}{\Delta Z_{e-1}}\right)+\frac{\dot{w}_c}{\rho}, \quad (4.4)$$

$$\frac{\partial T}{\partial t}(Z_e,t) = \frac{\chi}{\Delta Z_{e-1}+\Delta Z_e}\left(\frac{T_{e+1}-T_e}{\Delta Z_e}-\frac{T_e-T_{e-1}}{\Delta Z_{e-1}}\right) - \frac{\dot{Q}_c}{\rho c_p}. \quad (4.5)$$

Y_c denotes the progress variable and $\dot{Q}_c$ the source term for the energy equation. $\dot{Q}_c$ is a function of the progress variable. In this work a composite progress variable is applied which is the sum of more than one species' mass fractions (reactants and products). Species need to be chosen in such a way that the progress variable increases monotonously from initial conditions up to equilibrium.

According to Pitsch and Ihme [PI04], the sum of the mass fractions of CO_2, H_2O, CO and H_2 fulfill this requirement. In his PhD thesis, Brandt [Bra05] states that CH_2O would be a good choice for a progress variable to represent the pool of radicals, because its source term has already got high values at low mass fractions. In test calculations, the agreement between calculations with the progress variable in combination with tabulated source terms (Eqns. 4.4 and 4.5) and calculations where the flamelet equations were solved for all species (Eqns. 4.2 and 4.3) could be improved when CH_2O was used for the composite progress variable, too. Therefore the mass fraction of CH_2O is added to the progress variable:

$$Y_c = Y_{H_2} + Y_{H_2O} + Y_{CO} + Y_{CO_2} + Y_{CH_2O}. \tag{4.6}$$

The source terms $\dot{w}_c$ and $\dot{Q}_c$ in Eqns. 4.4 and 4.5 are computed in a preprocessing step, where the flamelet equations (Eqns. 4.2 and 4.3) are solved for all species. Source terms are tabulated as a function of the parameters mixture fraction Z, progress variable Y_c, stoichiometric scalar dissipation rate χ_{st}, temperature of main flow T_∞, air excess ratio of the vitiator, and pressure. In the preprocessing step, the source terms are evaluated with the Cantera methods "netProdRates" and "enthalpies_RT" using the GRI3.0 [SGF$^+$] mechanism. "netProdRates" returns the net chemical production rates of all chemical species, depending on temperature and on the mass fractions of all species. Therefore Cantera calculates the forward and backward rate coefficients for all 325 reaction equations of the GRI3.0 mechanism. For the majority of the equations the modified Arrhenius equation (see Eqn. 2.33) is used. The calculation of rate coefficients for pressure dependent, three-body or falloff reactions is more complex and can be found in [KRM$^+$04]. This will not be discussed here as it is not important for the understanding of this work.

With Eqn. 4.7, the molar reaction rate of creation/destruction of species i in reaction r is computed:

$$\dot{\omega}_{i,r} = \left(\nu_{i,r,2} - \nu_{i,r,1}\right)\left(k_{R,f,r}\prod_{j=1}^{N_r}\left[C_{j,r}\right] - k_{R,b,r}\prod_{j=1}^{N_r}\left[C_{j,r}\right]\right). \tag{4.7}$$

$\nu_{i,r,1}$ is the stoichiometric coefficient for reactant i in reaction r, $\nu_{i,r,2}$ the stoichiometric coefficient for product i in reaction r, N_r denotes the number of chemical species in reaction r and $C_{j,r}$ the molar concentration of each reactant and product species j in reaction r. To obtain the chemical source term of species i for Eqn. 4.3, the sum of $\dot{\omega}_{i,r}$ over the N_R reactions that species i participates in is calculated. The sum is multiplied by the molar mass of species i.

$$\dot{w}_i = M_i \sum_{r=1}^{N_R} \dot{\omega}_{i,r}. \tag{4.8}$$

The "enthalpies_RT" method returns the pure-species standard-state enthalpies divided by the ideal gas constant and the temperature. To obtain the enthalpy of each species that is necessary for the source term in Eqn. 4.3, the standard-state enthalpies are multiplied by the temperature and the ideal gas constant.

Values are tabulated from zero to ten milliseconds for five stoichiometric scalar dissipation rates (0, 1, 5, 10, 20) at five different start temperatures (equivalent to the main flow temperature). The start conditions for the flamelet calculation process depend on the operating conditions of the vitiator. They are calculated with the equilibrate method of Cantera. Only O_2, N_2, CO_2 and H_2O are considered at the inlet of the second combustion stage.

The source terms are selected from the tables, non tabulated values are interpolated linearly. The integration time equals the residence time, which is determined by the flow velocity $\Delta t = d/u$, where d denotes the nozzle-diameter and u the velocity in x_1 direction.

4.1.2.3 Output of Each Calculation Cell

Figure 4.9a shows a flamelet representing the evolution of the progress variable over time. Ignition starts at low mixture fraction values, as the mass fraction of the progress variable increases there first. The base line ($t = 0.5\,\text{ms}$ similar to

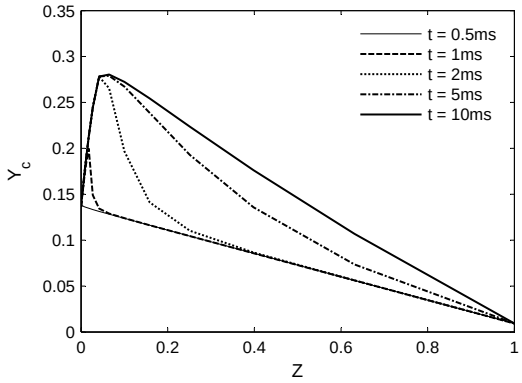

(a) Progress variable

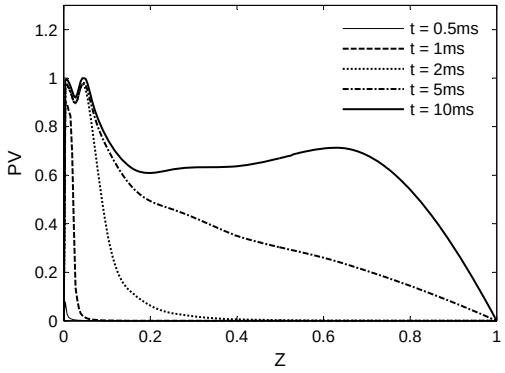

(b) Normalized progress variable

Figure 4.9: Temporal evolution of a flamelet – at 0.5, 1, 2, 5 and 10 ms; $\chi_{st} = 1\,\mathrm{s}^{-1}$; $T_\infty = 1500\,\mathrm{K}$.

$t = 0.0\,\mathrm{ms}$), is at $Z = 0$ non-zero because of the mass fractions of H_2O and CO_2 in the co-flow.

Kulkarni and Polifke [KP12] showed that a normalized progress variable (PV) is a good quantity to be used as the ignition criteria. With the mass fraction of the progress variable it is computed as a function of the mixture fraction:

$$PV(Z) = \frac{Y_c(Z) - Y_{c,in_2}(Z)}{Y_{c,eq}(Z) - Y_{c,in_2}(Z)}, \tag{4.9}$$

wherein the index eq denotes the equilibrium values and in_2 the mass fraction at the inlet of the second combustion stage.

In Fig. 4.9b, the temporal evolution of the normalized progress variable corresponding to the temporal evolution of the progress variable in Fig. 4.9a is plotted. Between the mixture fractions 0.01 and 0.04, the equilibrium value of the progress variable is only reached if the scalar dissipation rate is zero. In the shown calculations, the scalar dissipation rate was set to unity.

With Eqn. 4.9 the normalized progress variable is evaluated as a function of Z. Mean temperature and mean normalized progress variable are determined for each simulation cell from the local PDF and the solution of the flamelet equations with Eqns. 4.10 and 4.11 (see also Fig. 4.6).

$$\overline{T}(\mathbf{x}) = \int_0^1 T(Z,\mathbf{x})P(Z,\mathbf{x})\mathrm{dZ}, \tag{4.10}$$

$$\overline{PV}(\mathbf{x}) = \int_0^1 PV(Z,\mathbf{x})P(Z,\mathbf{x})\mathrm{dZ}. \tag{4.11}$$

$P(Z,\mathbf{x})$ denotes the PDF at position (x_1,x_2,x_3). $T(Z,\mathbf{x})$ and $PV(Z,\mathbf{x})$ are the temperature and normalized progress variable from the solved flamelet equations at position (x_1,x_2,x_3).

Experimentally determined variances of the PDFs are used instead of less precise values from the numerical simulation of the non-reacting flow employing presumed PDF transport equations. According to Pitsch [Pit00] mixture fraction PDFs are well represented by beta distributions. This assumption is confirmed in Fig. 4.10, where a PDF obtained from water channel measurements is reproduced by a beta distribution. Variance (0.000275) and mean value (0.0529) are the same for both distributions.

For the lift-off height, the position $\overline{PV} > 0.5$ is defined. To get the lift-off height, a coordinate transformation into cylindrical coordinates is done—the flow direction

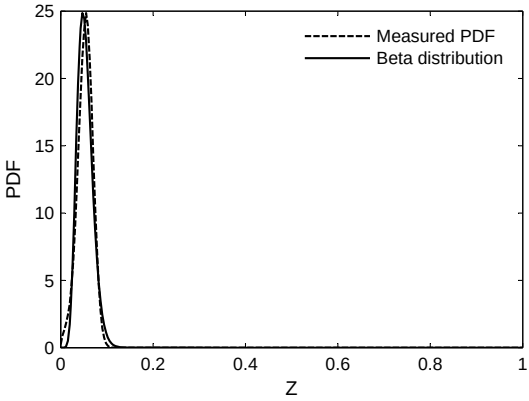

Figure 4.10: Experimentally determined PDF and beta distribution with the same variance (0.000275) and mean value (0.0529).

remains the x_1-direction. Then the flow field is scanned at every angle from the nozzle downstream, searching the first x_1 where $\overline{PV} > 0.5$ is found. The arithmetic mean of all points found is the mean lift-off height. Such a method is necessary as the flow field is asymmetric (see section 5.1.2) in experiment and simulation.

4.2 Numerical Investigation of Chemiluminescence

In order to understand how vitiated flow and pressure affect the chemiluminescence emissions of OH* and CH* radicals, chemiluminescence emissions are calculated in a post-processing step by using species concentrations determined with a reactor model in Cantera. As shown in Fig. 4.12, the chemiluminescence concentrations are below 1×10^{-14}. Therefore the flamelet combustion model presented in the previous section cannot be used, because its precision is too low as interpolation processes are involved in the calculation. Furthermore chemiluminescence emissions of the sequential combustion process are simulated only, because for the swirl flame too many assumptions would be necessary such as preheat temperature, residence time or amount of recirculating mass.

4.2.1 Constant Pressure Batch Reactor

The chemiluminescence reactions are calculated using the batch reactor module of Cantera. It describes a fixed mass homogeneous system which allows to prescribe the system volume as a function of time. The batch reactor is given by the conservation equations of species and energy:

$$\rho V \frac{dY_i}{dt} = \dot{\omega}_i M_i V, \tag{4.12}$$

$$\frac{dU}{dt} = -p\frac{dV}{dt} - \dot{Q}. \tag{4.13}$$

$\dot{\omega}_i$ is the molar reaction rate, M_i the molar mass and Y_i the mass fraction of species i. ρ denotes the density, U the internal energy, V the volume and $\dot{Q}$ the heat flux through the reactor wall.

To simulate constant pressure combustion ($p = p_\infty = \text{const}$), the following equation for the reactor volume is solved:

$$\frac{dV}{dt} - K_w A_w (p - p_\infty) = 0. \tag{4.14}$$

K_w is an expansion factor which determines the pressure response of the reactor volume. A_w denotes the area of the reactor wall that is fixed to $A_w = 1\,\text{m}^2$. K_w needs to be chosen large enough such that the volume response to pressure deviation maintains the pressure constant. However choosing the expansion factor too large, the numerical system becomes very stiff and convergence is hindered. In Fig. 4.11 the maximum pressure during the solution, divided by the mean pressure is plotted as a function of K_w. From this a value of $K_w = 10^4\,\text{m s}^{-1}\,\text{Pa}^{-1}$ can be inferred.

Rewriting Eqn. 4.13 in terms of enthalpy and inserting Eqn. 4.14,

$$\frac{dH}{dt} - p\frac{dV}{dt} = -p\left[K_w A_w (p - p_\infty)\right] - \dot{Q}, \tag{4.15}$$

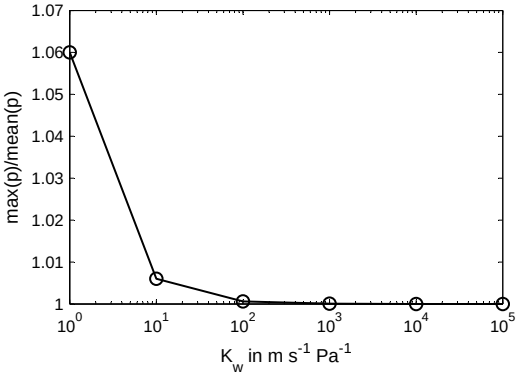

Figure 4.11: Pressure ratio as a function of the expansion factor.

the familiar enthalpy balance for constant pressure is obtained:

$$\frac{dH}{dt} = p \underbrace{\left[\frac{dV}{dt} - K_w A_w (p - p_\infty)\right]}_{\leq 0} - \dot{Q}. \tag{4.16}$$

The advance method of Cantera [Goo12] is used to solve the differential equations Eqns. 4.12 to 4.14.

For modeling the sequential combustor, the composition of the oxidator corresponds to the outlet condition of the vitiator, calculated with the equilibrium method of Cantera. The temperature of the oxidiator, the fuel composition and the ratio of fuel to oxidator are set according to the parameters of the experiments presented in section 5.2.

4.2.2 Simulation of OH* and CH* Chemiluminescence Emissions

The Gri3.0 mechanism is used to provide all concentrations necessary for the chemiluminescence mechanism suggested by Panoutsos et al. [PHT09] (see Tab. 4.2). The equations for the concentrations of OH* and CH* (Eqns. 4.17 and 4.18) can be deduced according to Nori [Nor08] from the chemiluminescence

mechanism (see also section 2.4). The chemiluminescence concentrations are calculated after each time step of the reactor.

	Reaction			A_A	B	E_A	Ref.
1	$CH + O_2$	$\rightarrow$	$OH^* + CO$	$6.00E+10$	0.00	0.00	[PCKB67]
2	$OH^* + N_2$	$\rightarrow$	$OH + N_2$	$1.08E+11$	0.50	−5183.26	[TBH+98]
3	$OH^* + O_2$	$\rightarrow$	$OH + O_2$	$2.10E+12$	0.50	−2018.04	[TBH+98]
4	$OH^* + H_2O$	$\rightarrow$	$OH + H_2O$	$5.92E+12$	0.50	−3605.83	[TBH+98]
5	$OH^* + H_2$	$\rightarrow$	$OH + H_2$	$2.95E+12$	0.50	−1859.94	[TBH+98]
6	$OH^* + CO_2$	$\rightarrow$	$OH + CO_2$	$2.75E+12$	0.50	−4053.82	[TBH+98]
7	$OH^* + CO$	$\rightarrow$	$OH + CO$	$3.23E+12$	0.50	−3295.01	[TBH+98]
8	$OH^* + CH_4$	$\rightarrow$	$OH + CH_4$	$3.36E+12$	0.50	−2659.62	[TBH+98]
9	$C_2H + O$	$\rightarrow$	$CH^* + CO$	$1.08E+13$	0.00	0.00	[DVLCP96]
10	$C_2H + O_2$	$\rightarrow$	$CH^* + CO_2$	$2.17E+10$	0.00	0.00	[DVLCP96]
11	$CH^* + N_2$	$\rightarrow$	$CH + N_2$	$3.03E+02$	3.40	−1595.17	[TBH+98]
12	$CH^* + O_2$	$\rightarrow$	$CH + O_2$	$2.48E+06$	2.14	−7201.30	[TBH+98]
13	$CH^* + H_2O$	$\rightarrow$	$CH + H_2O$	$5.30E+13$	0.00	0.00	[TBH+98]
14	$CH^* + H_2$	$\rightarrow$	$CH + H_2$	$1.47E+14$	0.00	5698.23	[TBH+98]
15	$CH^* + CO_2$	$\rightarrow$	$CH + CO_2$	$2.40E-01$	4.30	−6841.23	[TBH+98]
16	$CH^* + CO$	$\rightarrow$	$CH + CO$	$2.44E+12$	0.50	0.00	[TBH+98]
17	$CH^* + CH_4$	$\rightarrow$	$CH + CH_4$	$1.73E+13$	0.00	699.20	[TBH+98]

Table 4.2: OH* and CH* chemiluminescence mechanism from Panoutsos et al. [PHT09]. $k_R = A_A T^B exp(-E_A/RT)$. E_A [J mol^{-1}], R [J mol^{-1} K^{-1}].

$$[OH^*] = \frac{k_{R,1}[CH][O_2]}{\sum_j k_{R,j}[M_j] + A_{OH^*}}, \tag{4.17}$$

$$[CH^*] = \frac{k_{R,9}[C_2H][O] + k_{R,10}[C_2H][O_2]}{\sum_j k_{R,j}[M_j] + A_{CH^*}}. \tag{4.18}$$

$k_{R,1}$, $k_{R,9}$ and $k_{R,10}$ are the reaction rate coefficients for the suggested formation reactions (Reactions 1, 9 and 10 in Tab. 4.2). $k_{R,j}$ is the quenching rate coefficient for species j, $[M_j]$ is the concentration of species j and A_i the Einstein coefficient for spontaneous emission for the $X^2\Pi_i \leftarrow A^2\Sigma$ ($\Delta v = 0$) OH* transition and the $X^2\Pi \leftarrow A^2\Delta$ ($\Delta v = 0$) CH* transition respectively. Kathrotia et al. [KRS+12] and Tamura et al. [TBH+98] give different values for the Einstein coefficients. In this study the agreement between experimental and numerical results can be improved if the values of Tamura et al. are used: $A_{OH^*} = 1.4 \cdot 10^6\,s^{-1}$ and $A_{CH^*} = 1.85 \cdot 10^6\,s^{-1}$.

Nori states that the volumetric photon emission rate can be determined with the equation:

$$\iota_i = A_i[i^*], \tag{4.19}$$

where A_i is the Einstein coefficient. i can stand for OH* or CH*. As the flame is optically thin, self absorption is neglected. In order to compare the modeled data with experimental data, the spatially integrated chemiluminescence intensity is calculated with Eqn. 4.20.

$$I_i = \int_{L_0}^{L_0+L_t} \iota_i \mathrm{dx}_1. \tag{4.20}$$

The integration length (L_t) is set to the combustor diameter. Integration starts from L_0, the mean of the positions where $\iota_i \geq (\iota_{i,max} \cdot 0.01)$. To get the total chemiluminescence intensity, I_i needs to be multiplied by the flame surface [Nor08]. In this study the focus lies on relative chemiluminescence intensities, therefore knowledge about the flame's surface is not necessary. The chemiluminescence intensity ratio is obtained from the division of I_{OH*} by I_{CH*}.

The reactor model returns all data as a function of time. To obtain data as a function of space, the flow velocity at each time step t_l is calculated with the area of the combustion chamber, the mass flow (sum of oxidator mass flow and fuel mass flow) and the actual density, which is a function of temperature:

$$u_l = \frac{\dot{m}}{A\rho(T_l)}. \tag{4.21}$$

The distance L in axial direction is then obtained from the sum of the velocities at each time step multiplied by the reactor time step over a certain time interval $l \ldots n$:

$$L = \sum_{l}^{n} u_l \cdot \Delta t. \tag{4.22}$$

In Fig. 4.12 a sample output for concentrations of OH*, CH* and the main reactants are plotted as a function of time. Their concentrations are by orders of magnitude lower than the ones of OH, CH or O_2 (O_2 starts at concentrations of

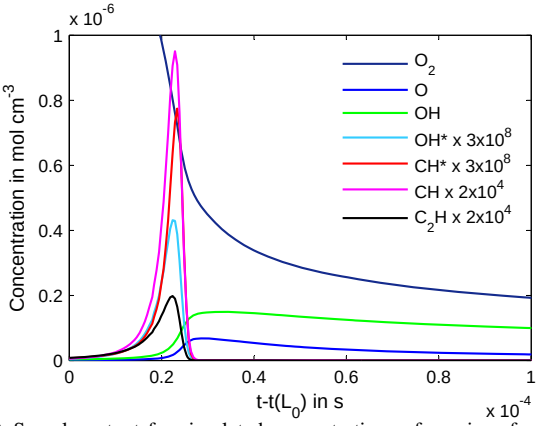

Figure 4.12: Sample output for simulated concentrations of species of reactions 1, 9 and 10 of Tab. 4.2 for the sequential combustor. Inlet temperature $T_{in} = 1205\,\mathrm{K}$, pressure $p = 3\,\mathrm{bar}$, air excess ratio $\lambda = 1.02$.

approx. $4 \times 10^{-6}\,\mathrm{mol\,cm^{-3}}$). Due to the low concentrations of OH* and CH*, Nori [Nor08] states that those species hardly influence the other reactions, which justifies the post-processing procedure. Furthermore it can be seen that the chemiluminescence species occur only within a very short period of time. Therefore the integration length in Eqn. 4.20 has no influence on the results as long as it is set to more than 1 mm at an assumed flow velocity of $30\,\mathrm{m\,s^{-1}}$. In other words this means that the integrated chemiluminescence intensity of OH* or CH* corresponds to the area under the OH* or CH* curve in Fig. 4.12.

Numerically obtained chemiluminescence intensity ratios (I_{OH*}/I_{CH*}) are used to interpret the effects seen in the experiments in section 5.2.

5 Results and Discussion

In this chapter the results obtained by applying the methods described in chapters 3 and 4 are presented. The chapter is divided into two main parts – the first part deals with auto-ignition. All simulated data throughout the first part are found by the 3D-RANS – flamelet model. The second part of this chapter shows chemiluminescence measurements and simulations. Numerical results are calculated with the reactor model.

5.1 Auto-Ignition

All data presented in this section are obtained from measurements done on the sequential combustor in non-premixed operation mode (see section 3.1.6).

5.1.1 Flame Images

Similar to what was reported in other publications [GMM09, MM05], auto-ignition in the current experiment starts with ignition kernels in regions with low temperature gradients and low scalar dissipation rates. The growth of two ignition kernels is shown in Fig. 5.1.

Flow direction is in horizontal direction from left to right and time progresses in vertical direction (top-down). The time step between the frames is $1/7500\,\mathrm{s}$. Although it looks as if the ignition kernels occur periodically, a frequency analysis did not return a corresponding result.

Ignition kernels grow continuously and finally form flames of the shape shown in Fig. 5.2. There the frame rate is set to $1000\,\mathrm{s}^{-1}$. The flame front is wrinkled and disrupted. It can be assumed that broken reaction layers occur, similar to the ones that Micka et al. [MD11] observe in their study. To get more insight into that, PLIF measurements would be necessary.

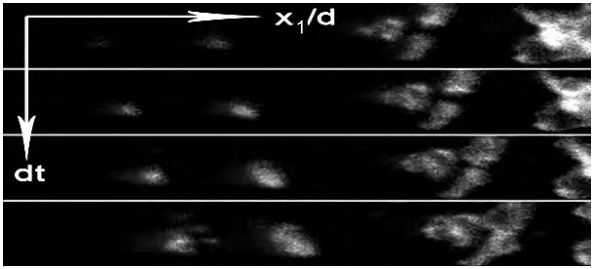

Figure 5.1: OH* raw images of ignition kernels. Time between two images: 133 μs, exposure time: 66 μs. Combustor pressure: $p = 3$ bar, Momentum flux ratio: $J = 20$.

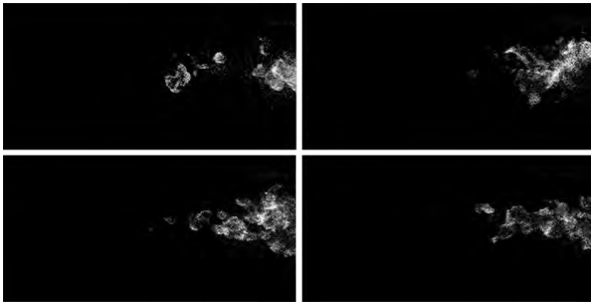

Figure 5.2: OH* raw images of the flame. Time between two images: 1 ms, exposure time: 50 μs. Combustor pressure: $p = 3$ bar, momentum flux ratio: $J = 20$.

Shape and lift-off height (see section 3.3.1) vary from image to image. To get an idea in which range lift-off height varies, histograms of four lift-off height measurements are shown in Fig. 5.3. Parameters of the corresponding experiments are given in Tab. 5.1.

As seen there, temperature needs to be increased with decreasing pressure, in order to observe the flame in the test rig's windows. At higher pressures the oxygen content in the vitiated flow is essentially constant since the temperature variation could be adjusted through the electrical preheater power. At 1 bar the electrical preheater reaches its temperature limits such that the vitiator needs to be operated at a lower air excess ratio to reach sufficiently high inlet temperatures at the inlet of the second combustion stage.

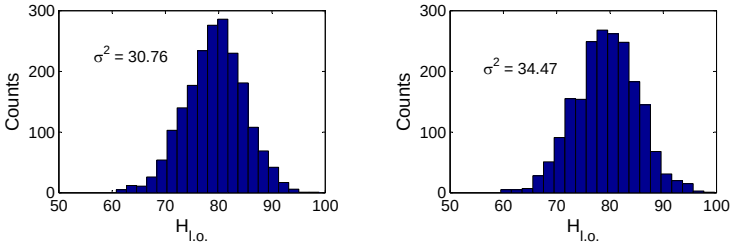

(a) $p = 1\,\text{bar}$. **(b)** $p = 2\,\text{bar}$.

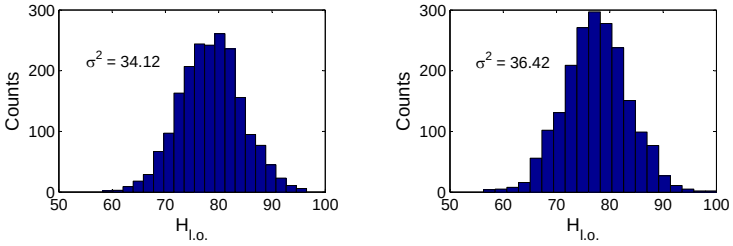

(c) $p = 4\,\text{bar}$. **(d)** $p = 6\,\text{bar}$.

Figure 5.3: Histograms of lift-off heights for different pressures. Experimental parameters given in Tab. 5.1.

p in bar	T_{in_2} in K	O_{2,dry,in_2} in %	J
1	1495	11.6	100
2	1351	12.7	100
4	1319	12.8	100
6	1310	13.1	100

Table 5.1: Parameters of the experiments as shown in Fig 5.3.

The histograms of lift-off height shown in Fig. 5.3 have symmetrical Gaussian shape. Owing to the temperature adjustments the median lift-off height is about 80 nozzle-diameters for all experiments. The fluctuations of lift-off height are in the range of ± 20 nozzle-diameters with a variance that ranges from 31 to 36. As temperature is the main driver for auto-ignition, it is assumed that temperature

fluctuations emerging from mixture fluctuations and temperature fluctuations of the inlet temperature at the second combustion stage are the main cause for the fluctuations of lift-off height.

As a simultaneous measurement of lift-off height and temperature fluctuation is not possible with this experimental setup, the latter are not considered any further in this study. Therefore mean values are used for analysis of the lift-off height.

5.1.2 Shape of the Flame

Figure 5.4 shows mean OH* chemiluminescence images of four measurements and line of sight integrated progress variable images of corresponding combustion simulations.

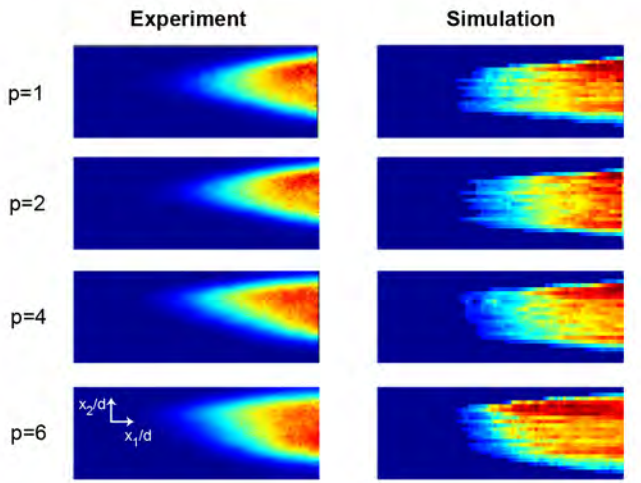

Figure 5.4: Mean images of the flame (experiment, left) and line of sight integrated progress variable (simulation, right). Parameters see Tab. 5.1.

Owing to the very simple but computationally inexpensive Lagrangian solution algorithm described in section 4.1.2, the transverse transport of the Lagrangian

particles was neglected. Therefore the numerical solution becomes stratified in radial direction. However, dominant features of the ignition delay can be found in both images. Flow direction is from left to right.

The asymmetry observed in the flame shape of the experiments may have its root cause in the unsymmetrical temperature profile due to the fuel injection lance as discussed in section 4.1.1. Also an off-axis displacement of the incoming flow due to a downward shift of the high temperature insulation upstream of the injector could cause such an asymmetry: Axial velocity increases towards the direction the insulation is displaced i.e.: if the insulation is displaced downwards, velocity will be higher in the section below than in the section above the central lance. The asymmetric velocity field has several effects: On the one hand, the fuel jet is slightly bent to the low-velocity part. Furthermore, higher velocity means lower residence time and therefore a higher lift-off height. Both effects lead to an asymmetric flame shape. Though care was taken to position all parts correctly already the parts tolerances may explain such deviation, as they were handcrafted.

In the simulation it was found that a downward-shift of 4 mm of the high temperature insulation (green colored part in Fig. 5.5) was needed to achieve a flame shape resembling that of the experiment.

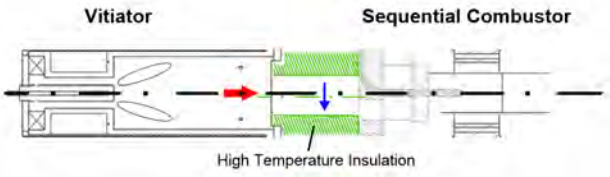

Figure 5.5: The green colored high temperature insulation might have been shifted downwards.

Pressure seems to enlarge the flame's diameter (see Fig. 5.4). Reasons for that might be an increasing reactivity (shorter ignition delay) at higher pressure and a more homogenous temperature field (see section 5.1.3.2).

5.1.3 Parameters Influencing Auto-Ignition

In this section simulated and experimental data is shown and compared to each other. The influences of area expansion, momentum flux ratio, pressure and oxygen content in the main flow on lift-off height are analyzed.

Temperature Field in the Second Combustion Chamber

As already shown in section 2.1.3, temperature has a strong influence on auto-ignition. Therefore it is important to understand the temperature field in the combustion chamber. Figure 5.6 shows the central plane of the simulated temperature field shortly after the injector in the second combustion chamber. As the central lance is water-cooled, a region of low temperature is seen in the wake of it. In the next sections it is shown that some observed effects only occur because of such a temperature profile.

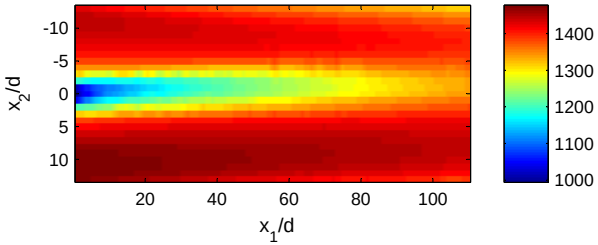

Figure 5.6: Simulated oxidator temperature field in the second combustor at 1 bar. Central plane shown.

Comparison Between Experiment and Simulation

Figure 5.7 illustrates that the combustion model can reproduce the lift-off height measured in the experiments. Results of four lift-off height measurements and the corresponding lift-off heights obtained in combustion simulations at 1 bar, 2 bar, 4 bar and 6 bar are shown. On the secondary axis the temperature at the inlet of the second combustion stage is plotted. Parameters of the experiments and simulations are given in Tab. 5.2. As already described in section 5.1, the inlet temperature needs to be increased with lower pressure to observe the flame through the test rig's windows.

The error between lift-off heights found in the experiment and simulated lift-off heights lies within 20%. Keeping in mind the simplicity of the model and that the combustion simulation is done in a post-processing step, the comparison is rather acceptable.

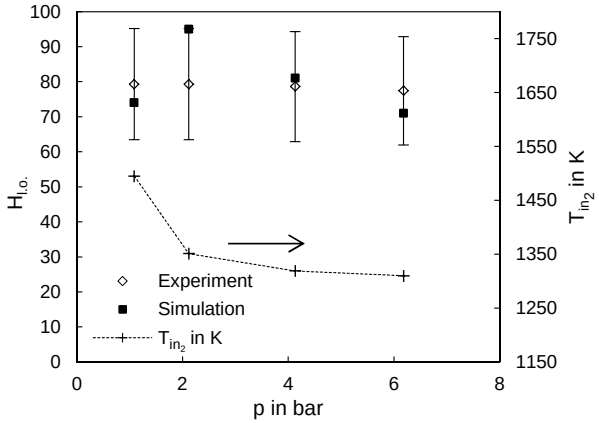

Figure 5.7: Calculated lift-off heights are compared to lift-off heights found in the experiment. The error bars indicate an error of 20 %. The secondary axis shows the temperature of the main flow at the inlet of the second combustion stage.

Experiment & Simulation				
Configuration	p in bar	T_{in_2} in K	O_{2,dry,in_2} in %	J
	1	1495	11.6	100
"Without area	2	1351	12.7	100
expansion"	4	1319	12.8	100
	6	1310	13.1	100

Table 5.2: Parameters of the experiments and the simulations shown in Fig. 5.7.

It is necessary to point out that the simulated absolute lift-off height strongly depends on the temperature at the inlet of the second combustion stage and therefore on the thermal model of the vitiator (see section 3.1.3). E.g.: at 6 bar, a relative temperature change of 2.6% (34 K) leads to a relative change of lift-off height of 23 % (16 nozzle-diameters) in the simulation. Since the inherent dependency on small errors of the inlet temperature would obscure the parameter influences sought after i.e. the dependence on pressure or oxygen content, it was chosen to normalize the lift-off height, such that the absolute temperature influence is reduced.

Due to the strong dependency on the inlet temperature and therefore on the thermal model of the vitiator, the ability of the combustion model to predict absolute lift-off heights without any validation data at hand should not be relied upon in future work.

5.1.3.1 Influence of Area Expansion on Lift-off Height

Experiments show that an area expansion slightly reduces the lift-off height (see Fig. 5.8).

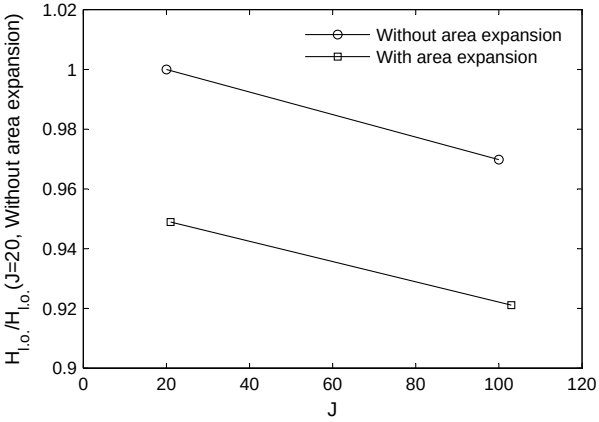

Figure 5.8: An area expansion reduces the lift-off height. The values are normalized to the maximum lift-off height.

The smallest mean lift-off height of the experiments shown in Fig. 5.8 is 79 nozzle-diameters. The area expansion is located at 70 nozzle-diameters (see also section 3.1.5), hence the majority of ignition events takes place after the area expansion. Therefore the reason for the reduced lift-off height might be the decay of the flow velocity originating from the expansion of the jet in the larger tube. Direct interaction between flame and area expansion is unlikely, as the mean minimum distance amounts to approximately 18 mm in axial and radial direction. No numerical data is available for the case “with area expansion”. Furthermore the influence of momentum flux ratio on lift-off height is investigated in the next section. Hence

no simulated data is plotted in Fig. 5.8. Table 5.3 shows the experimental parameters.

Experiment				
Configuration	p in bar	T_{in_2} in K	O_{2,dry,in_2} in %	J
"Without area	3	1301	13.6	20
expansion"	3	1303	13.6	100
"With area	3	1308	13.7	20
expansion"	3	1299	13.7	100

Table 5.3: Parameters of the experiments shown in Fig. 5.8.

5.1.3.2 Influence of Momentum Flux Ratio on Lift-off Height

According to Fig. 5.9, the influence of the momentum flux ratio on the lift-off height depends on pressure. Experiments at 1 bar show that an increasing momentum flux ratio decreases the lift-off height. In contrast to that, measurements at 6 bar indicate no influence of the momentum flux ratio on the lift-off height.

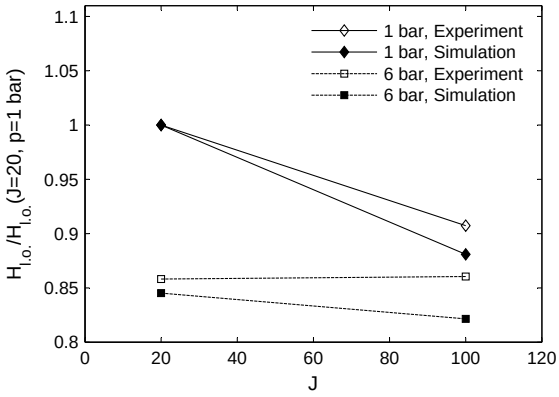

Figure 5.9: Lift-off height normalized by the lift-off height at $J = 20$, $p = 1$ bar. With increasing momentum flux ratio the lift-off height decreases at 1 bar. At 6 bar the effect vanishes in the experiment, in the simulation the effect decreases.

The simulations show an effect of the momentum flux ratio on the lift-off height at both pressure levels. Nevertheless, in the simulations, increasing pressure reduces the effect significantly. Parameters of experiment and simulation are shown in Tab. 5.4.

Experiment & Simulation				
Configuration	p in bar	T_{in_2} in K	O_{2,dry,in_2} in %	J
"Without area expansion"	1	1513	11.5	20
	1	1495	11.7	100
	6	1306	14.0	20
	6	1305	14.0	100

Table 5.4: Parameters of the experiments and the simulations shown in Fig. 5.9.

A possible explanation for this behavior is given in Fig. 5.10. There, mixture fraction profiles at $J = 20$ and $J = 100$ obtained in water channel measurements and simulated temperature profiles at 1 bar and 6 bar are shown.

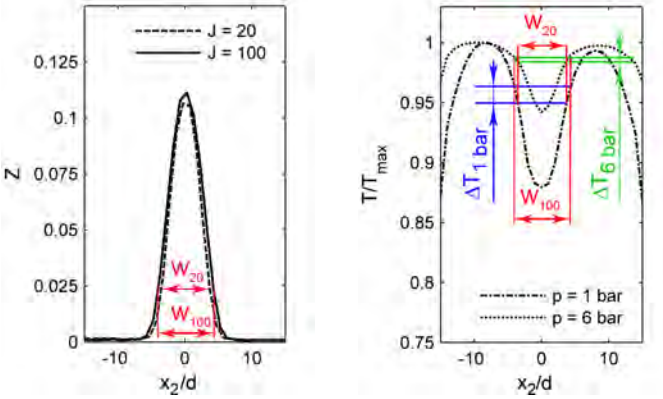

(a) Mixture fraction profiles from water channel measurements for $J = 20$ and $J = 100$, $Re_\infty \approx 47\,000$.

(b) Simulated temperature profiles of main flow for 1 and 6 bar. Curves are normalized by their maximum value.

Figure 5.10: Mixture fraction profiles and temperature profiles of main flow at $x_1/d = 70$.

It can be seen that a change of the momentum flux ratio changes the width of the mixture profile. As an example, the width W of the profiles for a given mixture fraction value of $Z = 0.025$ is shown in Fig. 5.10a. With increasing momentum flux ratio, the mixture profiles get wider and, therefore, fuel penetrates deeper into hotter zones of the main flow. This leads to a lower lift-off height with increasing momentum flux ratio at 1 bar as observed in Fig. 5.9. These results confirm the findings of Oldenhof et al. [OTvVR11].

At 6 bar, the temperature of the main flow becomes more homogenous (see Fig. 5.10b). Therefore, the wider mixing profile results in a smaller increase of temperature for the outer zones of the fuel jet ($\Delta T_{1bar} > \Delta T_{6bar}$). As a result, the experiment does not yield a significant effect of the momentum flux ratio on the lift-off height. In the simulation at 6 bar the effect of momentum flux ratio is also greatly reduced, but still the lift-off height is slightly higher for $J = 20$ than for $J = 100$.

According to the experimental data at 1 bar, a relative change of the momentum flux ratio of 10 % leads to a relative change of the lift-off height of only 0.2 %.

5.1.3.3 Influence of Pressure on Lift-off Height

In Fig. 5.11 the experimental and simulated lift-off heights have been plotted over pressure together with the ratio p_{ref}/p. It can be observed that the lift-off height decreases with pressure. This is expected as the auto-ignition time decreases with increasing pressure (see section 2.1.3).

From correlations of ignition delay time one could infer that the pressure ratio p_{ref}/p (here $p_{ref} = 2\,\text{bar}$) is a good approximation for the influence of pressure on the lift-off height. As seen in Fig. 5.11 this is clearly not the case. The pressure ratio highly overestimates the effect of pressure on the lift-off height. It is necessary to point out that the unbiased influence of pressure on auto-ignition cannot be measured with the presented experiment as the temperature field changes with pressure (see Fig. 5.10b). Furthermore calculations of the inlet temperature to the second combustion chamber (see Tab. 5.5) show that the temperature had been a bit higher for the 2 bar measurement compared to the other measurements which decreases the pressure effect.

To learn more about the unbiased pressure effect on lift-off height, simulations are conducted in which the temperature field of the main flow is taken from the

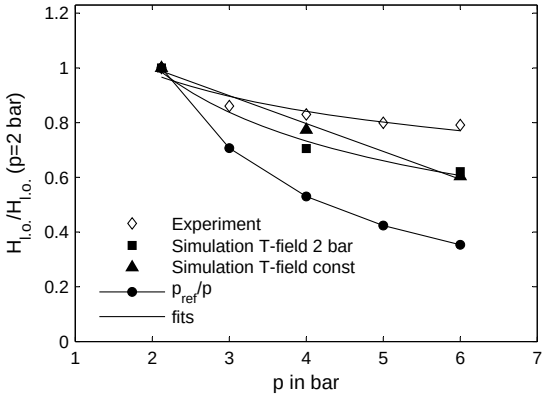

Figure 5.11: Lift-off height normalized by the lift-off height at 2 bar. Filled squares: the 2 bar temperature field of the main flow is used for the 4 and 6 bar simulation. Filled triangles: constant temperature field. The dots represent the pressure ratio.

2 bar case, whereas the influence of pressure on the chemistry table and the mixture field is considered. In addition, simulated data is shown (filled triangles in Fig. 5.11) where constant temperature at $T_\infty = 1400\,\mathrm{K}$ was assumed. In contrast to the simulations with temperature profile, the simulations with constant temperature field show almost linear dependency of lift-off height on pressure. Therefore the temperature profile in the main flow influences the pressure effect as well. Measurements of Goy et al. [GMT01] show that the pressure effect on auto-ignition time depends on the temperature level (see section 2.1.3). This might explain why a temperature profile in the main flow influences the pressure effect.

According to the experimental data, a relative change of the pressure of 10 % leads to a relative change of the lift-off height of 1 %.

Experiment				
Configuration	p in bar	T_{in_2} in K	O_{2,dry,in_2} in %	J
"With area expansion"	2	1345	13.6	100
	3	1294	13.6	100
	4	1291	13.6	100
	5	1297	13.7	100
	6	1298	13.6	100
Simulation, flow field and temperature field of 2 bar				
"Without area expansion"	2	1366	12.7	100
	4	1366	12.7	100
	6	1366	12.7	100
Simulation, T_∞ =const= 1400 K				
"Without area expansion"	2	1400	12.7	100
	4	1400	12.7	100
	6	1400	12.7	100

Table 5.5: Parameters of the experiments and the simulations shown in Fig. 5.11.

5.1.3.4 Influence of Oxygen Content on Lift-off Height

In Fig. 5.12 the lift-off height as a function of dry oxygen content at the inlet of the second combustion stage is plotted. The secondary vertical axis represents the calculated inlet temperature of the main flow of the experiments. Less oxygen at the inlet of the second combustion chamber increases auto-ignition time as Eqn. 2.5 shows. Hence lift-off height increases with decreasing oxygen content. Data for experiment and simulation are given in Tab. 5.6. Only one measurement (without area expansion, O_{2,dry,in_2}=14.8 %) does not follow the expected trend. Compared to the other "without area expansion" measurements the inlet temperature was the lowest, which might explain that behavior. The reason for the lift-off height reacting more sensitively on changes of the oxygen content if there is an area expansion might be measurement uncertainties.

In the simulations the flow field and the temperature field are kept constant for all three cases shown. Comparing the linear fit to all measurements and the linear fit to the simulations, the slope of the latter is larger than the slope of the fit to the

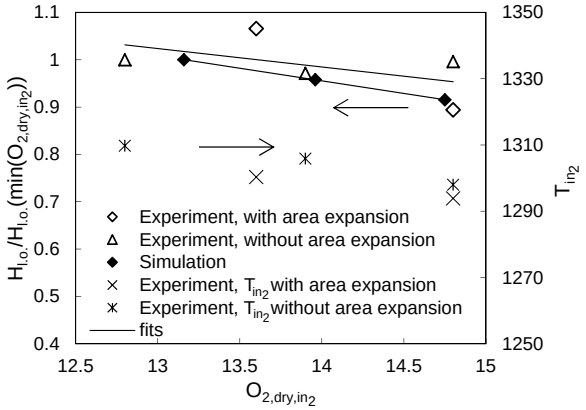

Figure 5.12: Lift-off height normalized by the lift-off height at the lowest oxygen content. With increasing oxygen content at the inlet of the second combustion chamber the lift-off height decreases.

Experiment				
Configuration	p in bar	T_{in_2} in K	O_{2,dry,in_2} in %	J
"Without area expansion"	6	1310	12.8	100
	6	1306	13.9	100
	6	1298	14.8	100
"With area expansion"	6	1300	13.6	100
	6	1294	14.8	100
Simulation. Flow field and temperature field of O_{2,dry,in_2}=13.16 %-case				
"Without area expansion"	6	1305	13.16	100
	6	1305	13.96	100
	6	1305	14.75	100

Table 5.6: Parameters of the experiments shown in Fig. 5.12.

measurements. The decreasing inlet temperature to the second combustion stage with increasing oxygen content might be an explanation for that result.

According to the experimental data, a relative change of the oxygen content of the co-flow of 10 % leads to a significant relative change of the lift-off height of 15 %.

5.1.3.5 Regression Model for Lift-off Height

Linear regression analysis is done on 77 measurements. The variation range of the experimental parameters are given in Tab. 5.7. Data analysis with SPSS [Cor12] yields the exponents for the relation in Eqn. 5.1.

p in bar	T_{in_2} in K	O_{2,dry,in_2} in %	J	$H_{l.o.}$
1	1442…1558	11.3…11.7	20…200	67…87
2	1324…1369	11.7…13.5	20…200	69…89
3	1282…1341	11.9…13.7	20…200	64…93
4	1269…1346	12.0…13.9	10…100	68…97
5	1269…1342	12.0…13.9	10…100	68…97
6	1270…1348	12.1…14.7	10…100	66…92

Table 5.7: Ranges of varied parameters of the experiments used for the linear regression analysis.

Independent variables are the oxidator temperature at the inlet of the second combustor, oxygen content in the oxidator, momentum flux ratio and pressure. The dependent variable is the lift-off height. All independent variables reach statistical significance (see section 2.5.3).

$$H_{l.o.} = 78.524 \cdot \left(\frac{T_{in_2}}{T_{in_2,ref}}\right)^{-1.668} \cdot \left(\frac{O_{2,dry,in_2}}{O_{2,dry,in_2,ref}}\right)^{-0.6} \cdot \left(\frac{p}{p_{ref}}\right)^{-0.088} \cdot \left(\frac{J}{J_{ref}}\right)^{-0.046}. \tag{5.1}$$

The determination coefficient with a value of $R^2 = 0.548$ means high predictive power (see section 2.5.1). The reference values are: $T_{in,ref}$=1337.85 K, $O_{2,ref}$=12.91 %, p_{ref}=3.54 bar, J_{ref}=72.95. According to the exponents, temperature has the strongest influence on lift-off height, followed by the oxygen content in the vitiated flow, pressure and momentum flux ratio.

5.2 Air Excess Ratio at Auto-Ignition

Chemiluminescence measurements of the premixed swirl flame (see Fig. 3.2), reactor simulations and measurements of the premixed vitiated flame (see Fig. 3.5) are analyzed in the first part of this section. In the further parts the three-lens method is validated and applied to the auto-igniting, non-premixed (see Fig. 3.6) fuel jet to measure air excess ratios at which auto-ignition occurs.

5.2.1 Parameters Influencing Chemiluminescence

Vitiated conditions and pressure are investigated regarding their influence on chemiluminescence and chemiluminescence intensity ratio, respectively. All given experimental data in this subsection are spectrally resolved, line of sight measurements (see section 3.3.3). The sequential combustion experiment is operated in the premixed mode (see Fig. 3.5). In this mode it is possible to predetermine the air excess ratio by adjusting the fuel mass flow in the second combustion stage. The aim is to obtain information about the chemiluminescence intensity ratio at a known air excess ratio. The data is compared to non-vitiated data from measurements done on the premixed swirl flame. If not stated otherwise, throughout this section all chemiluminescence intensity ratios are normalized by the I_{OH*}/I_{CH*} value measured in the swirl flame at an air excess ratio of $\lambda = 1.35$ and a pressure of $p = 1\,\text{bar}$.

Simulations are conducted with the constant pressure reactor model presented in section 4.2.2 to get a better understanding of the effects seen in the experiments.

5.2.1.1 Influence of Vitiation on Chemiluminescence

Figure 5.13 shows the chemiluminescence intensity ratio of OH* and CH* as a function of the global air excess ratio (see also section 3.3.2), based on the oxygen content of ambient air ($X_{O_2} = 20.85\%$). Parameters are given in Tab. 5.8. For the reactor simulation of the vitiated case a constant inlet temperature of $T_{in_2} = 1205\,\text{K}$ is used and the gas composition of the vitiated case is calculated with Cantera, as only the dry oxygen content is measured.

Accordig to Fig. 5.13 the sequential combustion process influences the chemiluminescence signal – the I_{OH*}/I_{CH*} ratio decreases for all air excess ratios and the

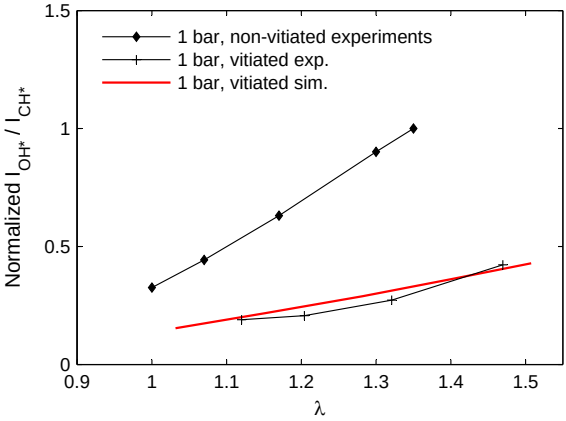

Figure 5.13: Spectrometer measurements and simulations (red line) show the OH*/CH* chemiluminescence intensity ratio at 1 bar as a function of the air excess ratio. The upper line represents the swirl burner case, the lower the vitiated case.

Experiment						
Configuration	p in bar	T_{in} in K	X_{N_2} in %	X_{O_2} in %	X_{CO_2} in %	X_{H_2O} in %
Swirl burner – non-vitiated oxidator	1	450 ± 20	20.85	79.15	0	0
Experiment & Simulation						
Configuration	p in bar	T_{in_2} in K	X_{N_2} in %	X_{O_2} in %	X_{CO_2} in %	X_{H_2O} in %
Premixed sequential combustor – vitiated oxidator	1	1205 ± 50	76.68	13.87	3.19	6.26

Table 5.8: Parameters of the experiments and the simulations shown in Fig. 5.13.

dependency on the air excess ratio decreases, too. The vitiated case is reproduced appropriately by the constant pressure reactor simulation.

The reason for the difference between the I_{OH*}/I_{CH*} ratio of the vitiated and non-vitiated combustion process is investigated in the following. Compared to the swirl burner experiment, in the sequential combustion experiment several conditions are changed: beside the flow field, preheat temperature and gas composition of the oxidator are different. Below, the influences of gas composition and preheat temperature of the oxidator are investigated in more detail.

Influence of Oxidator Temperature on Chemiluminescence

Nori and Seitzman [NS08] and Muruganandam et al. [MKM+05] investigate the influence of preheat temperature on the chemiluminescence emission ratio for a given equivalence ratio (corresponds to $1/\lambda$) in non vitiated flames. In both studies only a minor effect is seen. In this thesis only the vitiated case is investigated. Here the inlet temperature is varied from 1205 K up to 1500 K. All other parameters are kept constant. Values are shown in Tab. 5.8.

As seen in Fig. 5.14a, the OH*/CH* intensity ratio decreases monotonically with increasing inlet temperature, with decreasing slope of the curves. To find an explanation for this behavior, Eqn. 4.17 and Eqn. 4.18 of the reactor model are analyzed in more detail. The numerators of the fractions represent the formation reactions and the denominators the quenching reactions of OH* and CH*, respectively. If the numerator of the OH*-equation (Eqn. 4.17) or the denominator of the CH*-equation (Eqn. 4.18) increases, the chemiluminescence intensity ratio will increase, too. Higher values of the CH*-numerator or the OH*-denominator will have the opposite effect. Nevertheless, if numerator or denominator of Eqn. 4.17 and Eqn. 4.18 increase similarly, there will be no effect on the OH*/CH* intensity ratio. All relative changes shown in Fig. 5.14b-f are based on the values at an oxidator temperature of $T_{in_2} = 1205\,\mathrm{K}$.

The relative change of the $\mathrm{I}_{OH*}/\mathrm{I}_{CH*}$ ratios is plotted in Fig. 5.14b. With increasing air excess ratio the effect of temperature increases, a relative change of up to $-58\,\%$ is calculated. Therefore OH* and CH* respond differently on a variation of temperature.

Comparing Fig. 5.14c with Fig. 5.14d shows that the numerator of the CH*-equation is more affected by temperature than the numerator of the OH*-equation. The numerator represents the formation of the chemiluminescence species, hence more CH* than OH* is formed if temperature increases. Compared to the change in the formation reactions the change in the quenching reactions seems to play a minor role: The denominator of the OH*-equation decreases (see Fig. 5.14e) and that of the CH*-equation increases (see Fig. 5.14f). Such variations would increase the OH*/CH* chemiluminescence intensity ratio, which is not the case.

In conclusion, the reactor simulations show that a change in preheat temperature affects the OH*/CH* intensity ratio, especially at high air excess ratios. This behavior can be attributed to the formation of CH*, which strongly depends on temperature.

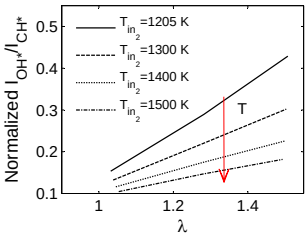

(a) I_{OH*}/I_{CH*} intensity ratio.

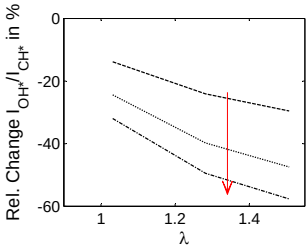

(b) Overall relative change of the I_{OH*}/I_{CH*} intensity ratio in Fig. 5.14a.

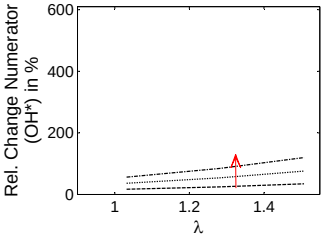

(c) Relative change of the numerator of Eqn. 4.17.

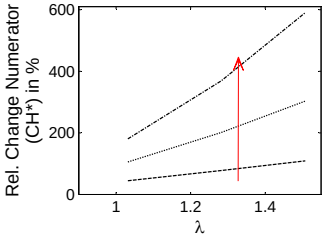

(d) Relative change of the numerator of Eqn. 4.18.

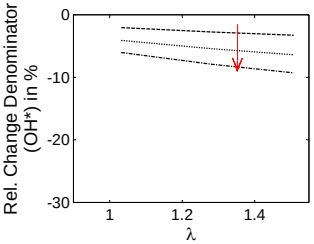

(e) Relative change of the denominator of Eqn. 4.17.

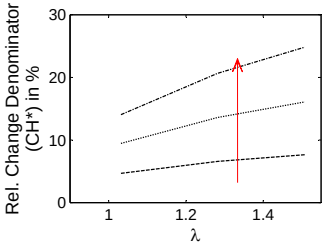

(f) Relative change of the denominator of Eqn. 4.18.

Figure 5.14: Simulation of OH*/CH* chemiluminescence intensity ratio as a function of the global air excess ratio. The inlet temperature of the oxidator to the second combustion stage is varied. All relative changes are based on the values at an oxidator temperature of $T_{in_2} = 1205\,\mathrm{K}$. Pressure for all simulations $p = 1\,\mathrm{bar}$.

Influence of Gas Composition on Chemiluminescence

To find out whether the gas composition of the main flow changes the OH*/CH* chemiluminescence intensity ratio, simulations are conducted where the amounts of N_2, O_2, H_2O and CO_2 are changed separately. Argon is used as inert gas as it does not influence any chemiluminescence reaction. Table 5.9 shows the simulated compositions[1]. The composition in the first row is used as reference. Each species is increased relatively by 50 %. Reactor simulations are done with an oxidator temperature of 1205 K at a pressure of 1 bar.

Name	X_{N_2} in %	X_{O_2} in %	X_{CO_2} in %	X_{H_2O} in %	X_{Ar}in %
Reference	50.00	12.50	3.81	7.49	26.20
X_{N_2} + 50 %	75.00	12.50	3.81	7.49	1.20
X_{CO_2} + 50 %	50.00	12.50	5.72	7.49	24.30
X_{H_2O} + 50 %	50.00	12.50	3.81	11.24	22.46
X_{O_2} + 50 %	50.00	18.75	3.81	7.49	19.95

Table 5.9: Gas compositions of the oxidator in percent per volume.

The chemiluminescence intensity ratio is plotted as a function of the local air excess ratio in Fig. 5.15a. Therefore, the air excess ratio is calculated on the basis of the oxygen content in the oxidator at the inlet of the second combustion stage. The results are analyzed similarly to the preceding section. All relative changes are based on the values computed with the reference gas composition of the oxidator, shown in Tab. 5.9. As the OH*/CH* intensity ratio does not show the same behavior for all cases of Tab. 5.9, they are treated separately:

N_2: According to Fig. 5.15b, 50 % more nitrogen in the oxidator leads to a change of up to 35 % of the OH*/CH* intensity ratio. This effect is not caused by the formation reactions, as the values of the numerators in Eqn. 4.17 and Eqn. 4.18 hardly change (see Fig. 5.15c and Fig 5.15d). In contrast to that, looking at Fig. 5.15e and Fig. 5.15f, the denominators change independently. OH* is quenched less by N_2 than CH*, because the reaction rate of the quenching reaction of CH* with N_2 is higher by an order of magnitude than the one wherein OH* reacts with N_2. Therefore the I_{OH*}/I_{CH*} chemiluminescence ratio increases with increasing nitrogen content in the oxidator.

1 Please note that the simulated gas compositions might not be found in reality. The aim of this section is to find out what happens to the chemiluminescence intensity ratio if the concentration of only one species changes.

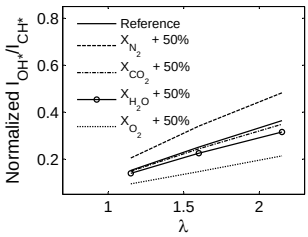

(a) I_{OH*}/I_{CH*} intensity ratio.

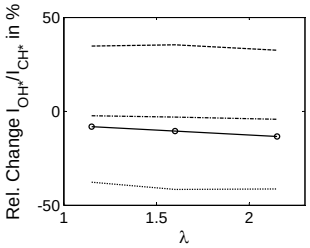

(b) Overall relative change of the I_{OH*}/I_{CH*} intensity ratio in Fig. 5.15a.

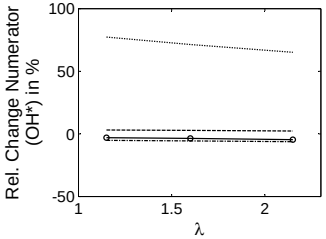

(c) Relative change of the numerator of Eqn. 4.17.

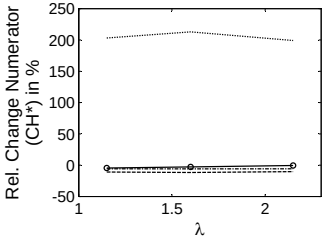

(d) Relative change of the numerator of Eqn. 4.18.

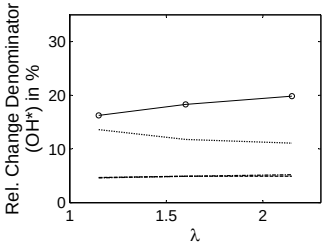

(e) Relative change of the denominator of Eqn. 4.17.

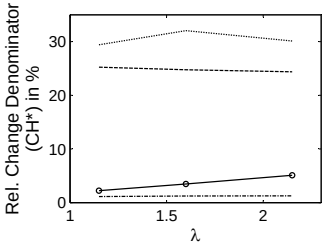

(f) Relative change of the denominator of Eqn. 4.18.

Figure 5.15: Simulation of OH*/CH* chemiluminescence intensity ratio as a function of the local air excess ratio. The content of N_2, CO_2, H_2O and O_2 is varied in the coflow (=oxidator). All relative changes are based on the values computed with the reference gas composition of the oxidator. Oxidator temperature $T_{in_2} = 1205\,\mathrm{K}$, pressure $p = 1\,\mathrm{bar}$.

O_2: The reactor simulation shows that an increasing oxygen content in the oxidator decreases the chemiluminescence intensity ratio (see Fig. 5.15a). Oxygen occurs in the formation reactions as well as in the quenching reactions for the chemiluminescence species (see Tab. 4.2). Moreover, a rise of the oxygen concentration in the oxidator leads to a higher amount of fuel that is necessary to reach the same air excess ratio. Therefore, the adiabatic flame temperature increases. As seen in the preceding section, temperature has a strong effect on the formation reactions, furthermore the concentrations of CH and C_2H increase with a higher amount of fuel. The concentration of the O-radical, which is part of the formation reactions for CH*, rises with more oxygen in the oxidator, too. Thus, the strong relative change in the numerators is a result of temperature and species' concentration.

Compared to the relative changes in the numerators, the variation in the denominators plays a minor role. The trend there would lead to an increase of the OH*/CH* chemiluminescence intensity ratio, as CH* is quenched more than OH*.

CO_2 and **H_2O:** For both species the different quenching behavior of OH* and CH* is responsible for the decrease of the chemiluminescence intensity ratio with increasing CO_2 or H_2O content.

The reaction rate of the CO_2 quenching reaction for OH* is almost twice the reaction rate for the CH* quenching reaction, though the reaction rate for the latter is highly temperature dependent. Therefore this conclusion is only valid for the investigated temperature range (adiabatic flame temperature from 1800 K to 2300 K).

On the contrary, the reaction rate of the H_2O quenching reaction for OH* is by an order of magnitude higher than the one for the CH* quenching reaction. Therefore water has a stronger effect on the OH*/CH* chemiluminescence intensity ratio than CO_2.

In the following, an attempt is made to reconstruct in the simulation the measured chemiluminescence intensity ratios of the non-vitiated experiment in Fig. 5.13. For that purpose gas composition and inlet temperature are varied. Parameters for the simulations are shown in Tab. 5.10.

In Fig. 5.16 the I_{OH*}/I_{CH*} chemiluminescence ratio is plotted as a function of the adiabatic flame temperature for different gas compositions for a fixed inlet temperature to the second combustion stage of $T_{in_2} = 1205\,\mathrm{K}$. Similar trends as described in the preceding section can be observed, though the effects of CO_2 and H_2O exceed the effect of a change in the N_2 or O_2 concentration as their

Name	T_{in_2} in K	X_{N_2} in %	X_{O_2} in %	X_{CO_2} in %	X_{H_2O} in %	X_{Ar} in %
Non-vitiated, simulation	1205	79.15	20.85	0	0	0
Less O_2	1205	79.15	13.87	0	0	6.98
Less N_2	1205	76.68	13.87	0	0	9.45
CO_2 added	1205	76.68	13.87	3.19	0	6.26
Vitiated, simulation	1205	76.68	13.87	3.19	6.26	0
Non-vitiated, experiment	450	79.15	20.85	0	0	0
Non-vitiated, simulation	1000	79.15	20.85	0	0	0

Table 5.10: Gas compositions of the oxidator for data plotted in Fig. 5.16 and Fig. 5.17.

concentrations double compared to the non-vitiated case. According to Fig. 5.16, less oxygen than in the non-vitiated curve increases the chemiluminescence ratio. If in addition to that the nitrogen concentration is decreased (see gas composition in the third line of Tab. 5.10), the chemiluminescence ratio decreases as well. The effect is very low as the N_2 concentration is only changed by $-3\,\%$. The addition of CO_2 and H_2O leads to the curve of the vitiated case that corresponds to the red line in Fig. 5.13.

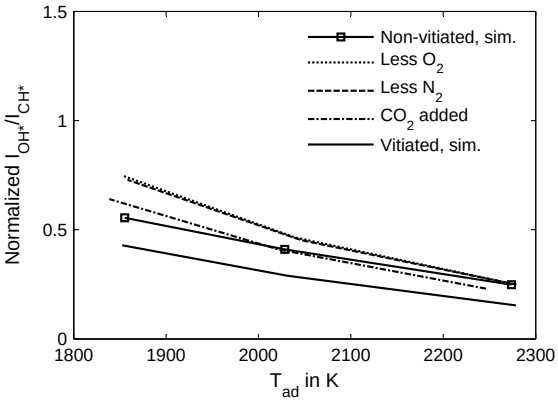

Figure 5.16: Simulated I_{OH*}/I_{CH*} ratios as a function of the adiabatic flame temperature T_{ad} for different oxidator compositions. Parameters are shown in Tab. 5.10.

Figure 5.17 shows the two already known curves of the vitiated case and the non-vitiated case. Furthermore data from a simulation where the inlet temperature to the second combustion chamber is decreased to $T_{in_2} = 1000\,\mathrm{K}$ is plotted. As

expected, the I_{OH*}/I_{CH*} ratio and the slope of the curve increase with decreasing inlet temperature, though the measured data from the non-vitiated experiment is still not met. The flow field might have an additional influence not covered by the reactor model.

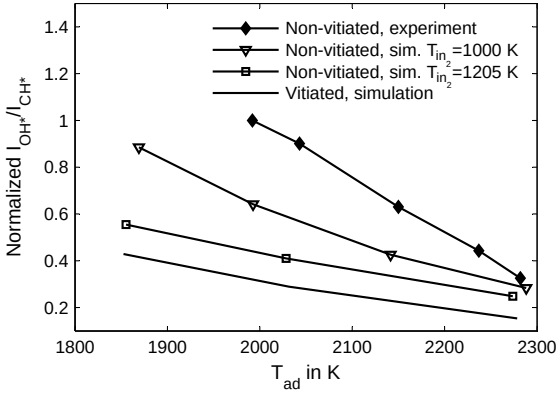

Figure 5.17: I_{OH*}/I_{CH*} ratios as a function of the adiabatic flame temperature T_{ad} for different oxidator compositions from simulation and experiment. Parameters are shown in Tab. 5.10.

In summary, an increased inlet temperature to the second combustion stage decreases the chemiluminescence intensity ratio and its sensitivity on the air excess ratio. A change in the gas composition can increase or decrease the OH*/CH* ratio, depending on which species concentration is changed. The significant differences between the results of the non-vitiated and the vitiated experiment are found to be mainly caused by the increased oxidator temperature and the changed oxidator composition. According to the simulations, temperature changes the slope of the I_{OH*}/I_{CH*}-curve and a change in the oxidator composition leads to a parallel shift.

5.2.1.2 Influence of Pressure on Chemiluminescence

All experimental results shown in this subsection are obtained from spectrometer measurements. The aim of these experiments is to investigate the influence of pressure on the OH*/CH* chemiluminescence ratio. Both combustion systems – the swirl burner and the sequential combustor in premixed mode – are examined. In Tab. 5.11 parameters of the experiments and the corresponding simulations are shown. The latter are performed to analyze the experimentally observed behavior. The first configuration essentially repeats findings from previous work to establish the validity of the experimental approach. The second configuration shown in Tab. 5.11 is used to establish the correspondence between experiment and simulation, whereas the third configuration is used to extract the unbiased pressure effect by simulation.

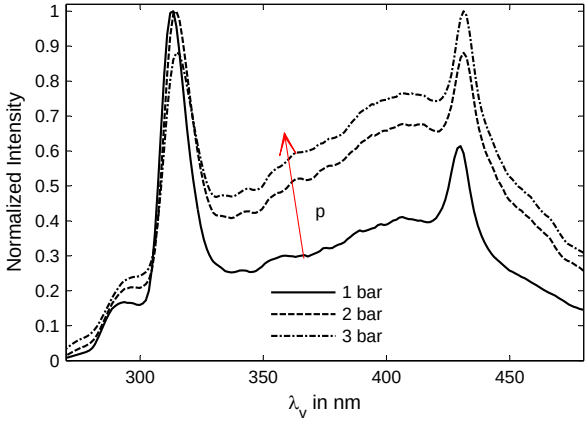

Figure 5.18: Normalized, measured spectra of the premixed swirl flame for different pressures, showing increasing relative intensity of the CO_2* chemiluminescence emissions with rising pressure. Global air excess ratio $\lambda = 1.3$.

Figure 5.18 shows that the broadband emission of CO_2* increases with rising pressure. Therefore it is important especially for higher pressures to remove the CO_2* broadband emission signal from the OH* and CH* chemiluminescence signals. More details on that issue are presented in section 3.3.3.

Experiment			
Configuration	p in bar	T_{Plenum} in K	O_{2,dry,in_2} in %
Swirl burner – non-vitiated oxidator	1…3	450 ± 20	20.85
Experiment & Simulation			
Configuration	p in bar	T_{in_2} in K	O_{2,dry,in_2} in %
Premixed sequential combustor – vitiated oxidator	1	1205 ± 50	14.8
	2	1130 ± 50	14.4
	3	1090 ± 50	14.3
Simulation			
Premixed sequential combustor – vitiated oxidator	1…3	1205	14.8

Table 5.11: Parameters of the experiments and the simulations shown in Figs. 5.19 – 5.22.

The curves shown in Fig. 5.19 are normalized by the fuel mass flow and the maximum CH*-value of the sequential combustor and the generic swirl combustor, respectively. By normalizing the OH* and CH* values by the maximum CH* value, it is still possible to calculate the chemiluminescence ratios from the figures. The normalization by the mass flow is necessary, because mass flows are increased proportionally to pressure to obtain inherent flow fields and residence times. As the chemiluminescence intensity is proportional to the fuel mass flow [HML$^+$01], the lack of normalization might result in increasing chemiluminescence intensities with increasing pressure. This must not be the case, because from literature ([HML$^+$01], [NS08]) it is known that collisional quenching is intensified at high pressure which reduces the chemiluminescence intensity.

In the experiments done with the generic swirl combustor (Fig. 5.19a and Fig. 5.19b), OH* and CH* chemiluminescence intensities decrease with increasing pressure. E.g.: at an air excess ratio of $\lambda = 1.2$ at 3 bar the OH* intensity amounts to 40 % of the signal strength at 1 bar. This finding is consistent with the experiments of Higgins et al. [HML$^+$01], and Nori and Seitzman [NS08]. As already stated, the reason for such a behavior is that collisional quenching is intensified at high pressure. In experiment (see Fig. 5.19) and simulation (see Fig. 5.20), the observation can be made that OH* and CH* respond differently to pressure. The reason for this might be found in the different pressure sensitivities of the OH* and CH* reactions, respectively.

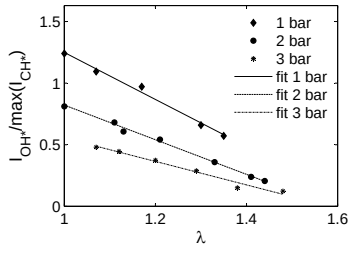

(a) Generic swirl combustor – OH*.

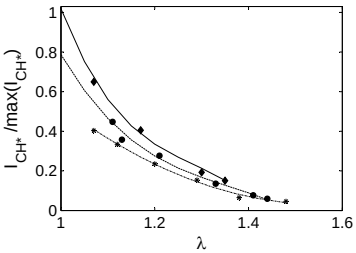

(b) Generic swirl combustor – CH*.

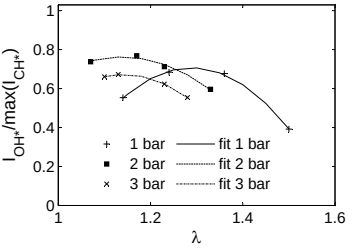

(c) Sequential combustor – OH*.

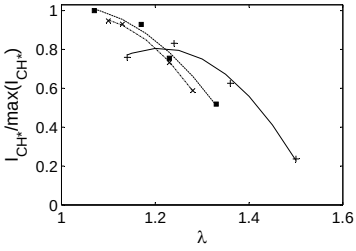

(d) Sequential combustor – CH*.

Figure 5.19: Spectrometer measurements show the influence of pressure and air excess ratio on the OH* and CH* chemiluminescence intensity. The values are normalized by the fuel mass flow and the maximum CH*-value of the generic swirl combustor and the sequential combustor, respectively.

As shown in Fig. 5.19, OH* is more pressure dependent than CH*. This observation is supported by Nori and Seitzman who state that the overall formation of OH* mainly occurs through the reaction CH+O_2 $\leftrightarrow$ OH*+CO and decreases at elevated pressure.

The experiments show that the OH* and CH* signals are less sensitive to changes of the air excess ratio in the vitiated case than in the non-vitiated case. At 1 bar unexpected values are obtained for OH* and CH* below $\lambda = 1.3$ in the vitiated case. Furthermore in the simulated data in Fig 5.20 the curvature is clearly opposite like that seen in the non-vitiated case in the experimental data. Possibly the deviation in the qualitative behavior of simulation and experiment result from the imperfect experiment. As temperature control is much less reliable at low pressure and low flow rate, it could be that the data points at 1 bar for $\lambda < 1.3$ are in error.

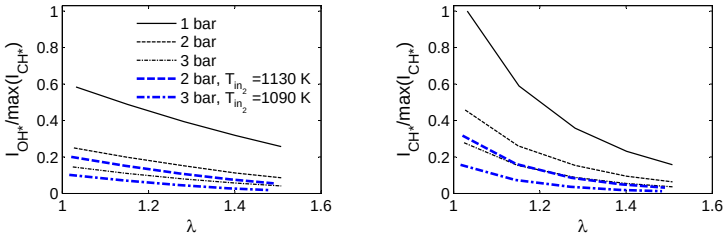

(a) Sequential combustor – OH*. **(b)** Sequential combustor – CH*.

Figure 5.20: Values of I_{OH*} and I_{CH*} simulated with the constant pressure reactor model. The values are normalized by the fuel mass flow and the maximum CH*-value of the reactor model for the sequential combustor.

Generally, for simulation and experiment, the CH* chemiluminescence signal seems to be more sensitive to changes of the air excess ratio than the OH* signal. This might be due to the stronger temperature sensitivity of CH* (see section 5.2.1.1). The blue lines in Fig. 5.20 represent simulations where the oxidator temperature was the same as calculated for the experiments. As already seen in section 5.2.1.1, a rise of temperature leads to higher chemiluminescence signals.

In Fig. 5.21 experimentally obtained chemiluminescence intensity ratios from 1 bar to 3 bar of the generic swirl combustor are shown. Again monotonic dependency on the air excess ratio are observed. This behavior can be attributed to a temperature effect. Here it is necessary to consider that the observed effects are a combination of pressure and temperature, as the heat losses to the combustion chamber wall do not increase proportional to increasing pressure (see Fig. 3.4). Hence the flame temperature increases with pressure. Therefore the pressure effect for adiabatic conditions might be lower at given air excess ratios.

The measured data at 1 bar agrees well with data from Lauer and Sattelmayer [LS10]. Compared with data from Muruganandam et al. [MKM+05] a stronger dependency on pressure is seen. The reason for this might be found in the different test rig setups. In this study the combustion chamber walls are water-cooled while the walls of the combustor used in the study of Muruganandam et al. are cooled by air. It can be assumed that a water cooled test rig wall provides significantly lower temperatures than an air cooled one. Therefore heat losses to the combustor walls are higher in the experiments conducted with the swirl burner than in the study of Muruganandam et al.

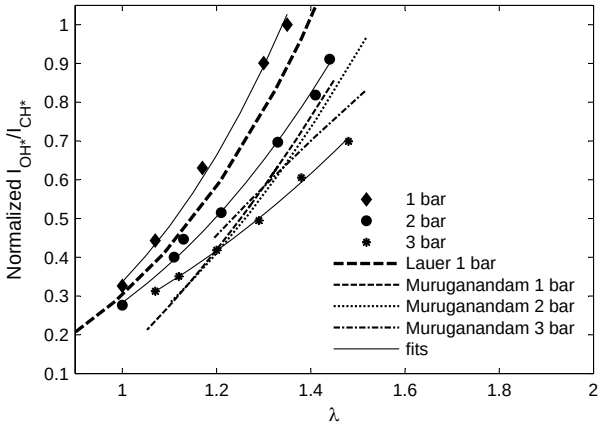

Figure 5.21: Experimentally obtained chemiluminescence intensity ratios for the generic swirl combustor for pressures of 1 bar to 3 bar.

In the sequential combustor case the pressure influence almost vanishes for low air excess ratios, see Fig. 5.22. According to the simulations at constant oxidator temperature (Fig. 5.22a), the chemiluminescence intensity ratio decreases slightly with increasing pressure. In the experimental data shown in Fig. 5.22b, the 2 bar and 3 bar measurement lies above the 1 bar measurement. The curves in blue show simulated data where the oxidator temperature was set to the same values as calculated for the experiments. Both curves lie above the simulated 1 bar curve. Therefore it is assumed that the inlet temperature to the second stage is the reason for the measurements not showing decreasing measurement values with increasing pressure. Nevertheless, the temperature effect seems to be slightly overestimated by the simulation.

In summary, OH* and CH* react differently on pressure changes, therefore the OH*/CH* chemiluminescence intensity ratio is influenced by pressure. With increasing pressure the ratio decreases. In case of the generic swirl combustor the pressure influence might be overestimated by the experiments as the combined effect of heat losses and pressure changes is observed. Both the experiments and simulations of the vitiated case show a low influence of pressure on the chemiluminescence intensity ratio.

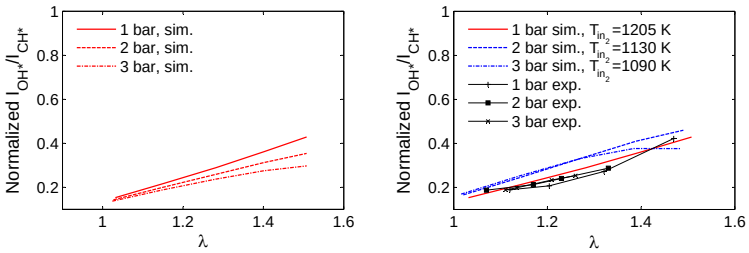

(a) $T_{in_2} = 1205\,\mathrm{K}$. **(b)** T_{in_2} varies.

Figure 5.22: Experimental and simulated data of chemiluminescence intensity ratios for the sequential combustor for pressures of 1 bar to 3 bar.

5.2.2 Three-Lens Technique

In this section the three-lens technique is validated. Data obtained with this method are compared with spectrally resolved chemiluminescence measurements. Parameters of all measurements are shown in Tab. 5.12. Figure 5.23 shows the CH*, OH* and CO_2* image of the flame of the premixed sequential combustor. The resulting OH*/CH* image shows a uniform distribution in axial as well as in radial direction, which indicates a good mixture. The mean value of the area of the OH*/CH* image is used to compare the results to the spectrometer measurements.

p in bar	T_{in_2} in K	O_{2,dry,in_2} in %	Number of Measurements
Spectrally resolved measurements			
1	1205 ± 50	14.4 ± 0.4	29
2	1130 ± 50	14.4 ± 0.4	30
3	1090 ± 50	14.4 ± 0.4	16
Three-lens method			
1	1250 ± 50	13.6 ± 0.4	10
2	1150 ± 50	13.6 ± 0.4	8
3	1120 ± 50	13.6 ± 0.4	8

Table 5.12: Parameters of the experiments shown in Fig. 5.24 and Fig. 5.25.

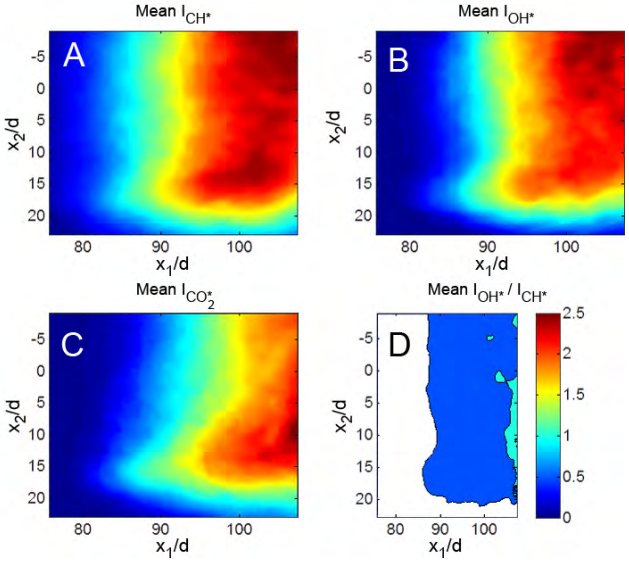

Figure 5.23: Images obtained with the three-lens technique. A, B and C show mean chemiluminescence intensities of the CH*, OH* and CO_2* radicals. The burner is operated at $p = 2$ bar and a global air excess ratio of $\lambda = 1.05$. D shows the resulting mean OH*/CH* image.

Boxplots are used to analyze the absolute deviation between spectrally resolved and three-lens method. In boxplots the bottom and top of the blue box are the first and third quartiles, and the red band inside the box is the second quartile (the median). The whiskers (the black bars) show the lowest datum still within 1.5 times the inter quartile range minus the lower quartile, and the highest datum still within 1.5 times the inter quartile range plus the upper quartile. The inter quartile range is the distance between the third and first quartile. Data points beyond the whiskers are considered to be outliers and are marked with a red cross.

The boxplots in Fig. 5.24 show the absolute deviation of spectrally resolved and three-lens method measurements from the expected λ-value (E(λ)) that is gained by fitting a curve to the spectrally resolved measurements. The three-lens method measurements are used as a reference for the air excess ratio measurements in the auto-igniting fuel jet. In the latter the oxygen content at the inlet of the second

combustion stage is in the range of 11 % to 13 % (see next section). Therefore the oxygen content in the oxidator is lower in the three-lens method measurements than in the spectrally resolved measurements. As the difference in oxygen content between three-lens method and spectrally resolved measurement method is in the range of 5 %, the impact is assumed to be in the range of the measurement uncertainty of the spectrometer measurement method.

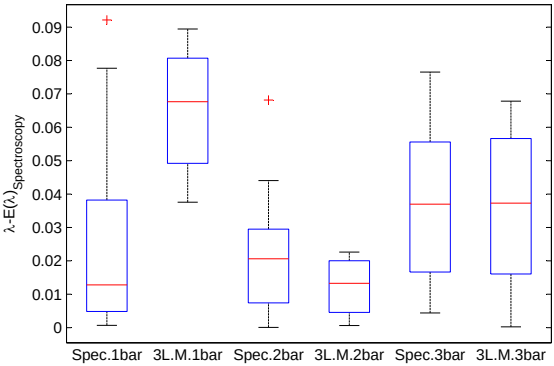

Figure 5.24: Boxplots show the absolute deviation of the spectrally resolved and three-lens method measurements from the expected λ-value (E(λ)).

According to Fig. 5.24, in the 1 bar case the deviation is rather large, but the measured values are still in the range of the spectrometer measurement method ($\lambda \pm 0.1$). At 2 bar and 3 bar the data measured with the three-lens method shows even lower deviation from the expected values than the spectrometer measurements itself. Therefore it is assumed that the presented three-lens method can be used to determine the OH*/CH* chemiluminescence ratio of a flame.

5.2.3 Air Excess Ratio Measurements

The aim of this section is to measure the air excess ratio in the auto-igniting fuel jet. This is done by measuring the chemiluminescence intensity ratio with the three-lens method.

5.2.3.1 Reference Measurements

To get the air excess ratio from the OH*/CH* chemiluminescence intensity ratio, reference measurements are necessary. These are done with the premixed sequential combustor and the parameters shown in Tab. 5.12. The obtained reference curves plotted in Fig. 5.25 are used to determine the air excess ratio of the auto-igniting fuel jet from OH*/CH* chemiluminescence intensity ratios measured with the three-lens method.

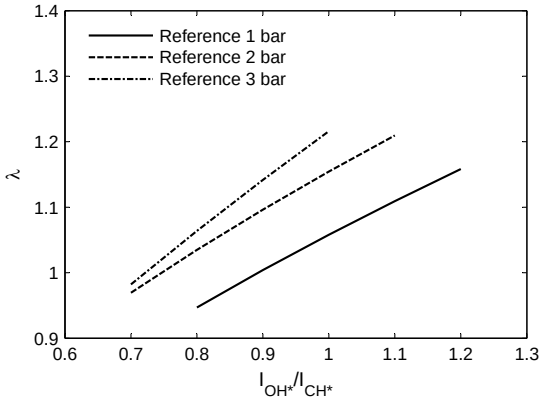

Figure 5.25: Reference curves to determine the air excess ratio from the chemiluminescence intensity ratio.

5.2.3.2 Evaluation of Air Excess Ratio in Flame Area

Before analyzing the local air excess ratios of the auto-igniting flame in more detail, the mean air excess ratio of the whole observable flame is evaluated as a function of the square root of momentum flux ratio at pressures from 1 bar to 3 bar in Fig. 5.26. The area of the recorded flame-image where the intensity counts exceed a value of 3000 (16 bit) is used to evaluate the mean air excess ratio. The square root of the momentum flux ratio can be computed with Eqn. 3.8. It is equal to the velocity ratio of jet and main flow as long as the densities are kept constant. Parameters of the experiments are presented in Tab. 5.13.

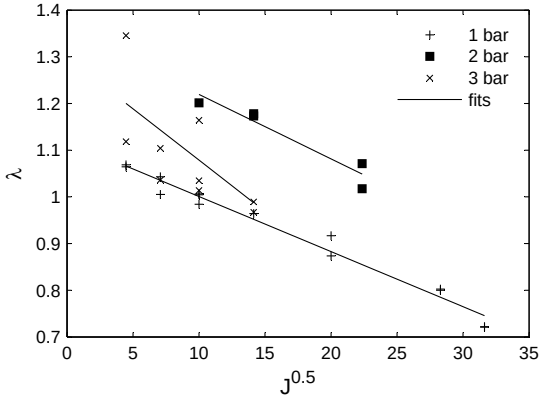

Figure 5.26: Air excess ratio as a function of the square root of momentum flux ratio. Parameters see Tab. 5.13

It has to be noted that there are significant differences in the inlet temperatures to the second combustion stage between the reference measurements (see Tab. 5.12) and the measurements done on the auto-igniting flame for all pressure levels. Furthermore the oxygen contents in the oxidator are lower in the non-premixed experiment. Therefore all absolute λ-values and comparisons between different pressure levels have to be treated with caution. In the following, only tendencies are analyzed. The reason for the discrepancies between reference measurements and measurements done on the auto-igniting fuel jet lies in the different operating points of the two burner configurations: in the premixed configuration flashback occurs if the inlet temperature is too high. On the contrary, if temperature is too low in the non-premixed auto-ignition experiment, no flame is visible in the optically accessible area of the test rig.

p in bar	T_{in_2} in K	O_{2,dry,in_2} in %	J
1	1500 ± 50	11.6 ± 0.2	20…1000
2	1320 ± 50	12.9 ± 0.2	200…500
3	1350 ± 50	12.6 ± 0.2	20…200

Table 5.13: Parameters of the experiments shown in Fig. 5.26.

As shown in Fig. 5.26, the mean air excess ratio decreases linearly with increasing velocity ratio. The reason is expected to be the increasing amount of fuel that is injected with increasing momentum flux ratio. More fuel will lead to a lower air excess ratio. Therefore the lines in Fig. 5.26 should be parallel. However, only if the two upper points of the 3 bar measurements are considered as outliers, this is the case.

5.2.3.3 Evaluation of Air Excess Ratio in Three Quadratic Areas

In the next step, mean air excess ratios are evaluated in three fixed regions of $4d \times 4d$ (see Fig. 5.27). Their center position coordinates are given in nozzle-diameter. The first coordinate denotes the axial distance from the nozzle and the second the distance from the central axis ($[x_1/d, x_2/d]$).

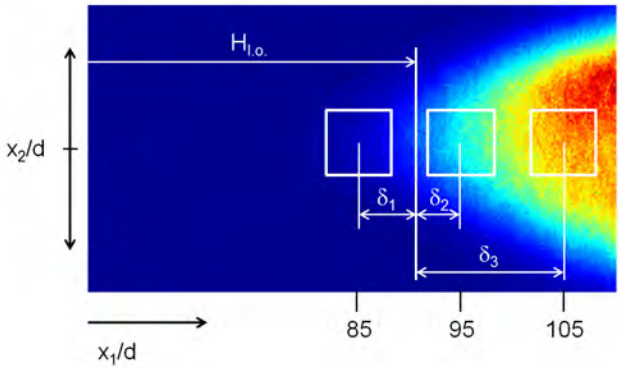

Figure 5.27: Sketch of evaluation areas.

In Fig. 5.28 mean air excess ratios are shown that are evaluated downstream of the injector at $[85,0]$, $[95,0]$ and $[105,0]$. The air excess ratio is plotted as a function of the difference between axial center coordinate of the evaluation window and mean lift-off height (δ). Experimental data of four measurements at 3 bar is shown, parameters are given in Tab. 5.14.

Inlet temperature to the second combustion chamber is varied, therefore lift-off height varies, too. It can be seen that for all four measurements the mean air excess ratio decreases from one to the next evaluation window. This means that

ignition starts at lean mixture fractions at the outer zones of the jet. Once ignited, with increasing distance from the nozzle, inner richer zones ignite, too.

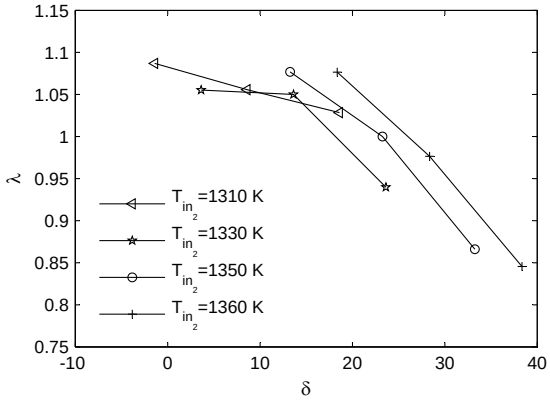

Figure 5.28: Mean air excess ratio at three different measurement areas (± 2 nozzle-diameters), plotted as a function of the difference between lift-off height and center position of evaluation window. Experimental data. Parameters see Tab. 5.14

p in bar	T_{in_2} in K	O_{2,dry,in_2} in %	J	$H_{l.o.}$
3	1310	12.6	100	86
3	1330	12.6	100	81
3	1350	12.7	100	72
3	1360	12.6	100	67

Table 5.14: Parameters of the experiments shown in Fig. 5.28.

Furthermore Fig. 5.28 shows that the difference of mean air excess ratio between the evaluation windows increases with increasing inlet temperature. This effect might be even underestimated as the dependency of the OH*/CH* chemiluminescence ratio on air excess ratio is influenced by the inlet temperature (see section 5.2.1.1). An increased inlet temperature decreases the dependency on air excess ratio, hence the slope of the reference curves in Fig. 5.25 will rise with increasing inlet temperature to the second combustion stage. In turn, this will lead to

larger differences of the air excess ratio between each evaluation window at higher inlet temperatures.

The reason for measurement data at negative values on the horizontal axis is that lift-off height fluctuates around the mean value, therefore ignition events also occur upstream of the mean lift-off height.

In the following, the center of the first evaluation area in axial direction is positioned at the mean lift-off height, given in Tab. 5.15. The second and third evaluation window are located 6 and 12 nozzle-diameters downstream the first one, respectively. Only measured data is given.

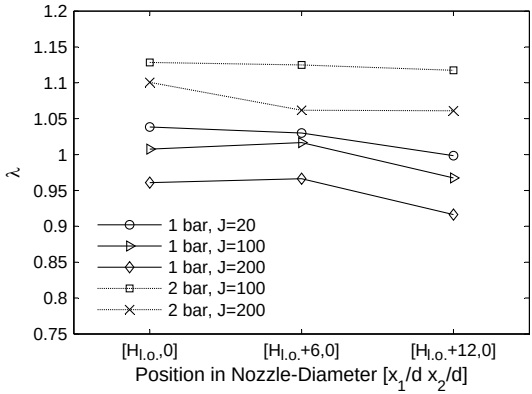

Figure 5.29: Mean air excess ratios in three different measurement areas (±2 nozzle-diameters). Momentum flux ratio and pressure are varied. Parameters see Tab. 5.15.

p in bar	T_{in_2} in K	O_{2,dry,in_2} in %	J	$H_{l.o.}$
1	1515	11.6	20	92
1	1500	11.7	100	88
1	1500	11.5	200	86
2	1330	12.8	100	94
2	1315	12.8	200	91

Table 5.15: Parameters of the experiments shown in Fig. 5.29.

According to Fig. 5.29, higher momentum flux ratios lead to slightly richer air excess ratios for all measurement areas at 1 bar and 2 bar. This is reasonable as the outer zones of the jet with low momentum flux ratio are leaner (see also Fig. 5.10a). Lift-off height might also play a role: the air excess ratio in the first measurement area increases with lift-off height. A dependency between air excess ratio and lift-off height is also reasonable, as low lift-off heights mean short mixing time and therefore low air excess ratios and vice versa.

With increasing pressure, leaner air excess ratios are obtained. A reason could be the different temperature levels at 1 and 2 bar (see Tab. 5.15), which changes the relation between OH*/CH* ratio and air excess ratio.

For all cases the tendency of lower air excess ratios with increasing axial distance (lift-off height +6 and +12) can be seen, implying that the inner, richer zones of the jet ignite there, too. At the position “lift-off height +6” some measurement points slightly lie above the value at the position “lift-off height”. This might be deduced to measurement uncertainties.

A general “most reactive mixture fraction” (see section 2.1.3) cannot be identified. The air excess ratio depends on lift-off height, the position in the flame, temperature and momentum flux ratio.

The sequential combustor in premixed operation mode, which is used for the OH*/CH* reference measurements, cannot be operated at the same inlet conditions as in non-premixed operation mode. Therefore, the role of pressure regarding the “most reactive mixture fraction” cannot be addressed.

6 Summary and Conclusions

In this thesis fuel jets in vitiated co-flow are investigated experimentally and numerically at different pressure levels.

One main focus of this work is **auto-ignition**. Influence of pressure, oxygen content in the oxidator and momentum flux ratio on lift-off height is observed in experiments and simulated. A special procedure for the computation of ignition in the second stage of a sequential combustion process is presented. It consists of the RANS simulation of the non-reacting flow and a subsequent combustion simulation on the basis of flamelets. The procedure is particularly useful in the early design phase of gas turbine combustors relying on self-ignition as the advantage of the approach is its flexibility: the model accepts either numerically derived input or experimental data for the flow-, temperature- and mixture fraction fields. The input may also originate from both sources. A further advantage of the model is its low demand regarding computational resources and turnaround time. On a PC with an Intel® CORE i7 2.7 GHz processor (only one core used) with 8 GB random access memory the average computation time for one combustion simulation is approximately two hours. The entire simulation process (RANS simulation + generation of tables + combustion simulation) is accomplished within eight hours on one PC.

The numerical results obtained from the procedure described above are compared with experimental data from optical measurements of a natural gas jet flame in a pressurized test rig. Lift-off heights and air excess ratios in the ignition zone are investigated in detail. It can be shown that increasing pressure as well as increasing oxygen content in the main flow significantly decrease lift-off height. Besides temperature, a change of the oxygen content in the co-flow has the largest impact on lift-off height, a change of momentum flux the lowest. According to the experimental data, a relative change of the oxygen content of the co-flow of 10 % leads to a significant relative change of the lift-off height of 15 %. In contrast to that, a relative change of the momentum flux ratio of 10 % leads to a relative change of the lift-off height of only 0.2 %. Furthermore, the temperature profile in the main flow influences the effect of momentum flux ratio and pressure on the lift-off height.

Linear regression analysis of 77 optical measurements of the auto-igniting fuel jet in hot co-flow leads to the exponents for the relation

$$H_{l.o.} = 78.524 \cdot \left(\frac{T_{in_2}}{T_{in_2,ref}}\right)^{-1.668} \cdot \left(\frac{O_{2,dry,in_2}}{O_{2,dry,in_2,ref}}\right)^{-0.6} \cdot \left(\frac{p}{p_{ref}}\right)^{-0.088} \cdot \left(\frac{J}{J_{ref}}\right)^{-0.046}$$

for the calculation of the lift-off height ($H_{l.o.}$), depending on the temperature of the oxidator (T_{in_2}), oxygen content in the oxidator (O_{2,dry,in_2}), pressure (p) and momentum flux ratio (J).

The second focus of this work is the investigation of **chemiluminescence**. A method for measuring the OH*/CH* chemiluminescence ratio in two dimensions is presented and verified with spectrally resolved chemiluminescence measurements. This measurement technique is applied to a vitiated auto-igniting flame. Furthermore, two different burner configurations are used to investigate how the chemiluminescence intensities of OH* and CH* are influenced by vitiation and pressure. Experimental data are compared with chemiluminescence data from reactor simulations.

The main findings are that increasing pressure as well as sequential combustion decrease the OH*/CH* ratio, but the monotonic relation between air excess ratio and chemiluminescence ratio remains. Therefore the OH*/CH* ratio is a good means to determine the air excess ratio in staged combustion processes and at elevated pressures. The reason for the decreasing OH*/CH* ratio in case of the vitiated flame is assumed to be the result of an increased oxidator temperature and the changed oxidator composition. The effect of pressure is investigated up to 3 bar. It is shown that OH* reacts more sensitive to pressure than CH*, therefore pressure affects the OH*/CH* chemiluminescence ratio, too.

The numerical procedure combining RANS and flamelet simulation as well as the relation for the lift-off height presented within this work can be useful in the early design phase of combustion chambers and also for the design of new experiments. Moreover the strong influence of vitiation on the chemiluminescence intensity of OH* and CH* needs to be considered in future chemiluminescence measurements.

The development of a relation for the air excess ratio at the point of ignition and the investigation of the influence of high pressure ($p > 3$ bar) on the chemiluminescence intensity ratio are interesting topics for future research.

Bibliography

[ABF+06] B. Ayoola, R. Balachandran, J. Frank, E. Mastorakos, and C. Kaminski. Spatially Resolved Heat Release Rate Measurements in Turbulent Premixed Flames. *Combustion and Flame*, 144:1–16, 2006.

[AT11] AG-Turbo. Ziele des Verbundprojekts COORETEC-Turbo zum Kraftwerk für den Klimaschutz. URL www.ag-turbo.de/pdf-files/Gesamtzielbeschreibung_Web_Seite.pdf, Stand 25.11.2011.

[AT12] Inc Agilent Technologies. *Agilent 34970A/34972A Data Acquisition / Switch Unit*. 900 S. Taft Ave, third edition, May 2012.

[Bai95] D.G. Bailey. Pixel Calibration Techniques. In *Proceedings of the Image and Vision Computing New Zealand*, pages 37–42, 1995.

[Bai02] D.G. Bailey. A New Approach to Lens Distortion Correction. In *Proceedings of the Image and Vision Computing New Zealand*, pages 59–64, 2002.

[BAS00] BASF Corporation. Product information: Basacid yellow 226. 2000.

[BK08] J. Brückner-Kalb. *Sub-ppm-NOx-Verbrennungsverfahren für Gasturbinen*. PhD thesis, TU München, 2008.

[BKKHS10] J. Brückner-Kalb, M. Krösser, C. Hirsch, and T. Sattelmayer. Emission Characteristics of a Premixed Cyclic-Periodical-Mixing Combustor Operated With Hydrogen-Natural Gas Fuel Mixtures. *Journal for Gas Turbines and Power*, 132(2):021505, 2010.

[Boi11] P. Boivin. *Reduced-Kinetic Mechanisms for Hydrogen and Syngas Combustion Including Autoignition*. PhD thesis, Escuela Politécnica Superior, 2011.

[BPF06] M. Brandt, W. Polifke, and P. Flohr. Approximation of Joint PDFs by Discrete Distributions Generated with Monte-Carlo Methods. *Combustion Theory and Modelling*, 10(4):535–558, 2006.

[Bra05] M. Brandt. *Beschreibung der Selbstzündung in turbulenter Strömung unter Einbeziehung ternärer Mischvorgänge*. PhD thesis, TU München, 2005.

[BS89] P. Bogacki and L. F. Shampine. A 3(2) Pair of Runge-Kutta Formulas. *Applied Mathematics Letters 2*, 4:321–325, 1989.

[BSMM01] I.N. Bronstein, K.A. Semendjaev, G. Musiol, and H. Mühlig. *Taschenbuch der Mathematik*. Verlag Harri Deutsch, 5. Auflage, 2001.

[BZ09] M. Bühner and M. Ziegler. *Statisitk für Psychologen und Sozialwissenschaftler*. Pearson Deutschland GmbH, 2009.

[Cam10] K. Cammann. *Instrumentelle Analytische Chemie: Verfahren, Anwendungen, Qualitätssicherung*. Spektrum-Akademischer Vlg., 2010.

[CEGP10] A. Ciani, A. Eroglu, F. Guethe, and B. Paikert. Full-Scale Atmospheric Tests of Sequential Combustion. In *Proceedings of ASME Turbo Expo 2010*, number GT2010-22891, 2010.

[CLYS03] Y. Cheng, F.S. Lien, E. Yee, and R. Sinclair. A Comparison of Large Eddy Simulations with a Standard k-ε Reynolds-Averaged Navier-Stokes Model for the Prediction of a Fully Developed Turbulent flow over a Matrix of Cubes. *Journal of Wind Engineering*, 91:1301–1328, 2003.

[Cor12] IBM Corp. *IBM SPSS Statistics for Windows*. Armonk, NY, Version 21.0; 2012.

[DLSKZ07] M. De Leo, A. Saveliev, L.A. Kennedy, and S.A. Zelepouga. OH and CH Luminescence in Opposed Flow Methane Oxy-Flames. *Combustion and Flame*, 149:435–447, 2007.

[DVLCP96] K. Devriendt, H. Van Look, J. Ceursters, and J. Peeters. Kinetics of Formation of Chemiluminescent $CH(A^2\Delta)$ by the Elementary Reactions of $C_2H(X^2\Sigma^+)$ with $O(^3P)$ and $O_2(X^3\Sigma_g^-)$: A Pulse Laser Photolysis Study. *Chemical Physics Letters*, 261:450–456, 1996.

[Eck05] J. Eckstein. *On the Mechanisms of Combustion Driven Low-Frequency Oscillations in Aero-Engines*. PhD thesis, TU München, 2005.

[EFHS06] J. Eckstein, E. Freitag, C. Hirsch, and T. Sattelmayer. Experimental Study on the Role of Entropy Waves in Low-Frequency Oscillations in a RQL Combustor. *Journal of Engineering for Gas Turbines and Power*, 128(2):264–270, 2006.

[FKL+06] E. Freitag, H. Konle, M. Lauer, C. Hirsch, and T. Sattelmayer. Pressure Influence on the Flame Transfer Function of a Premixed Swirling Flame. In *Proceedings of ASME Turbo Expo*, number GT2006-90540, 2006.

[FS13] T. Fiala and T. Sattelmayer. Heat Release and OH* Radiation in Laminar Non-Premixed Hydrogen-Oxygen Flames. In *51st AIAA Aerospace Sciences Meeting including the New Horizons Forum and Aerospace Exposition*, number AIAA 2013-1170, 2013.

[GGS+10] D. Guyot, F. Guethe, B. Schuermans, A. Lacarelle, and O. Paschereit. CH*/OH* Chemiluminescence Response of an Atmospheric Premixed Flame Under Varying Operation Conditions. In *Proceedings of ASME Turbo Expo*, number GT2010-23135, 2010.

[GMM09] R.L. Gordon, A.R. Masri, and E. Mastorakos. Heat Release Rate as Represented by [OH] x [CH_2O] and its Role in Autoignition. *Combustion Theory and Modelling*, 13:645–670, 2009.

[GMT01] C.J. Goy, A.J. Moran, and G.O. Thomas. Auto-Ignition Characteristics of Gaseous Fuels at Representative Gas Turbine Conditions. In *Proceedings of ASME Gas Turbine Expo*, number 2001-GT-0051, 2001.

[Goo12] D. Goodwin. Cantera: An Object-Oriented Software Toolkit for Chemical Kinetics, Thermodynamics and Transport Processes. Caltech, Pasadena, 2012. Available: http://code.google.com/p/cantera.

[Hab00] L. Haber. An Investigation Into the Origin, Measurement and Application of Chemiluminescent Light Emissions from Premixed Flames. Master's thesis, Virginia Polytechnic Institute and State University, 2000.

[HML+01] B. Higgins, M.Q McQuay, F. Lacas, J.C. Rolon, N. Darabiha, and S. Candel. Systematic Measurements of OH Chemiluminescence for Fuel-Lean, High-Pressure, Premixed, Laminar Flames. *Fuel*, 80:67–74, 2001.

[HMLC01] B. Higgins, M.Q McQuay, F. Lacas, and S. Candel. An Experimental Study on the Effect of Pressure and Strain Rate on CH Chemiluminescence of Premixed Fuel-Lean Methane/Air Flames. *Fuel*, 80:1583–1591, 2001.

[HPHS12] E.H. Haner, M. Pernpeintner, C. Hirsch, and T Sattelmayer. Simultaneous Application of PLIF and Mix-PIV: Quantification of the Measurement Precision. 2012.

[HPST68] I. Hurle, R. Price, T. Sugden, and A. Thomas. Sound Emission from open Turbulent Premixed Flames. In *Proceedings of Royal Society*, volume 303, pages 409–427, 1968.

[HTH+13] E.-M. Haner, G. Tautschnig, M. Hertweck, C. Hirsch, and T. Sattelmayer. Analysis of a Co-Flowing Fuel Injection with a Concentric Carrier-Air Inlet in Autoignition Driven Combustion Chambers. In *6th European Combustion Meeting*, 2013.

[HW69] R. M. R. Higgin and A. Williams. A Shock-Tube Investigation of the Ignition of Lean Methane and n-Butane Mixtures with Oxygen. In *12th Symposium (International) on Combustion*, pages 579–590, 1969.

[ID96] F.P. Incropera and D.P. DeWitt. *Fundamentals of Heat and Mass Transfer*. John Wiley and Sons, 1996.

[IKH02] Y. Ikeda, J. Kojima, and H. Hashimoto. Local Chemiluminescence Spectra Measurements in a High-Pressure Laminar Methane/Air Premixed Flame. In *Proceedings of the Combustion Institute*, volume 29, pages 1495–1501, 2002.

[Inc02] Fluent Inc. *Fluent 6.1 Documentation*. Centerra Resource Park, 10 Cavendish Court, Lebanon, NH 03766, 2002.

[KKA02] N. Konishi, K. Kitagawa, and N. Arai. Two-Dimensional Spectroscopic Analysis of a Flame Using Highly Preheated Combustion Air. *Journal of Propulsion and Power*, 18:199–204, 2002.

[Koh88] W. Kohler. *Turbulenz und Turbulenzstruktur in freien und eingeschlossenen Flammen*. PhD thesis, Universität Karlsruhe (TH), 1988.

[KP12] R. Kulkarni and W. Polifke. Large Eddy Simulation of Autoignition in a Turbulent Hydrogen Jet Flame Using a Progress Variable Approach. *Journal of Combustion*, 2012.

[KRM+04] R. J. Kee, F. M. Rupley, J. A. Miller, M. E. Coltrin, J. F. Grcar, E. Meeks, H. K. Moffat, A. E. Lutz, G. Dixon-Lewis, M. D. Smooke, J. Warnatz, G. H. Evans, R. S. Larson, R. E. Mitchell, L. R. Petzold, W. C. Reynolds, M. Caracotsios, P. Stewart, W. E.and Glarborg, C. Wang, O. Adigun, W. G. Houf, C. P. Chou, S. F. Miller, P. Ho, and D. J. Young. *CHEMKIN Release 4.0, Reaction Design, Inc.* San Diego, CA, 2004.

[KRS+12] T. Kathrotia, U. Riedel, A. Seipel, K. Moshammer, and A. Brockhinke. Experimental and Numerical Study of Chemiluminescent Species in Low-Pressure Flames. *Applied Physics B*, 107:571–584, 2012.

[Lau11] M. Lauer. *Determination of the Heat Release Distribution in Turbulent Flames by Chemiluminescence Imaging*. PhD thesis, TU München, 2011.

[LS03] J. Lee and D. Santavicca. Experimental Diagnostics for the Study of Combustion Instabilities in Lean Premixed Combustors. *Propulsion and Power*, 19/5:735–750, 2003.

[LS10] M. Lauer and T. Sattelmayer. On the Adequacy of Chemiluminescence as a Measure for Heat Release in Turbulent Flames With Mixture Gradients. *Journal of Engineering for Gas Turbines and Power*, 132(6):061502, 2010.

[LSBS71] A. Lifshitz, K. Scheller, A. Burcat, and G. B. Skinner. Shock-Tube Investigation of Ignition in Methane-Oxygen-Argon Mixtures. *Combustion and Flame*, 16:311–321, 1971.

[Mas09] E. Mastorakos. Ignition of Turbulent Non-Premixed Flames. *Progress in Energy and Combustion Science*, 35:57–97, 2009.

[MD11] D.J. Micka and J.F. Driscoll. Stratified Jet Flames in a Heated (1364 K) Cross-Flow. In *7th US National Technical Meeting of the Combustion Institute*, number AIAA 2011-321, 2011.

[MKM+05] T.M. Muruganandam, B.-H. Kim, M.R. Morrell, V. Nori, M. Patel, B.W. Romig, and J.M. Seitzman. Optical Equivalence Ratio Sensors for Gas Turbine Combustors. In *Proceedings of the Combustion Institute*, volume 30, pages 1601–1609, 2005.

[MM05] C.N. Markides and E. Mastorakos. An Experimental Study of Hydrogen Autoignition in a Turbulent Co-Flow of Heated Air. In *Proceedings of the Combustion Institute*, volume 30, pages 883–891, 2005.

[MSS+12] C. Mayer, J. Sangl, T. Sattelmayer, T. Lachaux, and S. Bernero. Study on the Operational Window of a Swirl Stabilized Syngas Burner Under Atmospheric and High Pressure Conditions. *Journal of Engineering for Gas Turbines and Power*, 134, 2012.

[NK99] V. Nilsen and G. Kosály. Differential Diffusion in Turbulent Reacting Flows. *Combustion and Flame*, 117:493–513, 1999.

[Nor08] V. Nori. *Modeling and Analysis of Chemiluminescence Sensing for Syngas, Methane and Jet-A Combustion*. PhD thesis, Georgia Institute of Technology, 2008.

[NPMW98] H. Najm, P. Paul, C. Mueller, and P. Wyckoff. On the Adequacy of Certain Experimental Observables as Measurements of Flame Burning Rate. *Combustion and Flame*, 113:312–332, 1998.

[NS08] V. Nori and J. Seitzman. Evaluation of Chemiluminescence as a Combustion Diagnostic under Varying Operating Conditions. In *46th AIAA Aerospace Sciences Meeting and Exhibition*, number AIAA 2008-953, 2008.

[OTvVR11] E. Oldenhof, M.J. Tummers, E.H. van Veen, and D.J.E.M. Roekaerts. Role of Entrainment in the Stabilisation of Jet-in-Hot-Coflow Flames. *Combustion and Flame*, 158:1553–1563, 2011.

[PCKB67] R.P. Porter, A.H. Clark, W.E. Kaskan, and W.E. Browne. A Study of Hydrocarbon Flames. In *Symposium (International) on Combustion*, volume 11, pages 907–917, 1967.

[Pet84] N. Peters. Laminar Diffusion Flamelet Models in Non-Premixed Turbulent Combustion. *Progress in Energy and Combustion Science*, 10:319–339, 1984.

[Pet12] N Peters. Skriptum Technische Verbrennung 1. URL http://decane.itv.rwth-aachen.de/fileadmin/LehreSeminar/ TechnischeVerbrennung/Technische_Verbrennung.pdf, Stand 03.05.2012. RWTH Aachen.

[PHT09] C. Panoutsos, Y. Hardalupas, and A.M.K.P. Taylor. Numerical Evaluation of Equivalence Ratio Measurement Using OH* and CH* Chemiluminescence in Premixed and Non-Premixed Methane-Air Flames. *Combustion and Flame*, 156:273–291, 2009.

[PI04] H. Pitsch and M. Ihme. An Unsteady/Flamelet Progress Variable Method for LES of Nonpremixed Turbulent Combustion. In *43rd AIAA Aerospace Sciences Meeting and Exhibit*, number AIAA 2004-557, 2004.

[Pit00] H. Pitsch. Unsteady Flamelet Modeling of Differential Diffusion in Turbulent Jet Diffusion Flames. *Combustion and Flame*, 123:358–374, 2000.

[Pop00] S.B. Pope. *Turbulent Flows*. Cambridge: Cambridge University Press, 2000.

[RGB+09] L.S. Rothman, I.E. Gordon, A. Barbe, D.C. Benner, P.F. Bernath, M. Birk, V. Boudon, L.R. Brown, A. Campargue, J.-P. Champion, K. Chance, L.H. Coudert, V. Dana, V.M. Devi, S. Fally, J.-M. Flaud, R.R. Gamache, A. Goldman, D. Jacquemart, I. Kleiner, N. Lacome, W.J. Lafferty, J.-Y. Mandin, S.T. Massie, S. Mikhailenko, N. Moazzen-Ahmadi, O.V. Naumenko, A. Nikitin, J. Orphal, A. Predoi-Cross, V. Perevalov, A. Perrin, C.P. Rinsland, M. Rotger, M. Simeckova, M.A.H. Smith, K. Sung, S. Tashkun, J. Tennyson, R.A. Toth, A.C. Vandaele, and J.V. Auwera. The HITRAN 2008 Molecular Spectroscopic Database. *Journal of Quantitative Spectroscopy & Radiative Transfer*, 110:533–572, 2009.

[Rod07] G. Rodewald. *Brandlehre*. 6. Auflage. Kohlhammer, 2007.

[Süß12] M. Süß. Untersuchungen zur homogenen kompressionsgezündeten Verbrennung mit Fremdzündungsunterstützung. Technical Report Band 5, Institut für Kolbenmaschinen, Karlsruher Institut für Technologie, 2012.

[Sat03] T. Sattelmayer. *Stationäre Gasturbinen*, chapter Grundlagen der Verbrennung in stationären Gasturbinen, pages 385–447. Lechner, C. and Seume, J., 2003.

[SC94] L. J. Spadaccini and M. B. Colket. Ignition Delay Characteristics of Methane Fuels. *Progress in Energy Combustion Science*, 20:431–460, 1994.

[SEB95] J.M. Samaniego, F.N. Egolfopoulos, and C.T. Bowman. CO_2* Chemiluminescence in Premixed Flames. *Combustion Science and Technology*, 109:183–203, 1995.

[SGF+] G.P. Smith, D.M. Golden, M. Frenklach, B. Moriarty, N.W. Eiteneer, T. Goldenberg, M. Bowman, R.K. Hanson, S. Song, V.V. Gardiner, W.C. Lissianski, and Z. Qin. *GRI-Mech 3.0*.

[SMS11] J. Sangl, C. Mayer, and T. Sattelmayer. Dynamic Adaptation of Aerodynamic Flame Stabilization of a Premix Swirl Burner to Fuel Reactivity Using Fuel Momentum. *Journal of Engineering for Gas Turbines and Power*, 133, 2011.

[SWM11] SWM Services GmbH. Erdgasqualität im Verteilungsnetz des Großraums München. 2011.

[TBH+98] M. Tamura, P.A. Berg, J.E. Harrington, J. Luque, J.B. Jeffries, G.P. Smith, and D.R. Crosley. Collisional Quenching of CH(A), OH(A), and NO(A) in Low Pressure Hydrocarbon Flames. *Combustion and Flame*, 114(3-4):502–514, 1998.

[Ter04] D.A. von Terzi. *Numerical Investigation of Transitional and Turbulent Backward-Facing Step Flows*. PhD thesis, The University of Arizona, 2004.

[THHS13] G. Tautschnig, B. Hampel, C. Hirsch, and T. Sattelmayer. Experimental Investigation of OH* and CH* Chemiluminescence under Varying Operating Conditions. In *Proceedings of ASME Turbo Expo*, number GT2013-95850, 2013.

[THHS14] G. Tautschnig, E.-M. Haner, C. Hirsch, and T. Sattelmayer. Experimental and Numerical Investigation of Confined Jets in Hot Co-Flow. In *Proceedings of ASME Turbo Expo*, number GT2014-25843, 2014.

[TN53] M.W. Thring and M.P. Newby. Combustion Length of Enclosed Turbulent Jet Flames. In *4th Symposium (International) on Combustion*, pages 789–796, 1953.

[Tur00] S.R. Turns. *An Introduction to Combustion: Concepts and Applications*. McGraw-Hill, New York, 2nd edition, 2000.

Appendix

A.1 Stable Operating Conditions of the Vitiator

In the tests the vitiator was operated in range given in Tab. A.1.1. It can be assumed that stable operation of the vitiator at different fuel mass flows, lower preheat temperature and higher pressure is possible, too.

p in bar	Air Mass Flow in g s^{-1}	Fuel Mass Flow in g s^{-1} (T_{Plenum} in °C)	λ
1	20	0.46 (310) ... 0.56 (340)	2.87 ... 2.35
2	40	0.90 (400) ... 1.11 (220)	2.66 ... 2.16
3	60	1.32 (430) ... 1.64 (140)	2.72 ... 2.19
4	80	1.68 (430) ... 2.12 (130)	2.85 ... 2.26
5	100	2.11 (410) ... 2.68 (80)	2.84 ... 2.24
6	120	2.20 (490) ... 3.20 (80)	3.27 ... 2.25

Table A.1.1: Operating conditions of the vitiator in the tests.

A.2 Beta Distribution

The beta distribution is a family of probability distributions defined on the intervall [0,1] and parametized by two shape parameters α_β and β_β (see Fig. A.2.1).

Expected value E as well as the variance σ^2 of the beta distribution are functions of the shape parameters:

$$E(Z) = \frac{\alpha_\beta}{\alpha_\beta + \beta_\beta}, \tag{A.2.1}$$

$$\sigma^2(Z) = \frac{\alpha_\beta \beta_\beta}{(\alpha_\beta + \beta_\beta)^2(\alpha_\beta + \beta_\beta + 1)}. \tag{A.2.2}$$

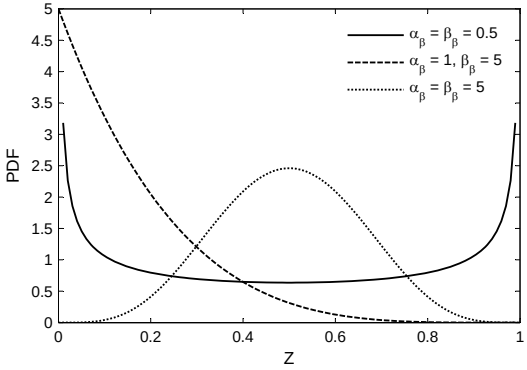

Figure A.2.1: Example beta distributions.

Hence, if mean and variance are known, α_β and β_β and therefore the shape of the beta distribution can be calculated:

$$\alpha_\beta = \frac{\frac{\gamma}{\sigma^2} - 1 - 2\gamma - \gamma^2}{1 + 3\gamma + 3\gamma^2 + \gamma^3}, \tag{A.2.3}$$

$$\beta_\beta = \alpha_\beta \cdot \gamma, \tag{A.2.4}$$

where

$$\gamma = \frac{1 - E}{E}. \tag{A.2.5}$$

Supervised Theses

Im Rahmen dieser Dissertation entstanden am Lehrstuhl für Thermodynamik in den Jahren 2009 bis 2013 unter wesentlicher wissenschaftlicher, fachlicher und inhaltlicher Anleitung des Autors die im Folgenden aufgeführten studentischen Arbeiten. Ergebnisse aus diesen Arbeiten können in Teilen in das vorliegende Dokument eingeflossen sein. Der Autor dankt hiermit nochmals explizit allen ehemals betreuten Studenten für ihr Engagement bei der Unterstützung des hier behandelten Forschungsprojekts sowie der damit verknüpften Dissertation.

Associated with the research under discussion, there are a number of different ”student theses” (Semesterarbeiten, Diplomarbeiten, Bachelor theses). This students' contribution was prepared at the Lehrstuhl für Thermodynamik in the years 2009 through 2013 under the close supervision of the author of this Ph.D. thesis with regard to all academic, professional, and context-related concerns. The author would like to express his sincere gratitude to all formerly supervised students for their commitment and support of this research project and of the Ph.D. thesis at hand.

Name	Thesis
Sigmund Brielmaier	Entwicklung und Einsatz von Doppelthermoelementen zur Messung von Flammentemperaturen in Hochdruck-Gasturbinenbrennern, Semesterarbeit, filed in 2012
Marc Rodriguez Girbau	Numeric Thermal Analysis of a Staged Gas Turbine Combustion Process, Bachelor's thesis, filed in 2012
Balbina Hampel	Luftzahlmessung einer selbstzündenden Flamme mittels Spektroskopie, Diplomarbeit, filed in 2012
Timo Speidel	Konstruktion einer Traversiereinrichtung für eine Abgasentnahmesonde, Semesterarbeit, filed in 2012
Richard Gruner	Programmierung von MATLAB-Tools zur Auswertung von Bildern einer selbstzündenden Erdgasflamme, report of an internship, filed in 2012
Thomas Reichart	Voruntersuchungen zur Selbstzündung von Erdgas unter Hochdruck, Semesterarbeit, filed in 2011
Rupert Graf	Auslegung und Konstruktion einer wassergekühlten Abgasentnahme-Sonde, Semesterarbeit, filed in 2010
Konrad Braun	Numerische Optimierung des Zentralinjektors einer generischen SEV-Gasturbinenbrennkammer, Semesterarbeit, filed in 2010. Mesh for the second simulation section (see Fig. 4.3).
Ludwig Briesemeister	Auslegung und Konstruktion der Erweiterung eines Hochdruckversuchsstandes, Semesterarbeit, filed in 2010
Fabian Forster	Überarbeitung der Steuerungssoftware des Hochdruckversuchsstandes mittels LabView, Semesterarbeit, filed in 2010